UNIVERSITY OF CAMBRIDGE

DEPARTMENT OF MATERIALS SCIENCE AND METALLURGY

CORPUS CHRISTI COLLEGE

Extraction of Superelastic Parameter Values from Instrumented Indentation Data

Francisco Fernando Roberto Pereira

This PhD project was entirely funded by

GOVERNO FEDERAL BRASIL PÁTRIA EDUCADORA

CNPq Conselho Nacional de Desenvolvimento Científico e Tecnológico

A dissertation submitted for the Degree of Doctor of Philosophy

February 2019

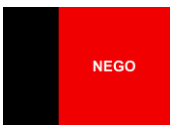

“O otimista é um tolo. O pessimista, um chato. Bom mesmo é ser um realista esperançoso”

Ariano Suassuna

PREFACE

This dissertation is submitted for the Degree of Doctor of Philosophy at the University of Cambridge. The work described within this document was carried out by myself between February 2015 and September 2018, under the supervision of Prof. Bill Clyne, in the Department of Materials Science and Metallurgy at the University of Cambridge.

This dissertation is the result of my own work and includes nothing which is the outcome of work done in collaboration except where explicitly indicated in the text. Neither this, nor any substantially similar dissertation has been, or is currently, being submitted for any degree, or other qualification, at this, or any other university. It contains fewer than 60,000 words.

Francisco Fernando Roberto Pereira

Cambridge

February 2019

ABSTRACT

Extraction of Superelastic Parameter Values from Instrumented Indentation Data

Interest in superelastic (and shape memory) materials continues to rise, and there is a strong incentive to develop techniques for monitoring of their superelastic characteristics. This is conventionally done via uniaxial testing, but there are many advantages to having a capability for obtaining these characteristics (in the form of parameter values in a constitutive law) via indentation testing. Specimens can then be small, require minimal preparation and be obtainable from components in service. Interrogation of small volumes also allows mapping of properties over a surface. On the other hand, the tested volume must be large enough for its response to be representative of behaviour. Precisely the same arguments apply to more "mainstream" mechanical properties, such as yielding and work hardening characteristics. Indeed, there has been considerable progress in that area recently, using FEM simulation to predict indentation outcomes, evaluating the "goodness of fit" for particular sets of parameter values and converging on a best-fit combination. A similar approach can be used to obtain superelastic parameters, but little work has been done hitherto on sensitivities, uniqueness characteristics or optimal methodologies and the procedures are complicated by limitations to the constitutive laws in current use. The current work presents a comprehensive examination of the issues involved, using experimental (uniaxial and indentation) data for a NiTi Shape Memory Alloy. It was found that it is possible to obtain the superelastic parameter values using a single indenter shape (spherical). Information is also presented on sensitivities and the probable reliability of such parameters obtained in this way for an unknown material.

Keywords: NiTi, FEM Simulation, Superelastic Parameter Values, Indentation

Francisco Fernando Roberto Pereira

Cambridge

February 2019

ACKNOWLEDGEMENTS

Firstly, I would like to thank God for this achievement and for once more keeping me safe and healthy (physically and mentally) throughout these years living in Cambridge.

I gratefully acknowledge the financial support from the Brazilian Government, represented by the National Council for Scientific and Technological Development (Conselho Nacional de Pesquisa e Desenvolvimento – CNPq, in Portuguese). From a financial standpoint, there were difficult times in Brazil during my PhD time, but this sponsor made sure that this research (and many others) reached its completion.

My family, of course, gave me tremendous emotional support and love throughout this entire PhD process (2015-2018). My parents (Francisco & Evanilza), my sisters (Fernanda & Renata) and my whole family did everything they could to keep me focused on this hard task. I am truly thankful for everything they have done for me. I would never have made this far without them.

Good friends from Brazil kept me under their radar during these PhD years and I am very thankful for that. My special thanks go to: Josué Buriti, Fernando Araújo, Bruno Moura, Leonardo Pereira, Euller Lima and Jackson Simões. These guys are first-line warriors in any battle. Also, I would like to thank Fernanda Cardozo, for being there for me when I needed.

I truly acknowledge my supervisor, Bill Clyne, nor only for academic support but also for his help and advise, from the application process until the very end of this thesis. His knowledge and experience were crucial for the completion of this PhD work. Furthermore, he gave me many opportunities for career development and personal growth via conference participation and group/individual meetings, among other things, which enormously contributed to enrich this PhD experience.

My special thanks go to Jimmy Campbell, who helped a lot throughout this PhD saga. His knowledge helped and guided me many times, especially when I reached dead ends on this journey.

Many thanks to Rob Thompson whose help was also crucial, especially on developing python scripts. His contributions were very much appreciated here.

I also would like to thank James Dean for his time and engagement with this PhD work. His knowledge on FE solvers (ABAQUS and COMSOL) and modelling rescued me many times.

Some departmental technicians helped me throughout this work. In particular, I would like to thank Bob Stearn and Giovanni Orlando, for putting their energy and experience towards sorting out my experimental problems. These guys really make life a lot easier. My thanks are also extended to: Dave Saul (teaching lab), Paul Nicholl (workshop), Andrew Rayment (mechanical testing), Mary Vickers (XRD) and Marcos Gutierrez (reception).

Finally, last but not least, many thanks to the Gordon lab crew, who made my coffee mornings and days more fun and relaxed, with many “banterous” times together. Along the way, many “comers and goers” were: Catalina Taltavull, Lakshana Mohee, Jimmy Campbell, Max Burley, Sam Troughton, Joe Reed, Noel Glaenzer, Matthew O'Hara, Nashid Sharif, Yi Cui, Tom Chalklen (summer student in 2016), Tom Edwards, Alastair Houston, Julia Purstl, Megan McGregor and Eleanor Brug.

Francisco Fernando Roberto Pereira

Cambridge

February 2019

TABLE OF CONTENTS

NOMENCLATURE

Acronyms	Description
A	Austenite
ASTM	American Society for Testing and Materials
at	Atomic
BCC	Body-Centered Cubic
DSC	Differential Scanning Calorimetry
EDM	Electrical Discharge Machining
EDX	Energy-Dispersive X-Ray spectroscopy
FEM	Finite Element Method
ISE	Indentation size effects
M	Martensite
MEMS	Micro-Electromechanical Systems
NiTi	Nickel-Titanium
NiTiNOL	Nickel-Titanium Naval Ordnance Laboratory
OP	Optical Microscopy
PE	Pseudo-elasticity
R	Rhombohedral
RFDA	Resonant Frequency and Damping Analyser
SE	Superelasticity
SEM	Scanning Electron Microscopy
SIM	Stress-Induced Martensite
SMA	Shape Memory Alloys
SME	Shape Memory Effect
UMAT	User-defined material's subroutine in ABAQUS
XRD	X-Ray Diffraction

Latin symbols	**Units**	**Description**
A	μm²	Projected area
A_c	μm²	Contact area
a	Å	Axial distance (cubic system)
a_c	μm	Projected contact radius
a_c^A, a_c^M	-	Material parameter for cosine flow rule
a_e^A, a_e^M	-	Material parameter for exponential flow rule
A_f	°C	Austenite finish temperature
A_S	°C	Austenite start temperature
B	-	Fitting parameter of indentations curve
b	Å	Axial distance (cubic system)
b^A, b^M	-	Material parameter for polynomial flow rule
c	Å	Axial distance (cubic system)
c	J Kg^{-1} K^{-1}	Specific heat
C_A	MPa K^{-1}	Stress coefficient of transformation into austenite
C_M	MPa K^{-1}	Stress coefficient of transformation into martensite
d	Å	Interplanar spacing
e	-	Constant depending on the geometry of the indenter
E^*	GPa	Linearization of the elastic modulus
E	GPa	Elastic modulus
E_A	GPa	Elastic modulus of austenite
E_{eff}	GPa	Effective modulus
E_i	GPa	Indenter's elastic modulus
E_M	GPa	Elastic modulus of martensite
E_r	GPa	Reduced modulus
E_S	GPa	Elastic modulus of single-variant martensite
E_T	GPa	Tangent modulus
F_b	μN	Bifurcation force
F_r	μN	Return force
h	-	Integer of Miller index
H	GPa	Hardness
k	-	Integer of Miller index

K	MPa	Work-hardening coefficient
l	-	Integer of Miller index
m	-	Fitting parameter of indentations curve
m	-	Number of dimensions of a parameter space
M_f	^{o}C	Martensite finish temperature
M_s	^{o}C	Martensite start temperature
n	-	Work-hardening exponent
N	-	The total number of displacement increments
N_A	-	Number of annealings to be performed during the analysis
P	N	Indentation load
$P_{i,\mathrm{E}}$	μm	Experimental displacement
$P_{i,\mathrm{M}}$	μm	Modelled displacement
P_{max}	μN	Maximum indentation load
R	μm	Radius of spherical indenter
s_0	J K^{-1}	Effective entropy at reference state
S	N μm^{-1}	Contact stiffness
$\boldsymbol{S}$	-	Effective compliance tensor
S	-	Sum of the squares of the residuals
S_{red}	-	Reduced sum of squares
T_o	^{o}C	Equilibrium temperature
T_{room}	^{o}C	Room temperature
u_0	J Kg^{-1}	Effective specific internal energy at the reference state
$\boldsymbol{x}_{cen}$	-	Centroid of the (reduced) simplex
$\boldsymbol{x}_{exp}$	-	A trial point established by expansion
$\boldsymbol{x}_{IC}$	-	A trial point established by inside contraction
$\boldsymbol{x}_{OC}$	-	A trial point established by outside contraction
$\boldsymbol{x}_{ref}$	-	A trial point established by reflection
$\boldsymbol{x}'_j$	-	A trial point established by shrinkage
$\boldsymbol{x}_1 \ldots \boldsymbol{x}_{m+1}$	-	Points expressed as vectors in parameter space

Greek symbols	**Units**	**Description**
α	-	Scale factor
α	°	Axial angles (cubic system)
$\boldsymbol{\alpha}$	-	Effective compliance tensor
α_A	K^{-1}	Coefficient of thermal expansion of austenite
α_M	K^{-1}	Coefficient of thermal expansion of martensite
β	-	Dimensionless correction factor
β	-	Scale factor
β	°	Axial angles (cubic system)
γ	-	Scale factor
γ	°	Axial angles (cubic system)
δ	μm	Indentation depth
δ	-	Scale factor
δ_c	μm	Extrapolated (elastic) indentation depth
δ_f	μm	Final (residual) indentation depth
δ_{max}	μm	Indentation depth at maximum load
ΔH	J g^{-1}	Enthalpy of transformation
ΔT	°C	Thermal hysteresis
ε	-	Total strain
ε_e	-	Elastic strain
ε_L	-	Transformation strain
ε_P	-	plastic (von Mises) strain
θ	-	Weighting factor
K	W m^{-1} K^{-1}	Thermal conductivity
λ	Å	Radiation wavelength
μ	-	Coefficient of friction
μ_1^c, μ_2^c	-	material constants (cosine flow rule)
μ_1^e, μ_2^e	-	material constants (exponential flow rule)
μ_1^p, μ_2^p	-	material constants (polynomial flow rule)
ν	-	Poisson's ratio

ν_A	-	Poisson's ratio (Austenite)
ν_i	-	Poisson's ratio (Indenter)
ν_M	-	Poisson's ratio (Martensite)
ξ_A	-	Volume fraction of austenite
ξ_S	-	Volume fraction of martensite
ρ	Kg m^{-3}	Density
σ	MPa	Transformation inducing stress
σ	MPa	Uniaxial stress
σ_{Af}	MPa	Austenite final stress
σ_{As}	MPa	Austenite start stress
σ_f	MPa	Forward transformation stress
σ_{Mf}	MPa	Martensite final stress
σ_{Ms}	MPa	Martensite start stress
σ_n	MPa	Normal stress
σ_r	MPa	Reverse transformation stress
σ_{VM}	MPa	Von Mises stress
σ_Y	MPa	Yield stress
τ	MPa	Shear stress

1. INTRODUCTION

1.1. Background

Shape memory alloys (SMA) continue to be subjected to intensive study and development. The most common SMA system is nickel-titanium, usually with a composition close to Ni-50 at%Ti [1-4]. Below M_f, defined as the temperature at which (shear) transformation of the parent austenitic phase to the martensitic phase is complete, the latter (monoclinic B19' structure in the NiTi case) is thermodynamically stable. On heating to a higher temperature A_f, reversion to the parent phase (cubic B2 structure in the NiTi case) is complete. Above A_f, SMA can demonstrate superelasticity (SE), in which large mechanically-imposed strains (up to ~8%) can be accommodated by transformation of the parent phase to metastable martensitic variants. These variants revert to the parent phase on the removal of the applied load. The shape memory effect (SME) can also be observed in these alloys. Application of stress at a temperature below M_f can lead to the strain being accommodated by reorientation of martensitic variants. On heating above A_f, however, the martensite can transform to the parent phase in such a way that the original shape is recovered. Subsequent (unloaded) cooling below M_f can occur without further shape change. Repeated cycles of deformation, followed by heating to give shape recovery, are possible and other types of shape memory behaviour can also be observed.

The application of instrumented indentation to SMA has expanded sharply in the past decade. One of the primary objectives is to obtain local SE and SME characteristics. For this purpose, it is important that a representative volume of material should be interrogated, which usually requires the deformed region to contain at least a handful of grains. As it happens, the grain size of SE alloys is often fairly small, so this requirement may not be too demanding and relatively small indents may be viable, facilitating the study of joints and other regions of compositional and microstructural variation in SMA structures. There are, however, various complications associated with the imposition of complex strain fields on SE alloys and interpretation of their indentation response requires care.

The general concept of obtaining bulk mechanical properties from instrumented indentation data is a challenge that has received intensive study over recent years.

Young's modulus can readily be obtained, from the unloading curve, which can typically be taken to represent purely elastic behaviour. However, this property is usually of limited interest, although in the case of SMA the two phases may have significantly different stiffness values, so the phase proportion is relevant to the outcome [5]. In addition to the relatively small number of studies aimed at SE and SME characteristics, various attempts have been made to use indentation data to obtain properties of conventional alloys, including quasi-static stress-strain relationships, creep characteristics, the strain rate dependence of plasticity and even fracture characteristics, such as the fracture energy. Most of these attempts have met with limited success, and many have been based on seriously flawed assumptions or approximations, mainly concerning the treatment of the complex evolving stress and strain fields beneath an indenter.

The most promising and flexible approach for all of these cases is that of iterative FEM simulation of the indentation process. The concept involved is the simple one of repeatedly changing the values of the material property input parameters until an optimal agreement is reached between measured and predicted outcomes. Of course, there are various issues, including choice of the outcomes to monitor, quantification of the "goodness-of-fit" and the need to identify a suitable formulation (constitutive law) describing the behaviour concerned. There are also some more subtle challenges, such as how to associate a level of confidence with the set of inferred values, given that there may be some alternative combinations giving similar levels of agreement with the experimental outcomes − i.e. the issue of the "uniqueness" of the solution.

Despite these difficulties, progress has been made on developing robust FEM-based methodologies for inferring a number of properties from indentation data − particularly quasi-static plasticity parameters [6-11]. Properties exhibiting some sort of time dependence, such as creep and the strain rate sensitivity of plasticity, are rather more complex, particularly in the case of creep, for which behaviour in the primary regime tends to dominate the outcomes of indentation experiments [12, 13]. It may be noted that SE behaviour can sometimes exhibit [14] a dependence on time (i.e. on strain rate), although it is often appropriate to neglect this.

Study of SE behaviour using indentation has thus reached an interesting stage. The number of parameters required to characterise the SE response tends to be

relatively large, which always makes the procedure more challenging. There is also the complication of whether any conventional plasticity is taking place within the system. Unlike uniaxial loading, indentation involves large local variations in stress and strain levels, so that inferring what may or may not be happening in different locations requires much more sophisticated interpretation of the experimental data.

In fact, there have been some studies [15-26] in which the indentation response of materials exhibiting SE have been examined, with many of these [15, 19, 24, 25] involving numerical (FEM) modelling of the indentation process. Of course, there have also been FEM simulations of the deformation of SE alloys in other types of loading situation [27, 28]. Such modelling does require analytical formulation to represent the behaviour, which, as mentioned above, tends to require a relatively large number of parameters in the case of SE. Nevertheless, some commercial FEM packages, such as ABAQUS, do incorporate standard SE formulations and, at least for most studies in this area, researchers are constrained to use these.

However, while a few publications describe work in which SE deformation has been simulated (in relatively complex loading situations) by using such packages, there has been little or no systematic work on iterative FEM simulation of indentation in which this mode of deformation is dominant, aimed at convergence between experimental and modelled outcomes. This is regarded as essential if the ultimate goal of identifying a robust methodology for obtaining SE parameter values solely from experimental indentation data is to be achieved. The present work is oriented in this direction.

1.2. Scope

This work is aimed at developing an iterative methodology to extract superelasticity parameters from instrumented indentation data, using existing material formulations implemented in FE packages. To this end, it is essential to understand the experimental issues involving indentation testing, as well as the computational aspects of modelling it. At the continuum mechanics level, there will be some limitations and challenges when modelling superelastic NiTi, and these might affect the outcome of the proposed methodology. Such limitations are investigated.

The primary goal of this thesis is to investigate whether or not indentation, coupled with FE modelling, can be a viable route to infer properties of NiTi, and perhaps more generally, be expanded to other materials with complex behaviour. In a mid-term perspective, this might be incorporated into FE packages as one of their capabilities.

1.3. Structure of the Thesis

Chapter 2 covers the fundamentals of shape memory alloys, such as martensitic transformations and mechanical behaviour on a continuum mechanic level.

Chapter 3 provides a more targeted introduction to NiTi alloys. Thermomechanical phenomena, mechanical properties, phase diagram and crystallographic aspects are described here. Issues related to FE modelling of superelastic behaviour of NiTi and current material formulations available are also addressed in this chapter.

Chapter 4 presents a number of important considerations that must be accounted for during indentation experiments and modelling. Finally, FE modelling of indentation and inverse methodologies to infer material parameters from indentation data of (NiTi and conventional metals) are reviewed.

Chapter 5 covers the material characterisation. The experimental techniques include metallographic sample preparation, DSC, XRD, optical microscopy and resonant frequency and damping analysis. This chapter also includes the outcomes of such techniques.

Chapter 6 describes how finite element models were built in this research. It gives an overview of how meshes and boundary conditions were set as well as the identification of input parameters for the material formulations.

Chapter 7 covers the basic principles behind the search algorithm developed for parameter extraction from indentation data. Descriptions of the quantification of the goodness-of-fit parameter, Nelder-Mead search method and convergence are also given. The sequence of operation of the algorithm is presented.

Chapter 8 discusses the outcomes of uniaxial compression experiments, involving issues such as compliance, major and minor stress-strain loops and anisotropy. Modelling and limitations of the material formulations are also presented here.

Chapter 9 presents considerations for the design of the indentation rig. Choice of indenter, scale effects and compliance procedure are discussed. The outcomes of indentation experiments, including loading rate dependence, indentation ratio, anisotropy and correlation between different spherical indenters.

Chapter 10 assesses the outcomes of the iterative methodology for the extraction of SE parameter values. The method is validated using a NiTi alloy with known properties. Some discussion is also presented about the limitations of such methodology and its sensitivity to the material formulation.

Chapter 11 is a summary of the conclusions drawn from this thesis, as well as suggestions for future work.

2. FUNDAMENTALS OF SHAPE MEMORY ALLOYS

2.1. Mechanically-induced Shear Transformations

Martensitic transformations [29-32] are diffusionless and involve cooperative shear (to a new crystalline phase) as shown in Figure 2.1(a). The transformation is most commonly driven by mechanical deformation or by a change in temperature. A martensitic transformation is an example of a displacive transition, and it is the origin of both shape memory effect (SME) and superelasticity (SE) [33] (discussed in more detail in §2.3 and §2.4).

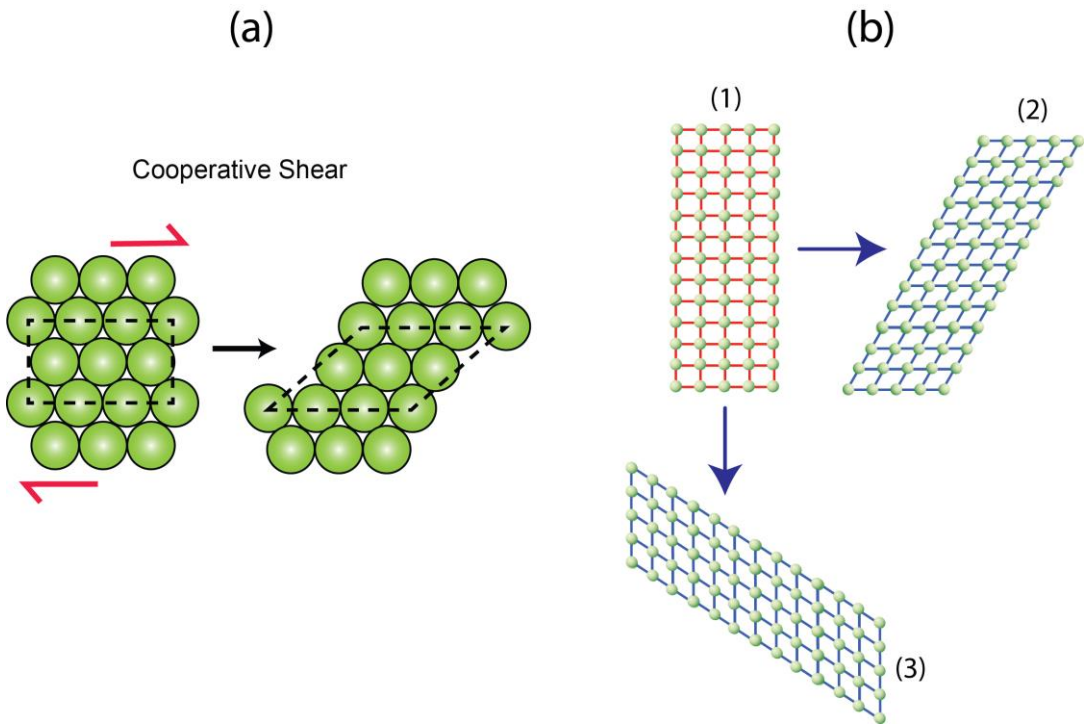

Figure 2.1. Schematic representation of (a) cooperative shear and (b) Two-dimensional representation of a martensitic transformation from a square lattice (1) to two variants (2) and (3) which differ only in orientation, adapted from Otsuka and Wayman [34].

Some crystalline materials can experience different mechanisms of deformation, which occur within a range of temperatures and involve a cooperative motion of a relatively large number of atoms (by cooperative shear) (see Figure 2.1(a)), each being displaced by only a small interatomic distance. This cooperative process is characterised by a homogeneous shear of a large volume of material, which creates a new crystal structure. This process is known as a martensitic phase transformation. In its fully martensitic state, the material is composed of martensite crystals with two

different orientations: opposite shear directions (Figure 2.1(a)). This morphology enables the martensite crystals to cancel out the shear deformation, and as a result, minimises the deformation of the material. This process is known as self-accommodation. The martensite crystals formed from the parent phase, but which have a different orientation, are called variants. In the case of the B19′ phase in NiTi, when the martensite is monoclinic, there can be up to 24 different orientations [30].

In the example in Figure 2.1(b), a quadratic array of circles (1) is representing atoms in a crystal structure. For some reason, this array becomes unstable and distorts into the lattice (2). This distortion is large, but the area of the array remains the same. It is a homogeneous distortion of the original lattice in which an atom does not change its position with respect to its neighbours. Since the original lattice (1) has quadratic symmetry, an equivalent distortion leads to (3), having a different orientation in space. The stability of the lattices will depend on a thermodynamic variable, such as temperature. Due to this atomic correspondence, this mechanism is able to create a driving force, associated with the free energy difference between the two phases, for reversing the phase change, giving the possibility of shape recovery [34, 35].

In theories of martensitic transformations [4], the interface between parent and martensite phases is known as habit plane, seen in Figure 2.2. Such a feature is considered to be an invariant plane, which is undistorted and unrotated since it gives the lowest strain energy.

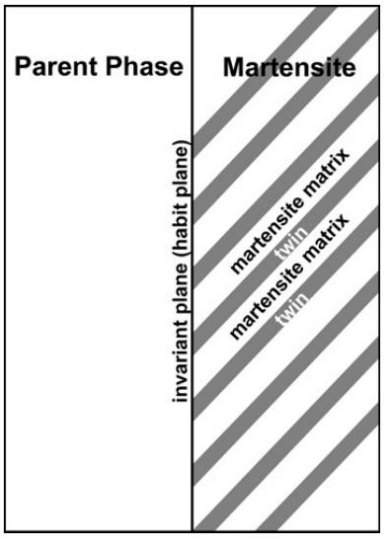

Figure 2.2. Schematic illustration of parent and martensite with the invariant plane as a habit plane [4].

This is the case where the lattice invariant shear is twinning (twinning modes in B19' martensite are addressed in §3.2). The left-hand side represents the parent phase, while the right-hand side a martensite plate. This plate, which consists of a martensite matrix and its twin, is called a habit plane variant. However, the martensite matrix and the twin, which are the smallest scale martensite variants, also each have a specified lattice correspondence with the parent phase. These are called correspondence variants [4].

2.2. Thermal Hysteresis and Terminology

The phase transformation can be investigated via differential scanning calorimetry (DSC) (see §5.2). It can be characterised as shown in Figure 2.3, with respect to the fraction of martensite.

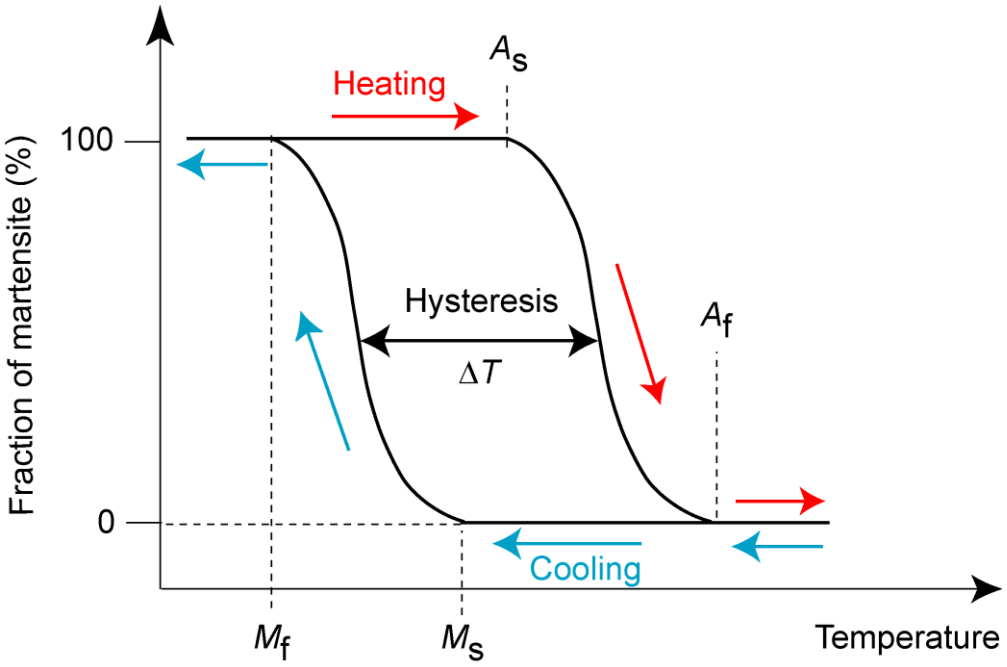

Figure 2.3. A generic representation of a thermal hysteresis, adapted from Otsuka and Wayman [34].

The terminology of each point in the process is also presented. The temperature range of the transformation is relatively small, although the beginning and end of the transformation during heating or cooling extends over a much broader temperature range. The transformation from austenite into martensite shows a thermal hysteresis (ΔT). This transition is characterised by values of temperature. On cooling from a temperature at which the austenite is stable, the alloy transforms into martensite via an exothermic reaction. On heating, there is the reverse transformation into austenite

with an endothermic reaction. As shown, it is possible to establish four transformation temperatures – namely the martensite start temperature (M_s), the martensite finish temperature (M_f), the austenite start temperature (A_s) and the austenite finish temperature (A_f).

2.3. Shape Memory Effect

The shape memory effect (SME) involves martensitic transformations stimulated by changes in temperature. It is schematically explained in Figure 2.4, representing a shape memory spring.

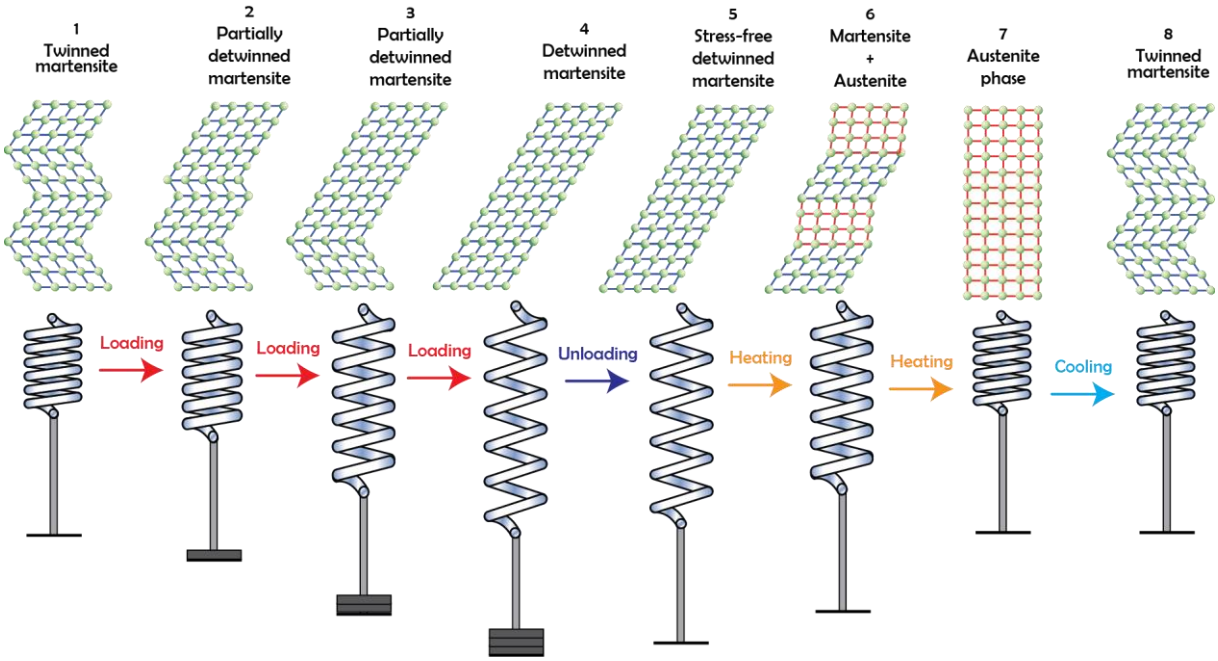

Figure 2.4. Schematic representation of the SME in a spring.

This effect occurs at low temperatures, at which the material microstructure is initially composed of twinned martensite (stage 1). By increasing the load gradually, a detwinning process takes place (stages 2-3) until the stress reaches the critical value for detwinned martensite (stage 4). At this point, due to martensite reorientation, there is a macroscopic deformation. Upon unloading, the macroscopic deformation is retained as variants of martensite (stage 5). When the material is heated above A_f, the martensite reverts into austenite, allowing the spring to recover its macroscopic shape (stages 5-7). On cooling, austenite is converted into martensite (stress-free transition), but there is no macroscopic change during this process (stages 7-8).

From a stress-strain standpoint, represented in Figure 2.5, the specimen starts from the reference point 1 at a given temperature and zero stress.

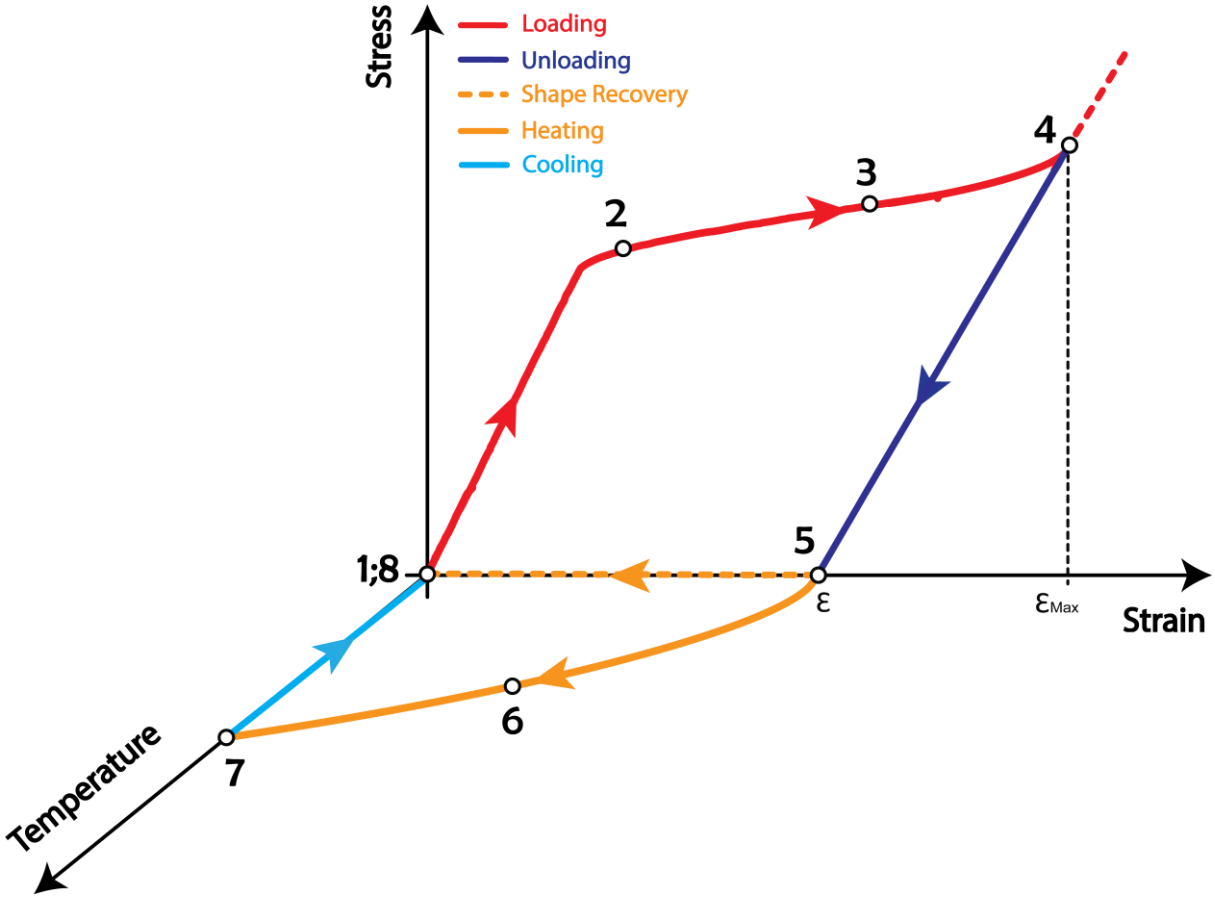

Figure 2.5. Schematic stress-strain-temperature diagram of a typical NiTi material undergoing SME, adapted from Otsuka and Wayman [34].

The stress is then gradually increased, and the material's behaviour is linear elastic (slope). Apparent non-recoverable deformation starts to develop at nearly constant stress (plateau 2-4). Unlike plastic deformation, however, the SMA deformation reaches saturation, and a further increase of the load leads to a new linear elastic behaviour (beyond stage 4 – dashed line). Upon unloading, a residual deformation is present (stage 5), which can be recovered, as described, by heating the material (above A_f) (stages 5-7) until it reached stage 7, where there is no remaining strain. Finally, when the spring is cooled down to its initial temperature (below M_f), the initial material state (stage 1) is completely recovered (twinned martensite). There is, however, a limit for that shape memory recovery, which will depend on the alloy. A typical range is 4-8% [4, 30, 34, 36, 37].

2.4. Superelasticity

The phenomenon known as superelasticity (SE) [1, 34-36, 38], or pseudo-elasticity (PE), takes place when the SMA is loaded above its critical temperature A_f. This is an isothermal phenomenon and involves the storage of potential energy. Superelastic deformations arise when imposed strains are accommodated by the formation of martensite variants, which reverse upon removal of the load. It is, thereby, a behaviour associated with a stress-induced transformation. This is demonstrated, schematically, in Figure 2.6, by using a representation of a superelastic spring.

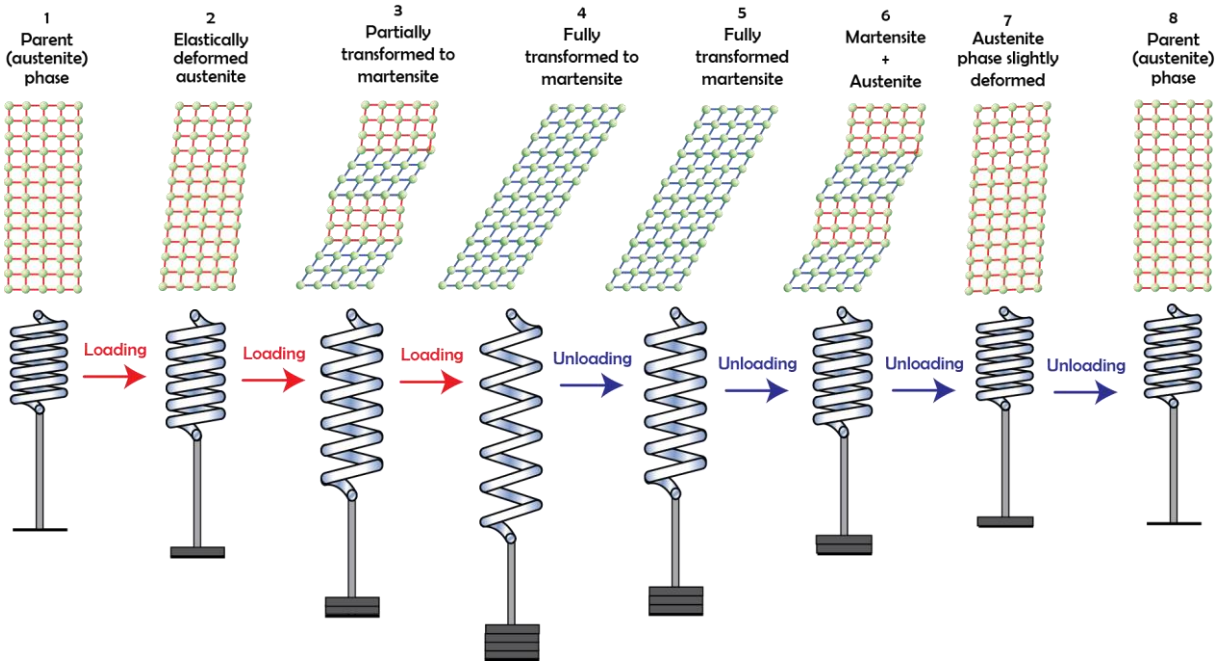

Figure 2.6. Schematic representation of the mechanism of SE in a spring.

During loading of the spring from stage 1 to stage 2, there is only elastically deformed austenite. The stress-induced phase transition takes place from stage 2 up to stage 4, where austenite is converted into martensite (stage 4). On unloading, the martensite becomes unstable (stage 6) and reverts to its parent phase (austenite), resulting in full strain-recovery (stage 1=8) after unloading. This is explained in terms of the stress-strain curve shown in Figure 2.7.

The material of the spring is initially austenitic (stage 1). During loading, the critical stress for the phase transition, known as martensite start stress (σ_{Ms}), is reached (stage 2) and the material starts transforming into detwinned martensite (plateau 2-4). The phase transition is complete when the stress level reaches the martensite finish

stress (σ_{Mf}) value. Further loading will only cause elastic deformation of the detwinned martensite up to a critical point. Austenite is the only stable phase at high temperature and no stress. Thereby, upon unloading the critical stress for the reverse phase transition, known as austenite start stress (σ_{As}), is reached and the spring begins to recover its original phase (plateau 5-7). The reversion is complete when the austenite finish stress (σ_{Af}) is reached. The macroscopic deformation is fully recovered at this point.

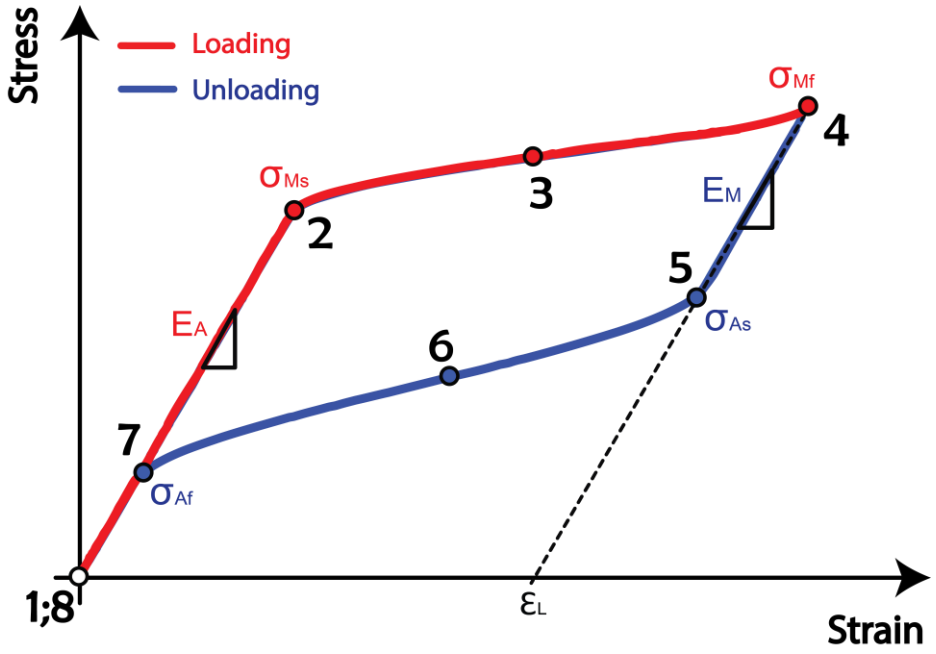

Figure 2.7. Schematic stress-strain plot of a typical NiTi alloy undergoing SE, Otsuka and Wayman [34].

The main characteristic of stress-strain plots of SE alloys is the pronounced hysteresis since the loading and unloading paths do not occur at the same stress levels. This is analogous to the hysteresis observed during thermal cycling (see Figure 2.3) and occurs for the same reasons (i.e. the stored elastic strain energy contribution causes an extra driving force to be required). This hysteresis is related to the mobility of the austenite/martensite interface.

The stress required to induce the transformation increases linearly with temperature, according to the Clausius-Clapeyron equation:

$$\frac{d\sigma}{dT} = -\frac{\Delta H}{\varepsilon T_0} = C \tag{2.1}$$

where σ is the transformation-inducing stress, T_0 is the equilibrium temperature, and ΔH is the enthalpy of transformation. In particular, C is the slope of the boundary surfaces, also known as stress influence coefficients, which identify the transformation into martensite and austenite, C_M and C_A, respectively. The straight blue line with a negative slope (see Figure 2.8) represents the critical stress to induce slip. Since slip never recovers upon heating or unloading, the stress must be below the blue line to enable SE to occur [4, 34, 35]. It is clear that the temperature at which superelasticity occurs is limited to a specific range. If the temperature is below A_f, the stress-induced martensite (SIM) does not revert to austenite. Thus, there remains some residual strain which vanishes on heating above A_f, due to SME. If the deformation temperature is too high, then the transformation stress exceeds the yield stress of the material (blue line), and the alloy deforms plastically.

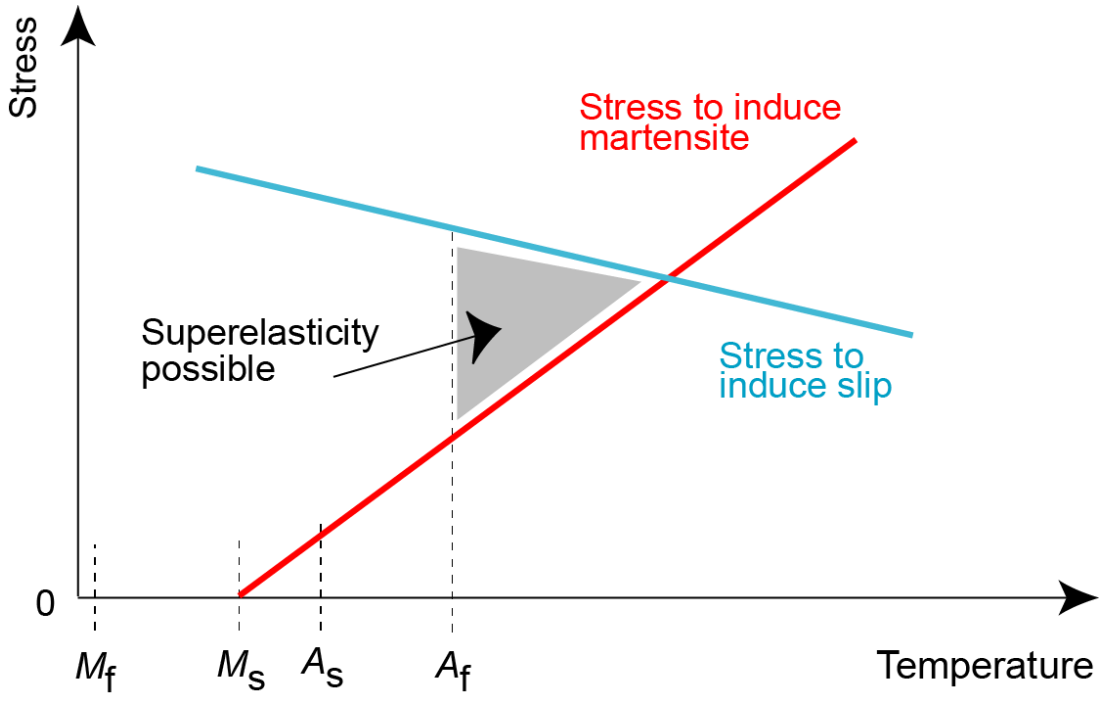

Figure 2.8. Schematic diagram representing the region of superelasticity in stress-temperature coordinates, adapted from Otsuka and Wayman [34].

2.5. Summary

The following conclusions can be drawn from this chapter:

- The martensitic transformation is the mechanism responsible for both the shape memory effect (SME) and superelasticity (SE). Self-accommodation and lattice invariant shear are important features in theories of martensitic transformations towards understanding these two thermomechanical phenomena.
- Thermal hysteresis (as well as stress hysteresis) is an important characteristic in SMA due to different paths taken by the material during cooling and heating. Transition temperatures can be experimentally measured in order to characterise this transformation.
- There are differences between SME and SE in terms of both stress-strain curves and triggering their activation. These stress-strain curves are characterised by stress plateaus, stress transitions, transformation strain and moduli of phases.
- There is an optimal region in the stress-temperature diagram within which SE can occur.
- The Clausius-Clapeyron equation dictates that the stress required to induce the phase transformation increases linearly with temperature.

3. NiTi ALLOYS

Most commercial applications involving SMA are related to superelastic NiTi, commercially called NiTiNOL, due to its shape memory properties, biocompatibility and fatigue life. These alloys are very attractive for applications such as medical instruments [39, 40], engineering devices [2, 41], sensors and MEMS [42].

3.1. Crystallographic Aspects

In the austenite (parent) phase, NiTi exhibit the CsCl crystal structure, B2 in the Strukturbericht notation [43]. The transition from the parent phase to monoclinic (B19') can follow the paths presented in Figure 3.1.

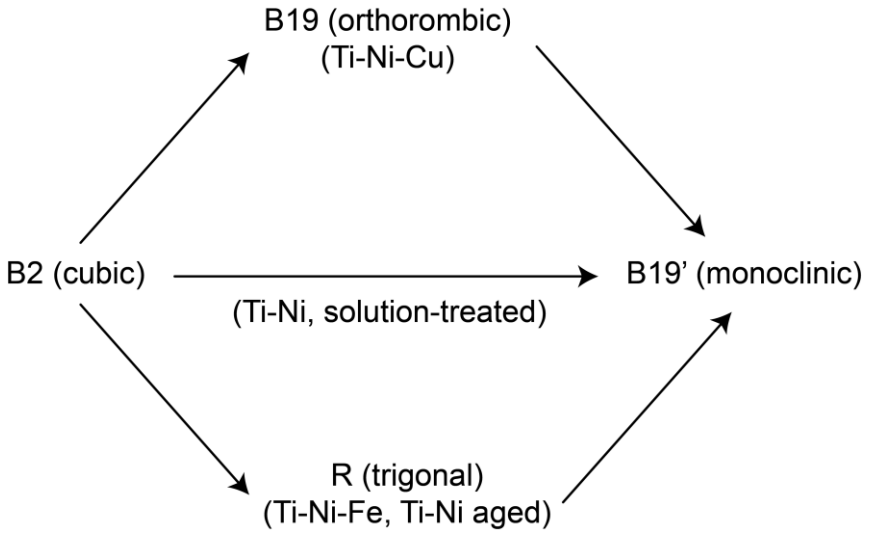

Figure 3.1. Three transformation paths to B19' (monoclinic) in Ti-Ni alloys, adapted from Otsuka and Ren, [4].

There is a tendency to transform from B2 to B19' martensite in Ti-Ni-based alloys, and in fact, for the solution-treated binary Ti-Ni alloys the transformation occurs from B2 to B19' directly, while for the upper and lower cases two successive transformations occur upon continuous cooling. However, depending on the composition and heat-treatment only the first transformation may occur whereas the second one might be lost since the possible transformation temperatures for the second one to B19' becomes too low (i.e. below 0 K) in that case [4]. The lattice change is shown in Figure 3.2.

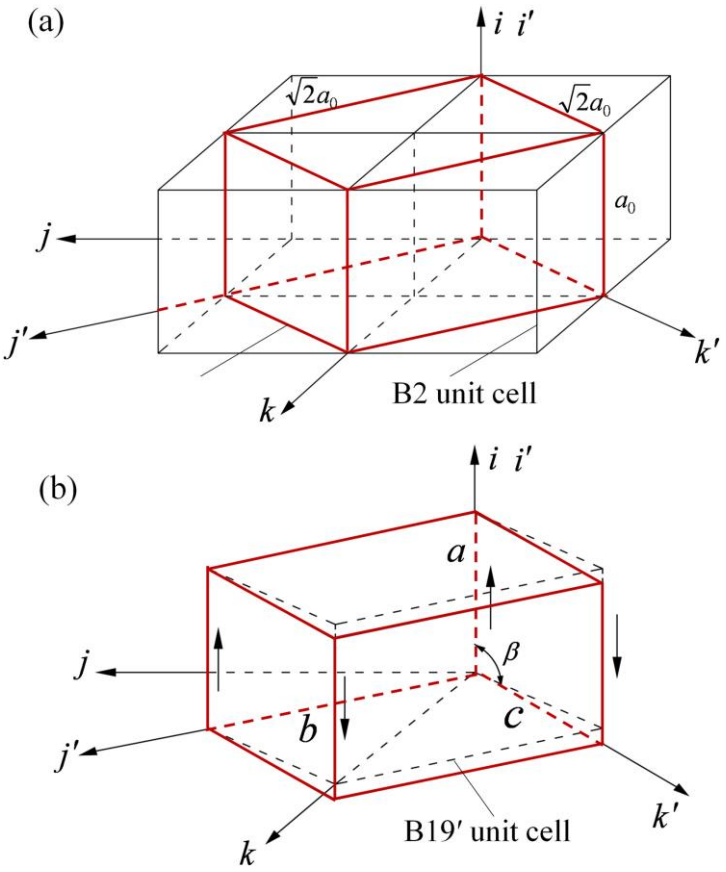

Figure 3.2. Schematic diagram of the transformation from (a) B2 austenitic phase into (b) B19' martensitic phase [44].

Figure 3.2 shows how a tetragonal unit cell in the B2 parent phase (a) (black lines) is transformed into a monoclinic unit cell in the B19' product phase (b) by means of a combination of a uniform expansion or contraction with a simple shear. The lattice parameters are a_o = 0.3015 nm in the cubic unit cell, and a = 0.2889 nm, b = 0.4120 nm, c = 0.4622 nm, and β = 96.8° in the monoclinic unit cell [4, 44]. Due to the different crystallographic structures, the two phases have different properties, such as electrical resistance and stress-strain parameters [2, 45-47].

The B19' martensite can be obtained either by a single step transformation of B2 → B19', or by a two-step transformation of B2 → R-phase → B19', as shown in Figure 3.3. In the two-step transformation, the R-phase is a rhombohedral phase that is incommensurate with the cubic B2 phase. The unit cell of the rhombohedral phase is created from the B2 cell by elongating the latter along any of the <1 1 1> directions [4, 36, 48].

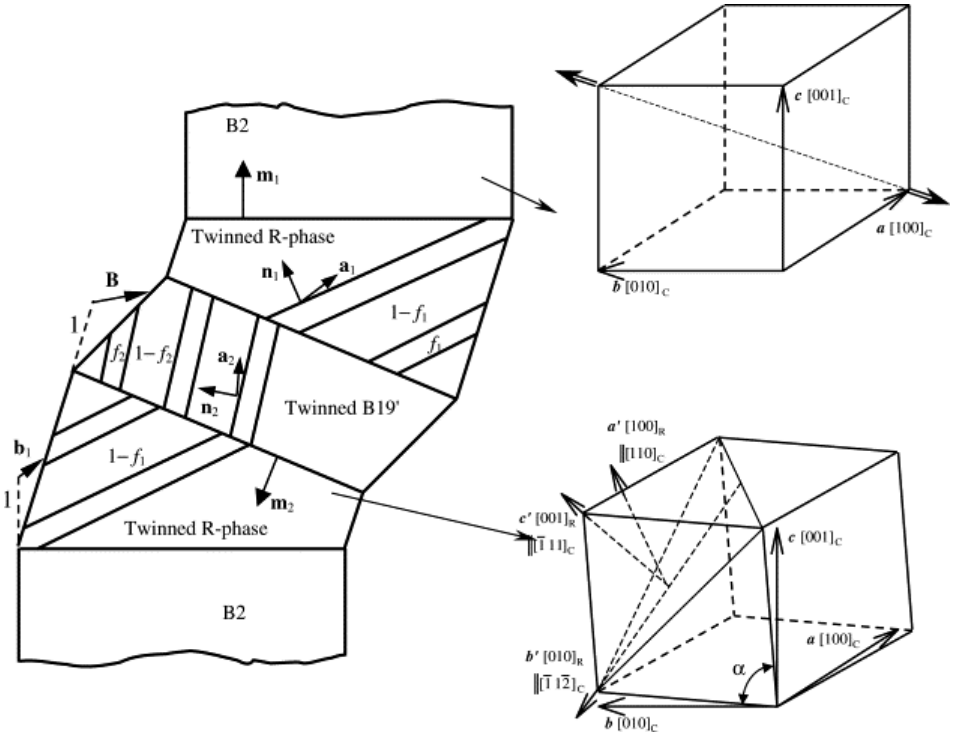

Figure 3.3. Schematic diagram showing the transformation planes and directions associated with successive step transformation of B2 → R-phase and R-phase → B19' and the unit cells of the B2 phase and the rhombohedral phase [48].

The two-step transformations of B2 → R-phase and subsequent R-phase → B19' may occur upon cooling when R_S (R-phase start temperature, as in the other temperatures) is above M_S. The occurrence of this particular phase will strongly depend on the chemical composition, thermomechanical history and heat treatment [48-50].

3.2. Twins in Martensite B19'

When NiTi shape memory alloy is transformed from B2 austenitic phase into B19' martensitic phase, the resultant two twinned martensite variants must meet the requirements for compatibility, which is defined as the twinning equation governing the interface between two twinned martensite variants. The lattice invariant shear (i.e. twinning modes) is an important input parameter for the phenomenological theoretical calculations. Details in mathematical theories to determine twinning modes were extensively discussed by Knowles and Smith [51], Otsuka and Ren [4] and Hu et al. [44].

A twin can be represented by a deformation of a unit sphere into an ellipsoid by shear with the twinning elements (K_1, η_1, K_2 and η_2), shown in Figure 3.4.

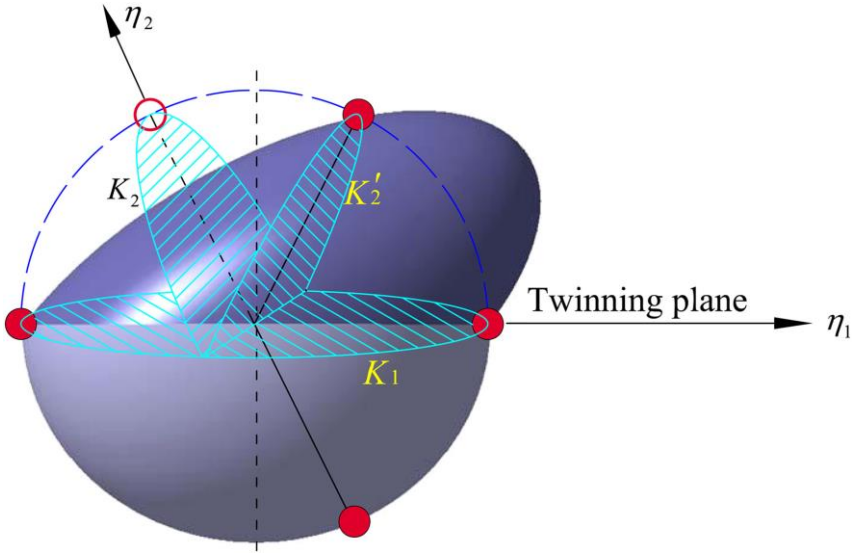

Figure 3.4. Schematic diagram of the twinning elements of NiTi shape memory alloys [44].

As described by Hu et al. [44], the element K_1 is the twinning plane which is not subjected to distortion and rotation. The element η_1 represents the direction of the twinning shear. The element K_2 is the second undistorted plane and the element η_2 is defined as the intersection of the K_2 plane and the shear plane. The twin is defined as a type I twin if the K_1 plane and the η_2 direction are rational indices, and the K_2 plane and the η_1 direction are irrational indices. The twin is defined as a type II twin if the K_2 plane and the η_1 direction are rational indices, but the K_1 plane and the η_2 direction are irrational indices. The twin is defined as a compound twin if the K_1 plane, η_1 direction, K_2 plane and η_2 direction are all rational indices.

Since the B19' structure is low symmetry monoclinic, many twinning modes have been found and reported in the literature [4, 51]. However, there is a consensus among researchers that the type II twinning mode, in which K_1 is irrational, but where η_1 = [011], is the most prevalent one. This was first reported by Knowles and Smith [51].

In the context of the present work, the material will be treated as a continuous and isotropic medium for modelling purposes, which means that crystallographic aspects will not be considered. The material formulations used here do not take into account different types of martensite variants. For a polycrystalline material, the formation of such variants occurs at a very fine scale in all directions, meaning that the assumption of continuous medium upon phase transition is reasonable.

3.3. Phase Diagram

NiTi compounds are located within a narrow band around the equiatomic composition (50NiTi %at) [38]. This particular region of the phase diagram is shown in Figure 3.5.

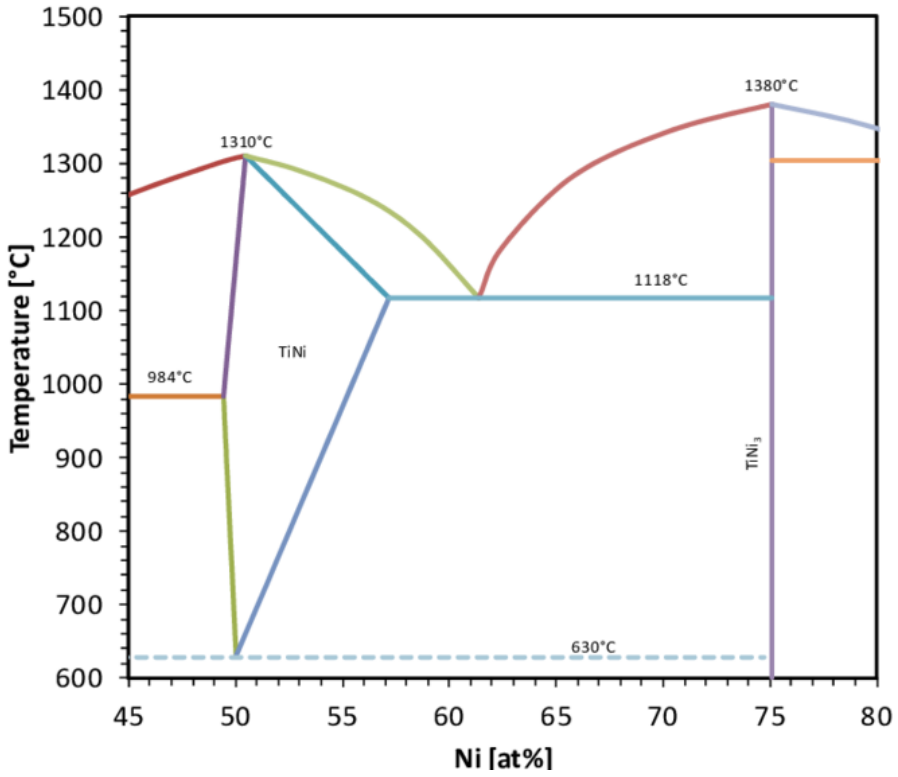

Figure 3.5. “Equiatomic region” of the phase diagram of NiTi binary alloy [52].

It is also noteworthy that the presence of precipitates is more likely in Ni-rich alloys. The boundary on the Ti-rich side is close to 50 at% Ni, and is very steep, whereas on the Ni-rich side the solubility strongly decreases as the temperature lowers [4]. During phase changes in Ni-rich NiTi alloys, one can observe the presence of the R-phase. This is common in near-equiatomic compositions when the alloy is thermally or thermo-mechanically cycled.

According to Lagoudas [53], the formation of Ti_3Ni_4 favours the presence of the R-phase, due to the internal stress field caused by such precipitates, when the Ni content is greater than 50.5 at%. Otsuka and Wayman [34] demonstrated that any addition of Ni up to 50 at% has little effect on the transition temperatures. Furthermore, slight additions of Ni above this percentage tend to, for example, drastically

decrease M_s [37]. This also causes important changes in the mechanical properties of the material.

3.4. Stress-Strain Characteristics

The mechanical behaviour of NiTi alloys is strongly dependent on both chemical composition and temperature [54, 55]. Properties can be tailored by imposing various loading paths, while phenomena associated with the phase transformation are monitored, such as the shape memory effect and the superelasticity, as previously shown (Figure 2.5 and Figure 2.7). These tests are usually carried out on a conventional screw-driven/hydraulic testing machine equipped with a heating stage.

Experimental (a) stress-temperature and (b) stress-strain-temperature diagrams for a NiTi alloy are shown in Figure 3.6. Diagram (a) was constructed based on the stress-strain curves with complete stress-induced martensitic transformation at different temperatures (b). In particular, transformation stresses have a linear relationship with temperature (a), as demonstrated by the Clausius-Clapeyron relationship (§2.4).

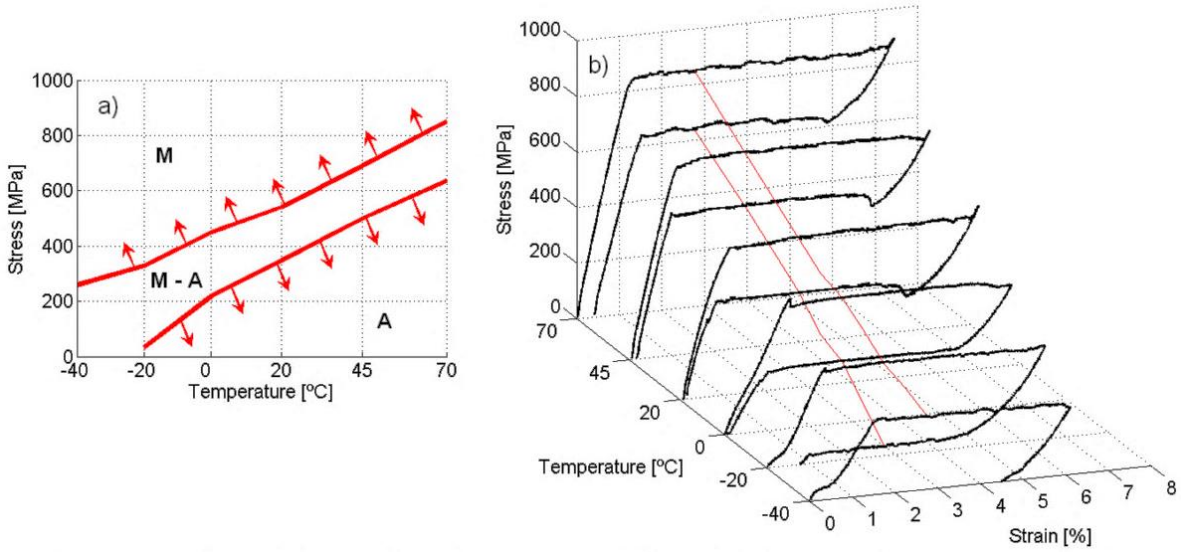

Figure 3.6. Thermomechanical behaviour of NiTi: (a) Stress-temperature plot obtained from (b) stress-strain tests at different temperatures [56].

Each temperature determines a particular stress level that initiates both forward and reverse transformations, upon loading and unloading. In Figure 3.6(b), it is worth noting that the material was, initially, fully martensitic at -40˚C, causing a high level of non-recovered macroscopic deformation upon unloading. As the test temperature

rose, the level of strain recovery is gradually increased, as the material was transforming into austenite.

Properties of NiTi have been the object of study over the last few decades. Some relevant properties for this research are summarised in Table 3.1.

Property	Unit	Value	
		Martensite	Austenite
Density	Kg/m^3	6450-6500	
Temperature hysteresis	˚C	20-30	
Corrosion performance	---	Excellent	
Transition temperatures	˚C	-100 to 120	
Young's modulus	GPa	24-41	65-85
Poisson's ratio	---	0.33	
Stress influence coefficients	$MPa\ K^{-1}$	5-10	

Table 3.1. Relevant property values of NiTi alloys [5, 34, 45, 57].

There are many issues addressed in the successful applications of NiTi, but the main one is undoubtedly related to determining its mechanical properties. Macroscopic mechanical testing can be applied to determine its stress-strain curves, but machining superelastic NiTi alloys to obtain samples can be difficult, and the cutting process itself might affect the properties [58]. In this regard, there is scope for developing accurate characterisation methods to determine mechanical properties, capable of quickly and reliably evaluating the functional properties of NiTi. The methodology proposed in this work, based on FE-inverse analysis, can be applied to small volumes of NiTi alloys in order to infer their mechanical properties.

3.5. Modelling of Superelastic Behaviour of NiTi

Mechanical properties of NiTi/SMA are typically represented by the characteristic stress-strain curve, which has been presented previously as in hysteresis loops during loading/unloading and shape-recovery process. Those properties are desirable and, therefore, there is an interest in using shape-memory materials in industrial applications. In this regard, some constitutive models can reproduce, with some limitations, the macroscopic behaviour of NiTi alloys undergoing stress change [27, 41, 53, 59-65].

Most of these widespread formulations used to model the mechanical behaviour of superelastic NiTi need multiple material parameters [41, 62, 65]. Since the purpose of this present research is to develop a methodology for extracting superelastic parameters of NiTi from indentation data, having many parameters would make the iterative process very time-consuming due to the large number of parameter combinations.

In principle, this current methodology will be developed with one specific material formulation, but the wider goal is to use it with different formulations or even to develop a different one capable of capturing the mechanical behaviour of NiTi with fewer material parameters. This work, the first of its type regarding inferring the properties of NiTi from indentation, may serve to pave the way towards the development of user-friendly software packages, containing built-in resources for FEM implementation, which would require the user only to specify the material formulation and to input a single experimental indentation plot.

3.5.1. Description of a Single-Variant-Martensite Constitutive Model

This approach assumes that there is no distinction between the different single-variant species and that the material is a continuous and isotropic medium. For simplification purposes, this analysis addresses only a one-dimensional model able to reproduce the superelastic behaviour [59]. 1D models, characterised by a simpler formulation than the 3D ones (implemented in ABAQUS), can account for some significant features of the thermomechanical response of SMA, such as the unloading behaviour, different behaviour in tension and compression, and different elastic properties of the phases, introducing fewer material parameters, with clear physical meanings.

According to this model, there are two processes that produce variations of the martensite fraction:

I. The conversion of austenite into single-variant martensite ($A \rightarrow S$).

II. The conversion of single-variant martensite into austenite ($S \rightarrow A$).

For internal variables, ξ_S is termed as the martensite volume fraction and ξ_A is termed as the austenite volume fraction. Even though these variables present restrictions related to phase coexistence, it is possible to use only one independent variable:

$$\xi_S + \xi_A = 1 \tag{3.1}$$

Limiting the discussion to a small deformation regime, one assumes an additive decomposition of the total strain, ε:

$$\varepsilon = \varepsilon_e + \varepsilon_L \xi_S \,\mathrm{sgn}(\varepsilon) \tag{3.2}$$

where ε_e is the elastic strain, ε_L is the maximum residual strain (also known as transformation strain), and sgn (.) is the sign function. The presence of sgn (ε) in the equation indicates that the direction of the effect related to the martensite fraction is governed by the stress. From the point of view of the integration scheme, the time-discrete problem is considered strain-driven. Accordingly, ε and sgn (ε) are assumed to be always known.

The elastic strain is assumed to be linearly related to the stress:

$$\sigma = E\varepsilon_e \tag{3.3}$$

where E is the elastic modulus.

Experimental tests show substantial differences between the austenite and the martensite elastic properties [34, 45]. In order to model this, the elastic modulus is assumed to be a function of the martensite fraction, $E(\xi_S)$, requiring that:

$$E(\xi_S = 0) = E_A, \; E(\xi_S = 1) = E_S \tag{3.4}$$

Valid expressions for $E = E(\xi_S)$ can be obtained regarding the shape-memory alloy as a composite material with a volume fraction of martensite and a volume fraction of austenite. Then, from the homogenisation theory adopting the Reuss scheme:

$$E(\xi_S) = \frac{E_A}{1+(E_A/E_S - 1)\xi_S} \tag{3.5}$$

For the case of a phase-transition evolution equation of the type considered here, a trial state is introduced, defined as the state obtained from the previous solution state, taking into account the new strain and assuming no evolution for the phase transition, as shown in Figure 3.7.

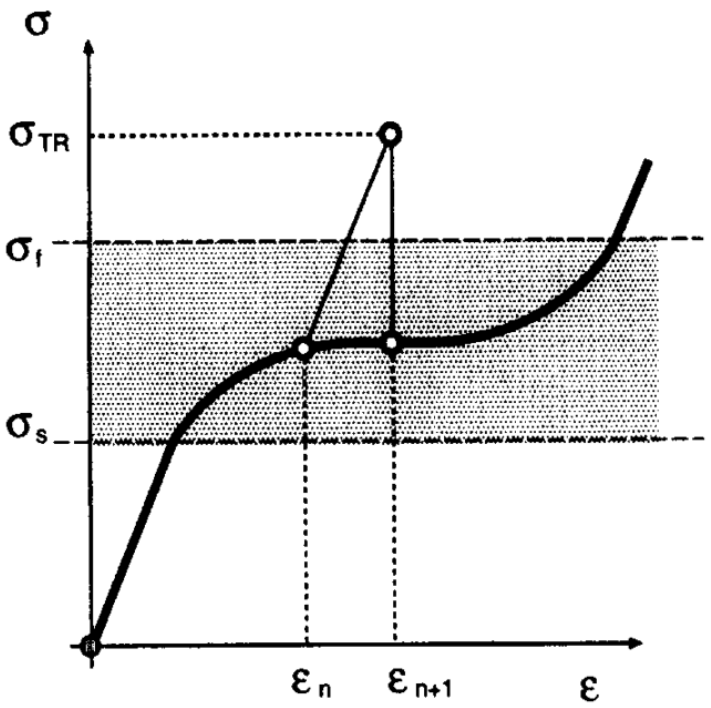

Figure 3.7. Return-map algorithm. The case of a phase transition model with a starting (σ_s) and final value (σ_f) for the occurrence of the phase transformation [59].

However, the elastic domain is not connected (as shown) and, therefore, two trial states have to be introduced: the first one is associated with no phase-transition evolution, and the second one with a complete transition evolution. If the first trial state violates the initial condition for the occurrence of the phase transition and the second trial state does not violate the final condition for the occurrence of the phase transition, then the enforcement of the phase-transition evolution equation guarantees the computation of the correct solution. The overall strain-driven solution algorithm is presented in Table 3.2.

1. Detect loading or unloading

If $(\varepsilon - \varepsilon_n) > 0 \Rightarrow$ Loading

If $(\varepsilon - \varepsilon_n) < 0 \Rightarrow$ Unloading

2. Check phase transformations

If loading then

check $A \rightarrow S$ phase transformation (Table 2.3)

else if unloading then

check $S \rightarrow A$ phase transformation (Table 2.4)

end if

3. Algorithmic tangent.

If phase transformations active, compute algorithmic tangent

Table 3.2. Overall strain-driven solution algorithm, adapted from Auricchio and Sacco [59].

Table 3.3 and Table 3.4 address the proposed solution scheme for the two-phase transformations considered within this formulation.

1. Compute 2 trial states.

First trial state: assume no phase transformation

$$\xi_S^{TR,1} = \xi_{S,n}$$

$$E^{TR,1} = \frac{E_A}{1+\left(E_A/E_S - 1\right)\xi_{S,n}}$$

$$\sigma^{TR,1} = E^{TR,1}\left[\varepsilon - \varepsilon_L \xi_{S,n}\,\mathrm{sgn}(\varepsilon)\right]$$

Second trial state: assume full phase transformation

$$\xi_S^{TR,2} = 1$$

$$E^{TR,2} = E_S$$

$$\sigma^{TR,2} = E^{TR,2}\left[\varepsilon - \varepsilon_L\,\mathrm{sgn}(\varepsilon)\right]$$

2. Check trial states

If $\left|\sigma^{TR,1}\right| < \sigma_{Ms}$ then

$\xi_S = \xi_{S,n}$

Solution found

else if $\left|\sigma^{TR,2}\right| > \sigma_{Mf}$ and $\varepsilon\sigma^{TR,2} > 0$ then

$\xi_S = 1$

Solution found

else

solve discrete $A \to S$ evolutionary equation $(H^{A\to S})$

to find admissible solution

end if

Table 3.3. Solution scheme for the forward phase transformation (A→S), adapted from Auricchio and Sacco [59].

1. Compute 2 trial states.

First trial state: assume no phase transformation

$$\xi_S^{TR,1} = \xi_{S,n}$$

$$E^{TR,1} = \frac{E_A}{1+\left(E_A/E_S - 1\right)\xi_{S,n}}$$

$$\sigma^{TR,1} = E^{TR,1}\left[\varepsilon - \varepsilon_L \xi_{S,n}\,\mathrm{sgn}(\varepsilon)\right]$$

Second trial state: assume full phase transformation

$$\xi_S^{TR,2} = 0$$

$$E^{TR,2} = E_A$$

$$\sigma^{TR,2} = E^{TR,2}\varepsilon$$

2. Check trial states.

If $\left|\sigma^{TR,1}\right| > \sigma_{As}$ then

$\xi_S = \xi_{S,n}$

Solution found

else if $\left|\sigma^{TR,2}\right| < \sigma_{Af}$ and $\varepsilon\sigma^{TR,2} > 0$ then

$\xi_S = 0$

Solution found

else

solve discrete $S \to A$ evolutionary equation $(H^{S\to A})$

to find admissible solution

end if

Table 3.4. Solution scheme for the reverse phase transformation (S→A), adapted from Auricchio and Sacco [59].

The use of a consistent tangent modulus (E^T) preserves the quadratic convergence of the Newton method (for example, in finite element codes). From the linearisation of the elastic relation, E^T is presented as follows:

$$E^T = E + H\left\{E^*\left[\varepsilon - \varepsilon_L \xi_S \operatorname{sgn}(\varepsilon)\right] - E\varepsilon_L \operatorname{sgn}(\varepsilon)\right\} \tag{3.6}$$

The quantity E^* is computed from the linearisation of the elastic modulus, and it is given by:

$$E^* = E_A\left(\frac{E_A}{E_S} - 1\right)\left[1 + \left(\frac{E_A}{E_S} - 1\right)\xi_S\right]^{-2} \tag{3.7}$$

The quantity H is computed from the linearisation of the discrete evolutionary equation corresponding to the active phase transformation. For the conversion of austenite into martensite, the linearisation of the time-discrete evolutionary equation leads to:

$$H = H^{A\to S} = -\frac{(1-\xi_{S,n})E}{(1-\xi_{S,n})\left\{E^*\left[\varepsilon - \varepsilon_L \xi_S \operatorname{sgn}(\varepsilon)\right] - E\varepsilon_L \operatorname{sgn}(\varepsilon)\right\} + \left|\sigma_n\right| - \sigma_{Mf}} \tag{3.8}$$

Similarly, for the conversion of martensite into austenite:

$$H = H^{S\to A} = -\frac{\xi_{S,n}E}{-\xi_{S,n}\left\{E^*\left[\varepsilon - \varepsilon_L \xi_S \operatorname{sgn}(\varepsilon)\right] - E\varepsilon_L \operatorname{sgn}(\varepsilon)\right\} + \left|\sigma_n\right| - \sigma_{Mf}} \tag{3.9}$$

As mentioned earlier in §3.2, this formulation does not account for different types of martensite variants. However, polycrystalline materials can be modelled as continuous media since such variants are formed in all directions (at a very fine scale), meaning that this approach can be used. This formulation is implemented in ABAQUS and has been widely applied to superelastic NiTi applications over the last decade [66]. It is a user-friendly subroutine (UMAT) and depends on material parameters obtained directly from tensile/compression tests, and combines conventional elastic and plastic behaviour with pseudo-elastic properties of shape memory alloy NiTi [27, 59, 63].

There is some literature on using this UMAT to model complex geometries accurately (e.g. NiTi stents), revealing stress/strain fields and the amount of martensitic transformation, among other output variables [67-70]. Thus, this formulation is used as a basis for this research.

3.5.2. Brief Description of an Energy-Based Constitutive Model

This present work also used the energy-based subroutine known as Shape Memory Alloy Unified Model (SMA_UM). This formulation is a FORTRAN coded numerical implementation of an SMA thermomechanical constitutive model. The current version of the SMA_UM implements the unified constitutive model, presented by Lagoudas et al. [71] in more detail, which unifies and generalises the constitutive formulation to three dimensions.

In this approach, the total Gibbs free energy is presented as:

$$G(\boldsymbol{\sigma},T,\xi,\varepsilon^t) = -\frac{1}{2}\frac{1}{\rho}\boldsymbol{\sigma}:\boldsymbol{S}:\boldsymbol{\sigma} - \frac{1}{\rho}\boldsymbol{\sigma}:\left[\boldsymbol{\alpha}(T-T_0)+\varepsilon^t\right] + \\ +c\left[(T-T_0)-T\ln\left(\frac{T}{T_0}\right)\right] - s_0 T + u_0 + f(\xi) \tag{3.10}$$

where $\boldsymbol{\sigma}$, ε^t, ξ, T, and T_0 are the Cauchy stress tensor, transformation strain tensor, martensite volume fraction, current and reference temperatures, respectively. The material constants $\boldsymbol{S}$, $\boldsymbol{\alpha}$, ρ, c, s_0 and u_0 are the effective compliance tensor, effective thermal expansion tensor, density, effective specific heat, effective entropy at reference state and effective specific internal energy at the reference state. Those material constants are defined by the rule of mixtures as:

$$\boldsymbol{S} = \boldsymbol{S}^A + \xi(\boldsymbol{S}^M - \boldsymbol{S}^A),\ \boldsymbol{\alpha} = \boldsymbol{\alpha}^A + \xi(\boldsymbol{\alpha}^M - \boldsymbol{\alpha}^A), \\ c = c^A + \xi(c^M - c^A),\ s_0 = s_0^A + \xi(s_0^M - s_0^A),\ u_0 = u_0^A + \xi(u_0^M - u_0^A) \tag{3.11}$$

where the quantities with the superscripts A and M indicate the values in the austenitic and the martensitic phases, respectively.

The function $f(\xi)$ is defined as transformation “hardening” function (as known as flow rule), and it has different forms of the function that can be selected to recover different constitutive models. In this context, Tanaka [72] developed an exponential model. The function $f(\xi)$ can be selected as:

$$f(\xi)=\begin{cases}\dfrac{\Delta s_0}{a_e^M}\left[(1-\xi)\ln(1-\xi)+\xi\right]+(\mu_1^e+\mu_2^e)\xi, & \dot{\xi}>0\\ -\dfrac{\Delta s_0}{a_e^M}\left[\ln(\xi)-1\right]+(\mu_1^e-\mu_2^e)\xi, & \dot{\xi}<0\end{cases} \tag{3.12}$$

Liang and Rogers [73] presented a constitutive model based on a cosine function $f(\xi)$, as follows:

$$f(\xi)=\begin{cases}\displaystyle\int_0^{\xi}\frac{\Delta s_0}{a_c^M}\left[(\pi-\cos^{-1}(2\tilde{\xi}-1)\right]d\tilde{\xi}+(\mu_1^c+\mu_2^c)\xi, & \dot{\xi}>0\\ \displaystyle\int_0^{\xi}\frac{\Delta s_0}{a_c^A}\left[(\pi-\cos^{-1}(2\tilde{\xi}-1)\right]d\tilde{\xi}+(\mu_1^c-\mu_2^c)\xi, & \dot{\xi}>0\end{cases} \tag{3.13}$$

where π is the thermodynamic force as a function of ξ.

Boyd and Lagoudas [64, 65] developed a polynomial constitutive model based on a polynomial function $f(\xi)$, presented as:

$$f(\xi)=\begin{cases}\dfrac{1}{2}\rho b^M\xi^2+(\mu_1^p+\mu_2^p)\xi, & \dot{\xi}>0\\ \dfrac{1}{2}\rho b^A\xi^2+(\mu_1^p-\mu_2^p)\xi, & \dot{\xi}>0\end{cases} \tag{3.14}$$

The quantities a_e^M, a_e^A, μ_1^e, a_c^M, a_c^A, μ_1^c, b^M, b^A and μ_1^p are material constants, while μ_2^e, μ_2^c and μ_2^p are introduced to enforce continuity for the function $f(\xi)$ during forward and reverse transformation.

The model is also numerically implemented using the concept of return mapping algorithms, presented previously in Figure 3.7. A description of the implementation is provided in the research paper by Qidwai and Lagoudas [74]. The current implementation of the subroutine follows the specifications for user-material subroutines by ABAQUS. However, the subroutine can be integrated into any other standard finite element or computational program. The subroutine can be used in 3D, 2D plane strain and generalised plane strain, and 1D problems.

This formulation is also used in this work, but it is not the one employed with the parameter search methodology, due to the lack of reproducibility of minor loops (especially the unloading part of the stress-strain curve). This is shown in more detail later in Chapter §8. For this reason, this formulation is used only for illustrative purposes, and it is not fully detailed here.

3.5.3. Considerations on Shape Memory Alloys Formulations

There are other formulations to model the behaviour of SMA that can be found in the literature [61, 62, 75-80]. However, most of these are not open-source, and their implementation is not a straightforward procedure. The physical basis behind the numerical codes must be well understood before any attempt is made to implement them. In general, some of the formulations tend to include:

- Dependence on the R-phase.
- Transformation-induced plasticity.
- “Calibration” and “correction” factors based on specific experiments.
- Tension-compression asymmetry.

The above factors add more material parameters to the formulations, not desired in the current work, where the goal is to infer NiTi properties by searching their “optimised combination” in a multidimensional parameter space.

3.6. Summary

The following conclusions can be drawn from this chapter:

- Crystallographic aspects of NiTi alloys have been exploited, showing that NiTi exhibit a parent phase with the CsCl crystal structure (B2). The transition to monoclinic (B19') can take one of three transformation paths, depending on factors such as chemical composition, heat-treatment and thermomechanical history.

- The literature on NiTi has a consensus among researchers that Type II twinning is the most prevalent twinning mode in this material.

- There is a narrow band in the phase diagram within which NiTi compounds are located. This region is located around the equiatomic composition (50NiTi at. %).

- There are phenomenological approaches for prediction of the mechanical behaviour of superelastic NiTi. These formulations are capable of simulating the behaviour of complex shapes under loading/unloading by using material input parameters obtained from uniaxial mechanical testing. Two main formulations have been selected based on their applicability in the field. Both approaches assumed that the material is a continuous and isotropic medium, and they have been briefly described in this chapter.

4. INSTRUMENTED INDENTATION OF MATERIALS

4.1. Introduction

Instrumented indentation is a type of mechanical testing where a load is applied to a hard tip with a defined shape (see Figure 4.1) to push it into the surface of a material, while monitoring both displacement and force as a function of time. In this regard, the method developed by Oliver and Pharr has been largely applied to infer Young's modulus of elasto-plastic materials from indentation data (P-δ), obtained during one cycle of loading and unloading [81, 82]. However, in this present work, this method will not be used since superelastic NiTi alloys experience phase transition upon loading. For this reason, this methodology will not be fully described in this section. The fundamentals of Oliver and Pharr's method are presented in Appendix §12.1, as well as some considerations about Hertzian contact theory for spherical indentation.

4.2. Hardness Testing

The "hardness number" has been in use for a long time. It does not necessarily need instrumented indentation to obtain this quantity since it does not depend on displacement measurements. Standard indenter shapes that can be used for this purpose (and for instrumented indentation) are shown in Figure 4.1.

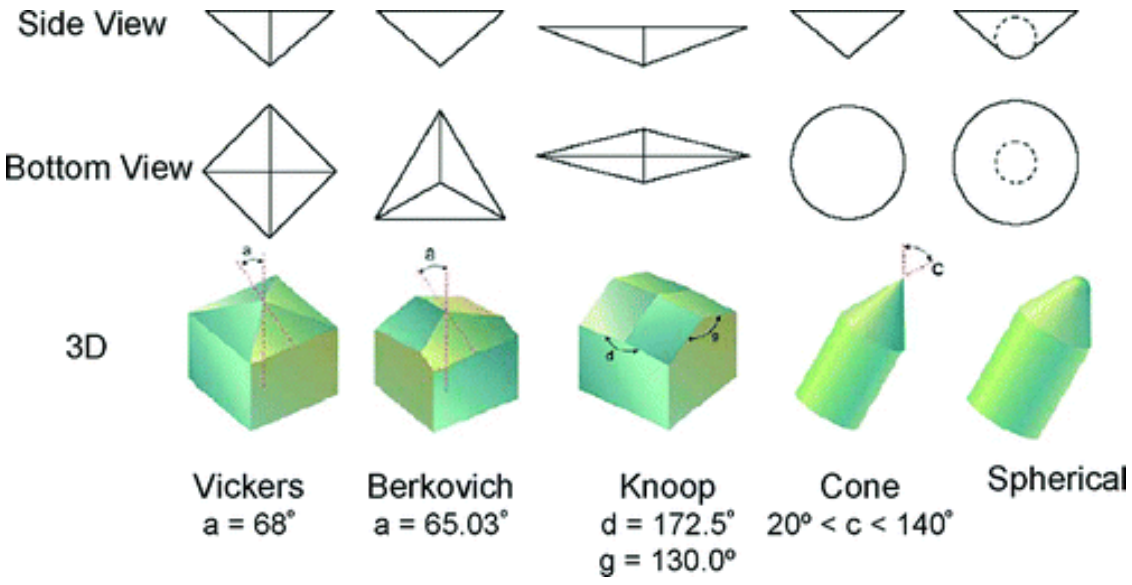

Figure 4.1. Types of standard indenter tips [83].

In fact, hardness should not be considered a well-defined material property. It is defined as a load divided by a contact area (thus, it is, in a crude way, a stress that does not mean anything much). This should be obvious from the fact that different types of hardness test give different hardnesses, and even the same test gives different hardnesses with different applied loads. It is a measure of the resistance to plastic deformation, and it does depend (in an ill-defined way) on the yield stress and the work hardening characteristics. In reality, it is related to some sort of average of the flow stress over the range of strain induced during the test (which is why it varies with applied load). In this regard, hardness testing only gives a semi-quantitative outcome of an indentation operation [10].

In the context of NiTi alloys, it is even more difficult to find a physical meaning for this “hardness number”. In addition to the above, the material undergoes phase transition (partially- and fully-transformed regions). Any attempt to interpret this number would be associated with a mixture of phases together with conventional plasticity. Again, this amalgamation of many phenomena would be far away from representing a genuine material property.

It is worth noting that there are assumptions incorporated into this hardness testing. The elastic recovery of the specimen, for example, is neglected. Furthermore, in practice, the specimen may exhibit “pile-up” or “sink-in” around the indent, such that the true area of contact (A_c) differs from that obtained from the “measurement” of the projected area (A) [82].

4.3. Issues Related to Indentation Experiments

Indentation experiments can be affected by a number of issues that need to be carefully addressed. It is worth noting that many of these issues become less important as the scale of the indenter increases. The extraction of material properties from indentation data depends on the accurate measurement of three variables: load, displacement and time. The most relevant issues related to experimental indentation data that may be considered to infer material properties reliably are listed as follows:

- Compliance: accurate analysis of frame compliance is an essential component of instrumented micro and nanoindentation experiments. In load frames of finite

stiffness, the load applied by the indenter induces a displacement in both the sample and the load frame. Frame compliance must be identified and subtracted from the total indenter displacement to account for sample deformation [84, 85].

- Friction: frictional effects between the indenter and the specimen surfaces can play a role in indentation, especially sharp indenter shapes [86]. In some cases, friction can affect the radial stress distribution below the indenter, which can alter the degree of “pile-up”. An analysis assuming smooth contact is commonly adopted in simulated indentation. However, limited studies have been performed to investigate the possibility of deviation due to this simplification. The literature on this topic has shown that these effects can affect the reverse analyses, carried out based on simulated results ignoring friction to predict material properties, which can be adversely inaccurate [86, 87].

- Temperature changes (thermal drifts): errors can be caused by a gradual change of either specimen or instrument dimensions due to thermal drifts. This results in (thermal) contractions and expansions, which are incorporated into measured displacements of the indenter tip [88]. Thermal drift is a standard issue in nanoindentation experiments. Several procedures are used to mitigate the thermal drift effects. The simplest one is to assure that measurements are taken at equalised temperatures (specimen, indenter). Another approach corrects the measured values by subtracting the displacement caused by thermal drift. In this case, a dwell time is applied during the unloading part of the test to measure the velocity of the indenter movement due to the drift. This velocity is then used in a model for drift correction [89].

- Surface roughness: this could be a great source of errors, if large when compared with the indentation depth. Even the best-polished specimens have surface undulations of height from several nanometres to several tens of nanometres and with the distances between individual hills of tens of nanometres and more. Consequently, the indenter comes first into contact with the highest asperities [88]. On loading, the tips of the highest asperities are compressed, and the indenter gradually comes into contact with lower asperities, etc. The specimen surface conforms more and more with the indenter, and the response gradually approaches that for the perfect contact [90]. A role is played not only

by the shape of the asperities and by the distribution of their heights, but also by their density, by the radius and shape of the indenter tip and also by the elasto-plastic properties of the specimen.

- Indentation size effect: this effect is observed in terms of variations in hardness. When indenting a material with a sharp indenter at shallow penetrations, the hardness often increases by decreasing the penetration depth. This is known as the indentation size effect (ISE) and becomes observable for indentation depths smaller than several μm [88]. The ISE also occurs with spherical indenters, although here the apparent hardness does not depend on the depth, but increases by decreasing the indenter radius [91]. Even some ceramics exhibit a size effect to a small extent [92]. There are several reasons for depth-dependence of hardness in metals: a thin hard surface layer might have been formed on the specimen surface during its preparation, the bluntness of the tip of the indenter, etc. For a given load, the penetration of a real indenter is thus smaller, and the hardness appears to be higher. By increasing the penetration depth, the influence of bluntness becomes smaller, and the measured hardness values approach gradually to those for the ideal shape [93].

- Microstructure: indentation techniques are often used to perform measurements on length scales that are sub-micron. There is also an issue related to the location of an indent or, more precisely, the size of the indent relative to grain size. In this case, some microstructural feature should be considered, such as dendrites, precipitates, etc [94-96]. For the specific case where the indent is smaller than the average grain size, then it is likely that it will be located within a single grain. Thus, the measured load-displacement curve will be specific to that particular grain, and its orientation with respect to the loading axis. In such cases, these curves will not represent the “bulk” behaviour of the material. The significance of the difference between “single grain” and “bulk” behaviours to indentation depends on crystallographic anisotropy and the texture of the sample. In order to determine constitutive relations that are representative of the bulk, it is important that a representative volume of material is interrogated [7, 97].

4.4. Basics of Finite Element Modelling Applied to Indentation

Finite element analysis solvers are powerful tools to model indentation, as seen in Figure 4.2 [9, 98].

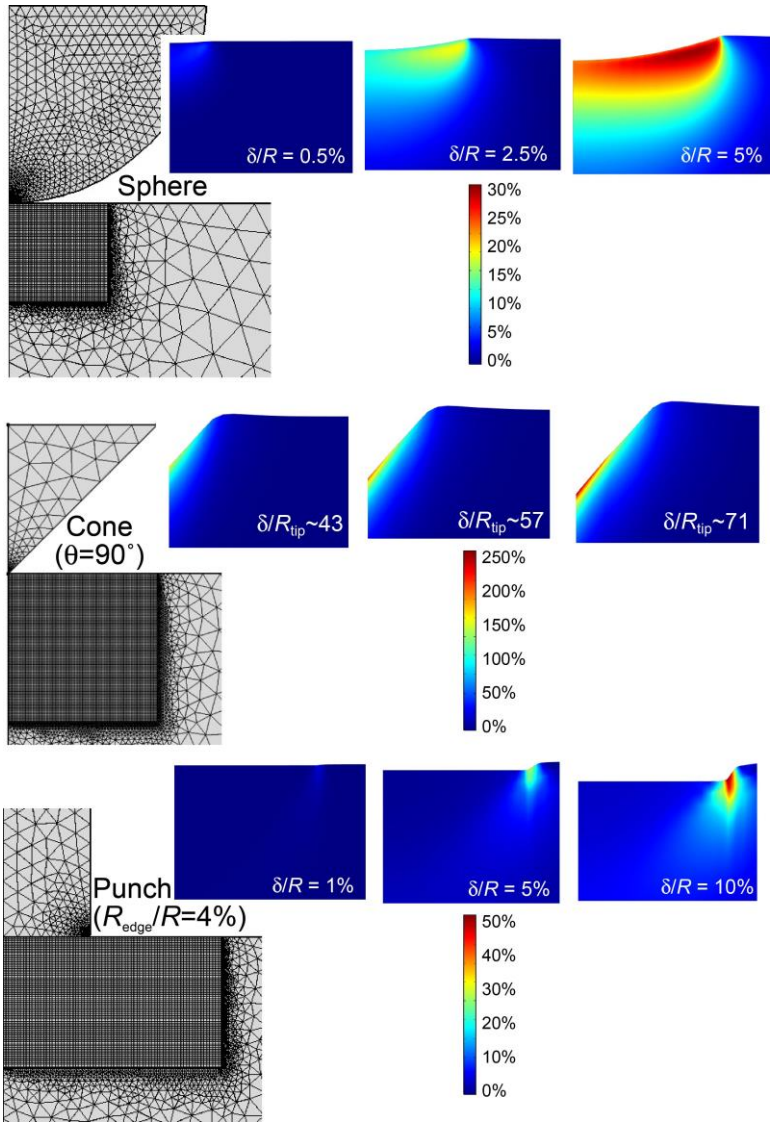

Figure 4.2. FEM meshes used for the sphere, cone and cylindrical punch, with corresponding fields of (von Mises) plastic strain after three different extents of penetration [9].

When the response of the material is only elastic, the stress field at the contact region is well-defined, regardless of the indenter shape. However, for elasto-plastic, viscoelastic or superelastic materials, this task becomes more complicated, due to the existence of complex stress fields, particularly for Berkovich or Vickers indenters. This is caused by a 3D phenomenon associated with large plastic strain fields [99]. In this case, the finite element method (FEM) is a valid methodology to predict stress distribution and displacements during loading and unloading processes.

However, experimental indentation techniques have a few drawbacks, such as compliance issues and thermal drift in high-temperature environments, as discussed in §4.3, which may lead to significant errors in the load-displacement plots.

Some work has been done on using FEM to model the indentation process, as follows: thin film properties [98, 100, 101], coating fracture and substrate plasticity [102], properties of superhard coatings [103], elasto-plastic transition regime [104], indentation of hard multilayer coatings [105], properties of aluminium alloys [99]. Thus, this method of analysis is of interest to both academia and industry. In this regard, FEM can be used to predict the load-displacement plot during indentation, for a material with a given (uniaxial) stress-strain curve, assumed to be applicable to von Mises stress and strain for multi-axial situations, and for any given indenter shape. An example of FE modelling applied to indentation is shown in Figure 4.2. The meshes used are shown, corresponding to the three indenter shapes used in these simulations. The plastic strain fields are also shown at three different penetration depths for the parameter set in Table 4.1.

Parameter	Symbol	Value
Yield Strength	σ_Y, MPa	300
Work Hardening Coefficient	K, MPa	1000
Work Hardening Exponent	n	1

Table 4.1. Plasticity parameters used in FE simulations of indentation tests [9].

It is worth noting in Figure 4.2 that the strain fields are substantially different for these three cases, both regarding the distribution of the strains and their magnitudes. Furthermore, for the only self-similar shape (the cone), the nature of the strain field is independent of penetration (although the magnitude of the strains does increase with penetration), whereas for the other two (non-self-similar) shapes, it is not [9]. Another issue related to the sharp indentation that can be addressed by FEM is the high-stress region below the tip, as expected. This might be a problem while running simulations. It can be overcome by refining the mesh at that specific region which will cause an increase in the computational time.

4.5. Extraction of Plasticity Parameters from Indentation Data

FEM simulations have demonstrated their ability to obtain predicted load-displacement curves [106, 107], by using pre-specified stress-strain parameters, which agree quite well with those obtained experimentally. Unfortunately, the inverse problem/analysis − i.e. the inference of constitutive relations from observed behaviour during indentation − is not that straightforward.

Dean et al. [7] established some underlying factors that make the inverse problem complex and challenging:

- The relatively low sensitivity of measurable behaviour (such as load-displacement plots) to the characteristics being sought.
- The fact that these characteristics incorporate several degrees of freedom (e.g. unknown values of yield stress and work-hardening rate as a function of strain).
- The relatively high sensitivity of measurable behaviour to various factors, such as physical boundary conditions (such as frictional effects [108], material anisotropy [96, 109], tip shape imperfections [110], etc).

In this regard, some FE-based methodologies have been proposed [111-118]. All these methods require the coding of material subroutine scripts based on the corresponding theories. Although several material constitutive relations have been used in FE simulation, very few research papers have shown transparent comparisons with real experimental data [9-11, 114], used to infer material properties from reference indentation data obtained experimentally. These approaches are based on optimising a “quantity” that gives the amount of agreement between modelled and experimental curves. These methodologies are defined on the basis that a single combination of material properties and boundary conditions will result in the observed experimental conditions. Proceeding from this assumption, it is possible to iterate the possible material parameters for given boundary conditions and a given constitutive relationship until the properties lead to results that agree closely with experimental observations. A crucial step in using these methodologies is to select a material constitutive model that can capture the central mechanical responses of the material subjected to indentation. The one chosen was the Ludwik-Hollomon expression:

$$\sigma = \sigma_Y + K\varepsilon_P^n \tag{4.1}$$

where σ is the applied stress (von Mises), σ_Y is its value at yield, ε_P is the plastic (von Mises) strain, K is the hardening coefficient, and n is the work hardening exponent.

Chen et al. [114] proposed an indentation elastoplastic constitutive relation based on Equation 4.1 and σ_Y was discretised to allow for the minimisation of the residual between an experimental depth-time reference curve and the corresponding FE simulated curve. This was performed by a gradient-based nonlinear least square technique. Although this method is claimed to work well, there are many functions to be considered, and the complexity of the iterative process makes it hard to be reproduced. Furthermore, there is no information on the sensitivities (e.g. on how each variable influences the overall outcome of the process).

On the other hand, Dean and Clyne [9] developed a methodology based on running repeated FEM modelling, with the predicted outcome (load-displacement plot) being systematically compared with experiment. The “correct” property values are found by searching for the combination giving the maximum value for a “goodness of fit” parameter, measuring the agreement between experimental and predicted outcomes. This agreement ranges from 0, for no agreement, to 1, for perfect agreement. This is a novel approach that offers considerable promise for the clear and precise characterisation of plasticity via a single indentation run with a spherical indenter.

A comparison of the predictions obtained with the experimental data for (a) the load-displacement plot and (b) the stress-strain curve is shown in Figure 4.3. The latter shows that, while neither inferred plot conforms closely with the experimental one (no plot of Equation 4.1 can do this), they are both giving reasonably accurate descriptions. It is reasonable to suppose that, for a material with a stress-strain curve conforming closely to the assumed functional form, the (unique) solution, in the form of the three parameter values, could be accurately obtained.

Another drawback related to this “simple” inverse iterative FEM procedure is that it requires the user to carry out dedicated FE modelling for many combinations of the parameter values. Based on this, it is worth mentioning that the inverse problem has considerable scope for ambiguity (e.g. different stress-strain relationships giving

effectively the same load-displacement plot), as seen in Figure 4.3(a). This problem is the main obstacle to this approach [7, 8, 111, 112, 119].

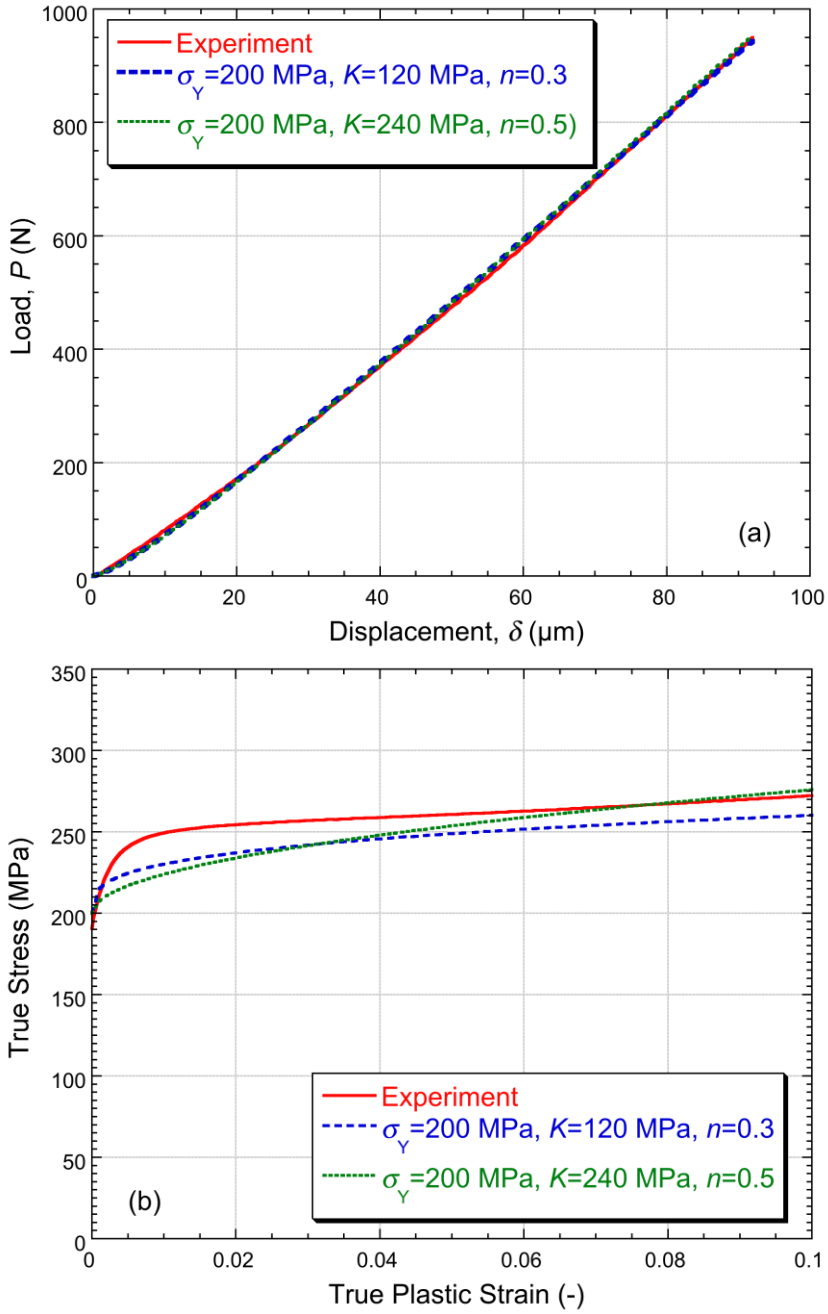

Figure 4.3. Comparison between experimental data and predictions based on the use of Equation 4.2, with the two parameter sets shown (inferred via inverse FEM), for (a) the indentation load-displacement plot and (b) the uniaxial stress-strain curve [9].

Campbell and co-authors [11] have overcome this problem by developing a systematic search algorithm, based on the Nelder-Mead minimiser [120, 121]. This algorithm searches for a combination of parameters that minimises the "goodness-of-fit" quantity in a 3D parameter space. Many metals were used in this

study and anisotropy was also investigated. The convergence procedure generally required only a relatively small number (a few tens) of iterations, although this does depend on the level of accuracy being sought. Some features of the convergence are apparent in Figure 4.4, where it can be seen how the movement through parameter space took place for one of these materials.

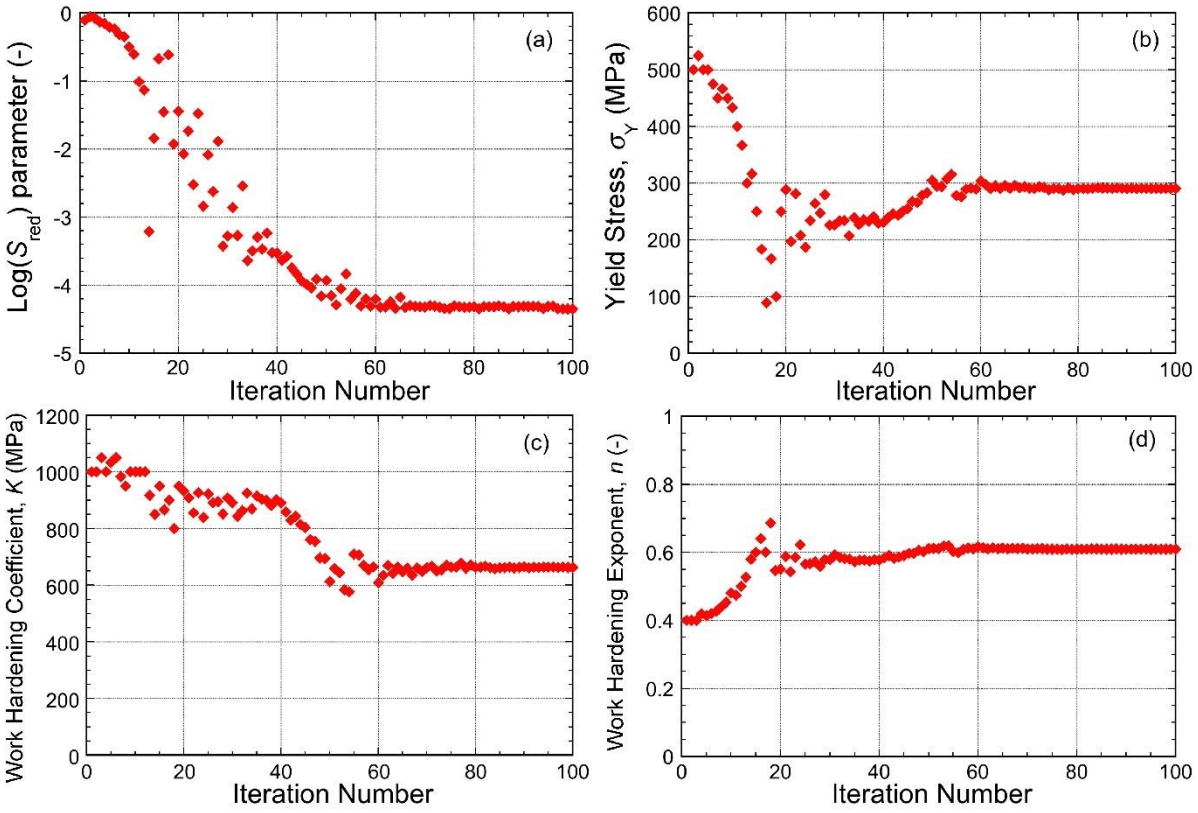

Figure 4.4. Nelder-Mead convergence on an optimal (Ludwik-Hollomon) parameter set, targeting a load-displacement plot from indentation of a brass sample, showing the evolution with iteration number of: (a) the goodness-of-fit parameter, S_{red}, (b) yield stress, (c) work hardening coefficient and (d) work hardening exponent [11].

The starting values were selected in a fairly arbitrary way and, as it can be seen, they were not very close to the optimal values in this case. If they happened to be either very close to, or differ substantially from the optimal set, then that would affect the efficiency of the convergence. However, there would not, in general, be very much difference between the number of iterations required in the two cases. On the other hand, there will always be a requirement for more than just a few iterations, even if the starting positions are quite close.

A comparison (for all three metals) is shown in Figure 4.5, between uniaxial stress-strain plots (axial and radial) and those obtained via Nelder-Mead convergence

on best-fit parameter combinations. This has been done using the Ludwik-Hollomon expression for all three metals. It can be seen that the level of agreement is very good. It could be quantified in several ways, but in all cases, the predicted curves are within about ±5% of the average of the axial and radial uniaxial plots, over the complete strain range.

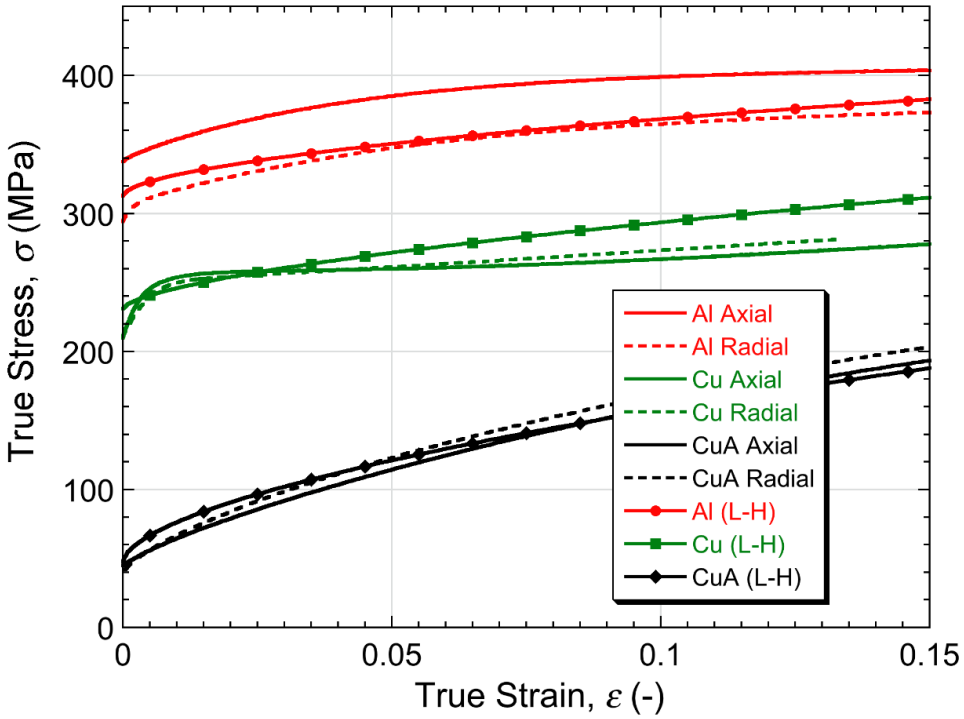

Figure 4.5. Comparisons between experimental stress-strain curves (axial and radial directions) and corresponding plots of constitutive laws, using the parameter values obtained by iterative comparison between measured and modelled indentation load-displacement data. These comparisons are shown for Al, Cu and annealed Cu [11].

This is certainly acceptable for most purposes, and indeed it might be argued that uniaxial data can rarely be considered reliable to higher precision than this. In general, similar inferred stress-strain curves were obtained using the adopted constitutive law.

4.6. FE Modelling of the Indentation of Superelastic NiTi

4.6.1. NiTi Behaviour under Indentation

The current theories and models in use deal mainly with the deformation of single-phase materials and are not appropriate to explain the behaviour of materials that experience phase transition during indentation tests [81, 82]. Recent efforts have been made on extending such techniques to study the mechanical properties of

multi-phase materials such as, for example, SMA [122]. The main issue behind inferring the mechanical properties of superelastic materials, such as NiTi, for using indentation techniques, lies in coupling both deformation and reversible martensitic transformation of NiTi under indentation conditions. This makes the interpretation of such results quite challenging. In this regard, FEM predictions of stress/strain fields induced by indenter tips are very useful to enhance the understanding of the behaviour of NiTi under such complex loading conditions [15, 24, 25, 122-125].

Muir Wood and Clyne [15] simulated the peak of strain levels for two shapes of indenter tips, spherical and conical, during indentation of martensitic and superelastic NiTi alloys, as shown in Figure 4.6.

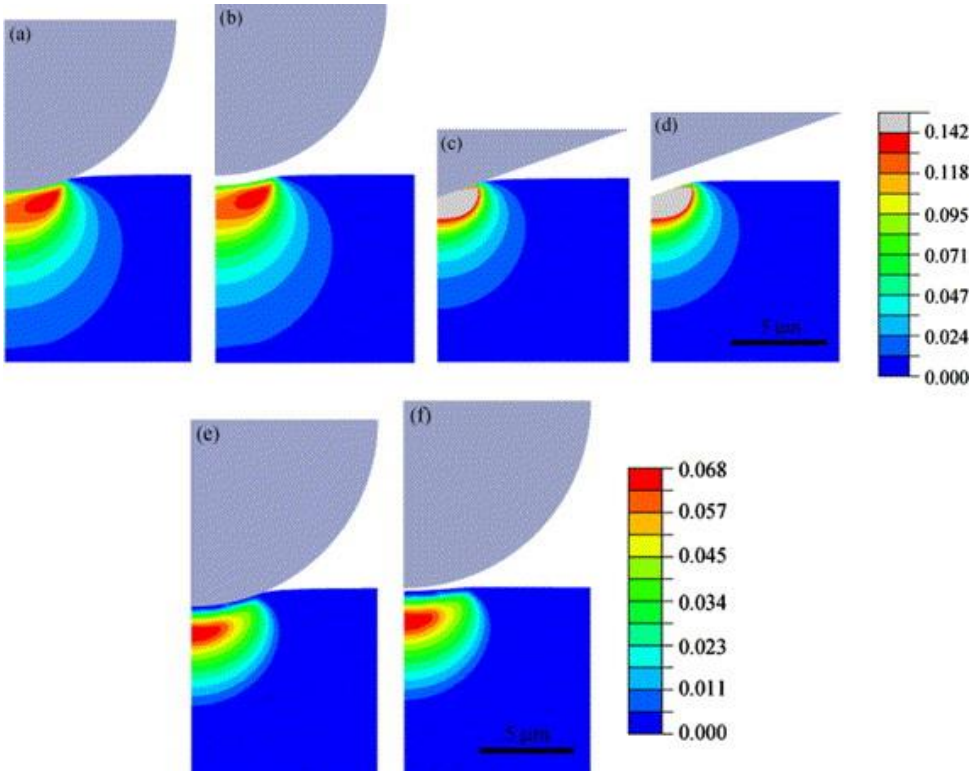

Figure 4.6. Predicted distributions of equivalent plastic strain during and after indentation of martensitic NiTi (a-d) and parent phase NiTi (e and f) [15].

Strain fields are predicted at (a) maximum loading and (b) after unloading for an indenting sphere, and at (c) maximum load and (d) after unloading for an indenting cone into NiTi martensite. For the spherical indenter, strain fields for the superelastic case are also shown at (e) maximum load and (f) after unloading.

In this case, the built-in UMAT for superelastic materials in ABAQUS was used [60, 63, 66]. As expected, the conical indenter tip generated extremely high strains beneath an indenting cone and, for that reason, it was not possible to predict the superelastic behaviour for that case. On the other hand, with the spherical indenter, indentation could be simulated, for both martensitic and superelastic NiTi. However, the analyses of the load-displacement curves obtained experimentally and compared to those from the FEM simulations, shown in Figure 4.7, showed some discrepancies. These are likely to be expected because the interactions between plastic and superelastic strains will, in reality, be highly complex during indentation. Furthermore, these discrepancies could be related to deficiencies with the indentation rig (§4.3).

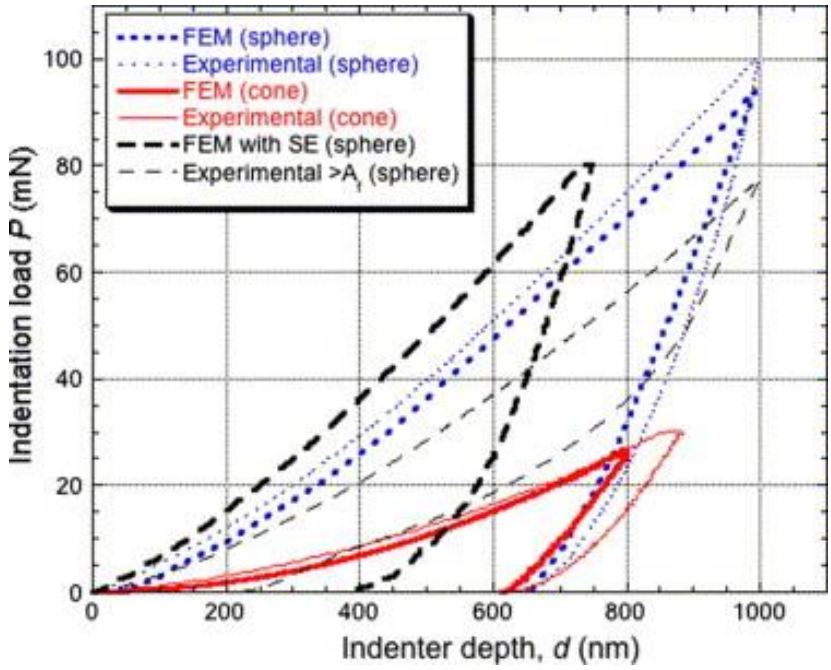

Figure 4.7. Comparison between predicted and measured load-displacement curves during loading and unloading, with spherical and conical indenters and, for the case of the spherical indenter, for both martensitic and superelastic NiTi alloys [15].

Further development of both experimental set-up and simulation algorithms for combined superelastic/plastic straining are required before they can be applied reliably to the indentation process.

Kan et al. [122], Zhang et al. [28] and Perlovich et al. [124] also used FE-based models to predict the behaviour of NiTi beneath an indenter tip. An example of a modelled load-displacement curve of SE NiTi subjected to spherical indentation is shown in Figure 4.8. The modelled unloading process consists of three stages: the

elastic unloading of a mixture of austenite and martensite phases, reverse transformation and austenite elastic unloading. In practice, for an experimental case, the unloading can incorporate some plasticity or residual martensite.

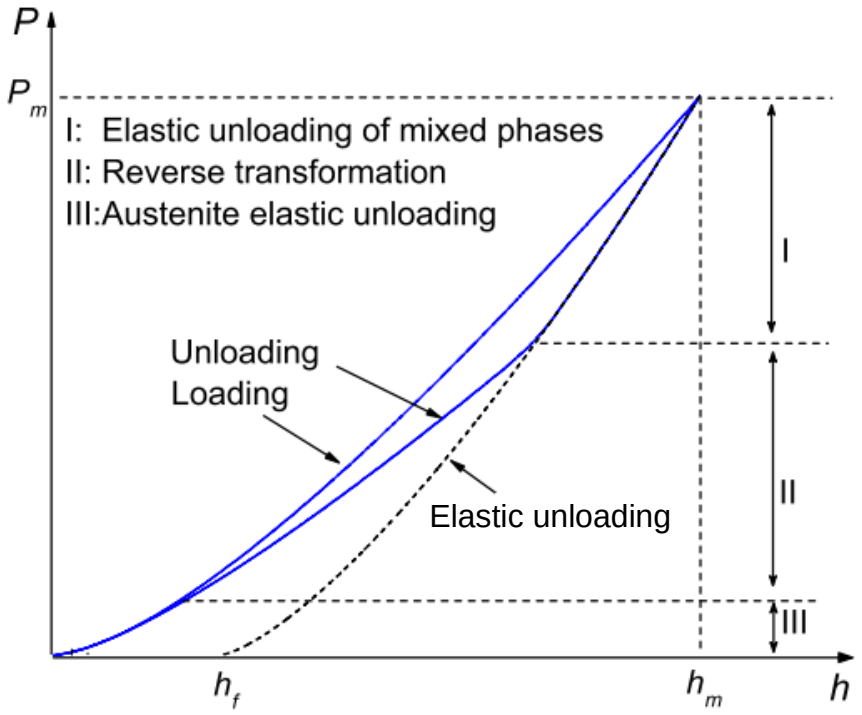

Figure 4.8. Typical spherical indentation modelled load-displacement curve with both upper (loading) and lower (unloading) paths for a generic SE NiTi alloy [122].

Frost and co-workers [24] developed a constitutive model that captures the two-stage martensitic transformation via the intermediate R-phase. The inputs for this model included the elastic properties of NiTi, as well as the phase transition temperatures (including R-phase) and fitting coefficients. The spherical indentation was modelled using this approach. Information on spatial distribution of the minimum principal component of strain (b) and volume fraction of phases at maximum penetration depth (c and d) is provided in Figure 4.9. As expected, the most deformed region is fully martensite. During loading, as presented in Figure 4.9(c), the material has three different stages: a single austenitic phase at the initial stage, a partially-transformed zone (A-M) at the second stage, which is surrounded by the austenitic phase and a fully-transformed martensitic zone at the final stage, which is surrounded by a partially-transformed zone enclosed by the austenitic phase.

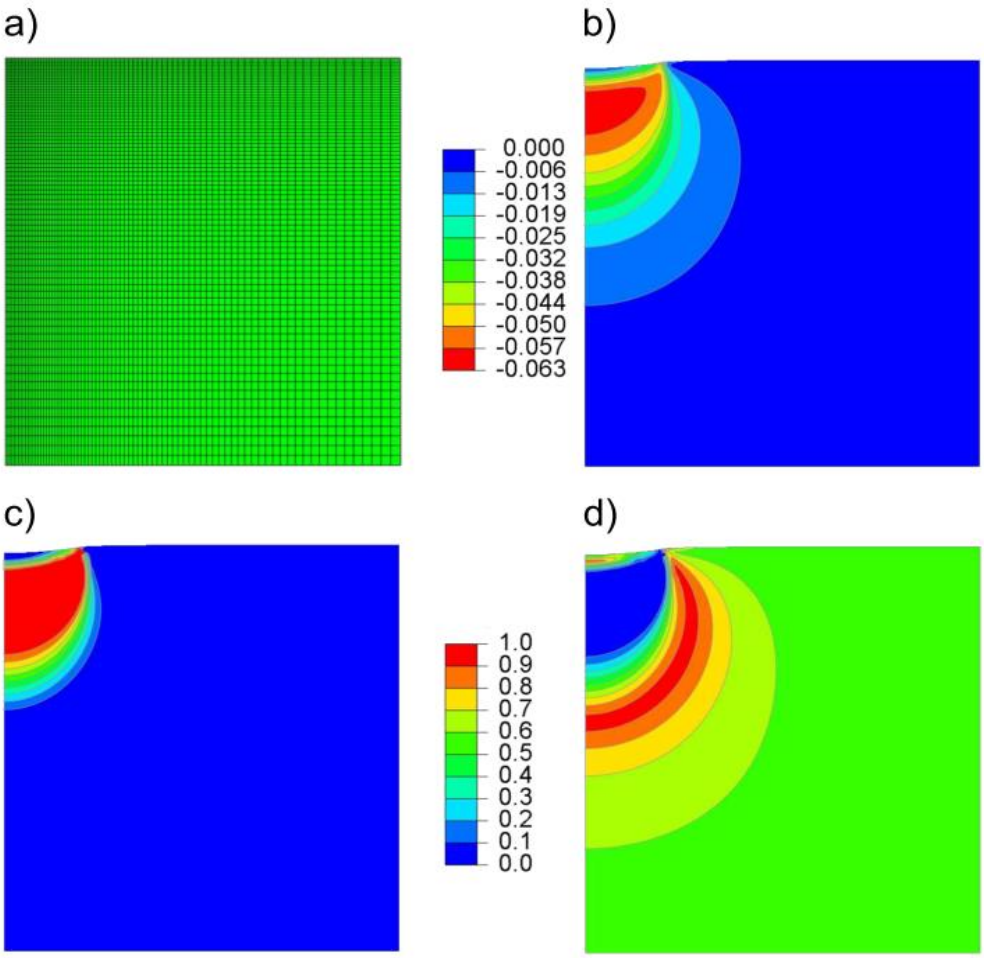

Figure 4.9. (a) FE model mesh, (b) distribution of the principal component of logarithmic strain, (c) Volume fraction of martensite and (d) volume fraction of R-phase for spherical indentation at 42nm in depth at 0°C [24].

A comparison between modelled (using the formulation proposed by Frost et al. [24]) and experimental load-displacement curves for two different types of indenter shapes is shown in Figure 4.10. For the spherical indentation case, at the maximum depth of 42 nm, the material clearly exhibited SE behaviour, since there was no residual depth on unloading. For the indent carried out at 65 nm, a residual deformation was detected, indicating the occurrence of conventional plasticity. This agrees with what had been established by the FE simulation, which predicted a superelastic limit of ~60 nm. For the Berkovich indenter, the agreement was reasonably good up to the point that no irreversible processes were involved. Also, some cyclic loading/unloading experiments were performed just to confirm the reversibility of the transformation in the material.

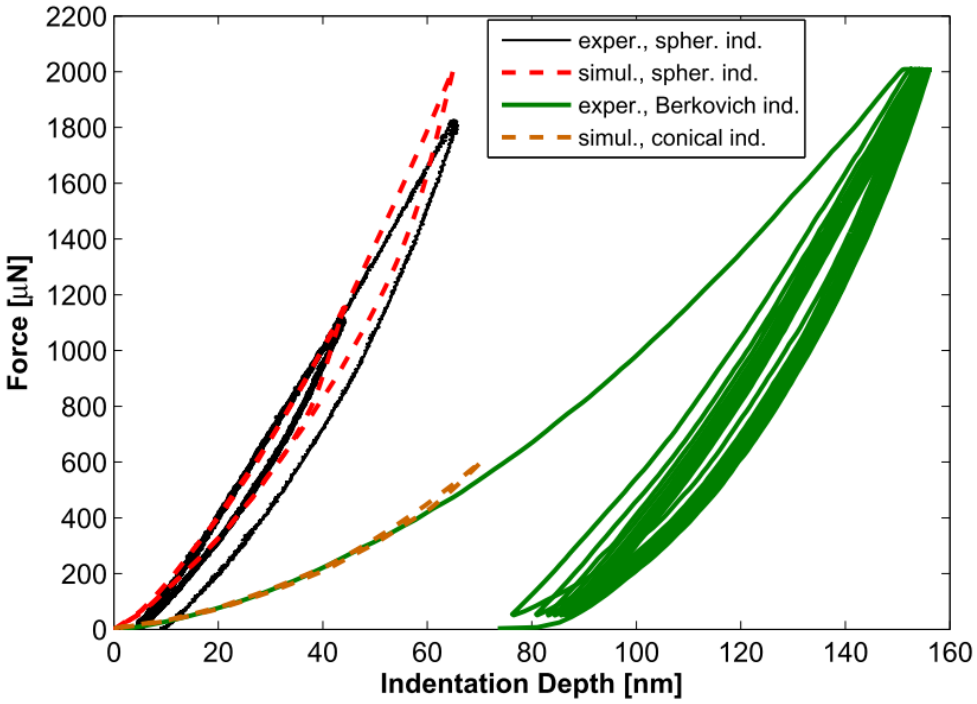

Figure 4.10. Comparison between modelled and experimental load-displacement curves obtained at 25°C for two types of indenter shapes: sphere and Berkovich [24].

4.6.2. Extraction of Superelasticity Parameter from Indention Data

Regarding inferring stress-strain characteristics from indentation data (FE-inverse analysis), there is no consolidated literature, as applied to superelastic NiTi.

Kan et al. [122] developed a method, based on theoretical analysis and numerical simulation, to determine the elastic moduli of austenite and martensite by using spherical indentation test with Oliver-Pharr's method (§12.1). This approach introduced a "weighting factor", based on FEM simulations, which accounts for the effects of the martensite during the phase transition upon loading (see Figure 4.11). This was an idealised numerical problem, that is, a modelled experiment of a spherical indentation. In practice, both non-idealised indenter tip (with compliance) and noise of experimental curves will introduce some additive errors into the proposed method. Further experimental validation will be needed.

Yan et al. [16, 125] proposed an approach to infer transformation stresses of superelastic NiTi. In this analysis, it was assumed that there is no distinction between the elastic properties of the phases (E_A=E_M=E) and the phase transformation stresses start and finish at the same level. These simplifications imply that only two parameters

are left to be found: the forward stress (σ_f) and the reverse stress (σ_r). It was found that there are two characteristic points in the load-displacement plot: bifurcating and returning points, shown in Figure 4.11.

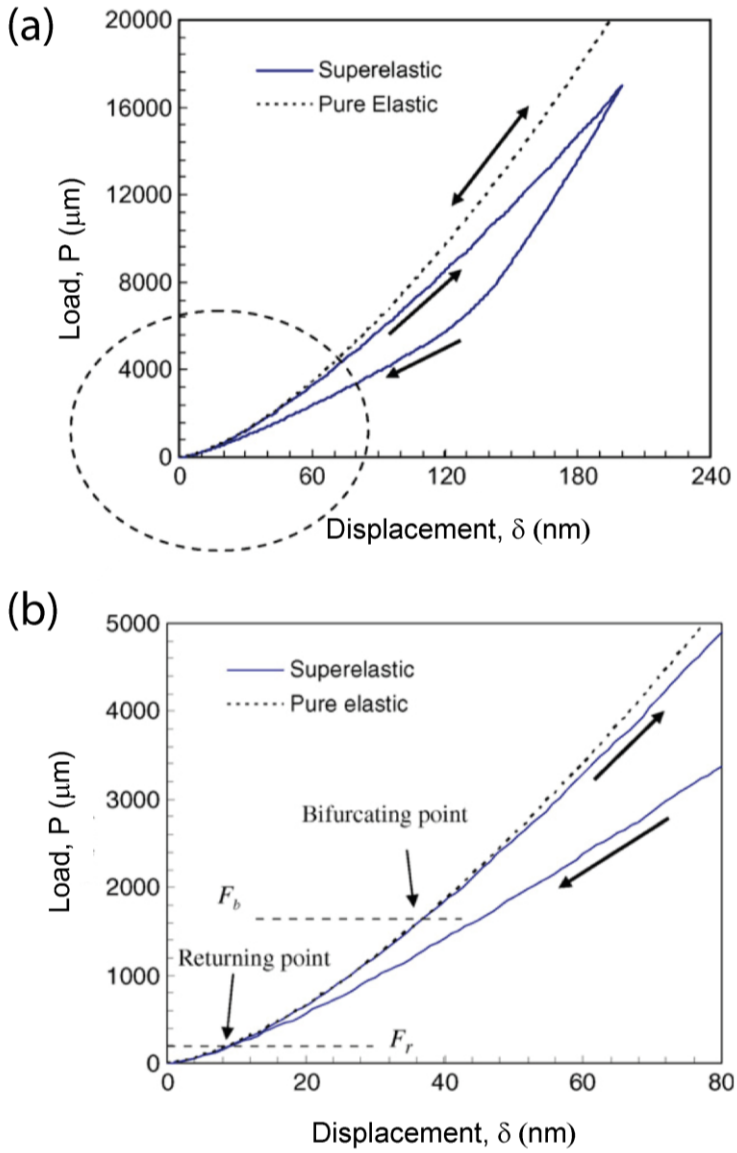

Figure 4.11. (a) Comparison between a pure elastic (dotted line) and a (solid line) modelled load-displacement curves with the same elastic constants, as in the austenitic phase, with (b) magnified area showing both bifurcating and returning points [16].

Right before the beginning of the forward transformation, the material is in a linear elastic state. Within small indentation depths (δ/R<0.001), Hertzian contact theory can be applied to describe this purely elastic contact problem. It was demonstrated that the elastic limit load, i.e. the bifurcation force (F_b), at the onset of phase transformation, is related to the martensite start stress (σ_{Ms}, forward transformation), and the return force (F_r), is related to the austenite finish stress (σ_{Af}, reverse transformation). Generally, the

proposed universal scaling function for both bifurcation and return forces can be determined by extensive FEM simulations [16, 125]. In the case of small deformation, this function can be determined analytically from elastic solutions. Although the transformation stresses can be determined in theory, in practice it is difficult to identify those specific loads, since there is no abrupt change in the load-displacement curve.

Perlovich et al. [25] proposed a function for determination of mechanical properties of superelastic NiTi. This was performed by running several indentation simulations (in ABAQUS) with spherical indenters of various geometries for different material datasets. For both approaches [16, 25], it was assumed that the moduli of both phases are known, and the phase transformation stresses start and finish at the same level, meaning that the stress-strain curves present two flat plateaus. This assumption implies that plots inferred from this method will not represent well the experimentally-obtained ones. Thus, only three parameters are left to be sought: forward stress (σ_f), reverse stress (σ_r) and transformation strain (ε_L). For the simulation, each one of these parameters was varied systematically. Each combination generated a load-displacement plot, from where the quantities unrecovered energy ratio and maximum indentation depth were extracted. This method has been tested on a NiTi alloy, superelastic at room temperature. The difference between mechanical properties obtained from uniaxial compression testing and this technique was found to be less than 20% for most specimens. It is worth noting that no (experimental) stress-strain plots were presented in these research papers.

4.7. Summary

The following conclusions can be drawn from this literature review chapter:

- The standard method for extraction of Young's modulus of elasto-plastic materials from indentation data is not well-suited for NiTi alloys. Indentation of such materials has more issues to be considered than for conventional elasto-plastic materials since these particular materials present a stress-induced transformation upon loading/unloading. The same applies to the interpretation of the "hardness number".

- There are issues that may strongly affect the outcome of indentation experiments. The most relevant ones, according to the literature, that may be considered are compliance, friction, thermal drifts, surface roughness, indentation size effects and microstructure. Some of these issues become less important as the scale of the indenter increases.

- There are FE-inverse methodologies already in the scientific literature which can be used to infer plasticity parameters. Very few provide clear information about the convergence procedures and other issues related to the model. Nevertheless, it was possible to identify a traceable methodology in this regard. This methodology has been used for conventional metals and the experimental results have proven to be compatible with the ones inferred via FEM.

- Research work on indentation experiments of NiTi has been found in the literature. Most of the experimental load-displacement curves do not agree well with the modelled ones (some do not agree at all). This might be related to some of the experimental issues mentioned above.

- There are very few papers approaching FE modelling of the indentation of superelastic NiTi by using the macroscopic mechanical behaviour. However, inferring stress-strain curves from indentation data is a much more complex problem. Unfortunately, there are only a couple of methodologies that claimed to have had approached this matter. They not only oversimplified the problem but also lack in both transparency and applicability. Thus, further work needs to be done in this direction.

5. EXPERIMENTAL TECHNIQUES

The experimental work in this research was based on the sequence of procedures shown in Figure 5.1.

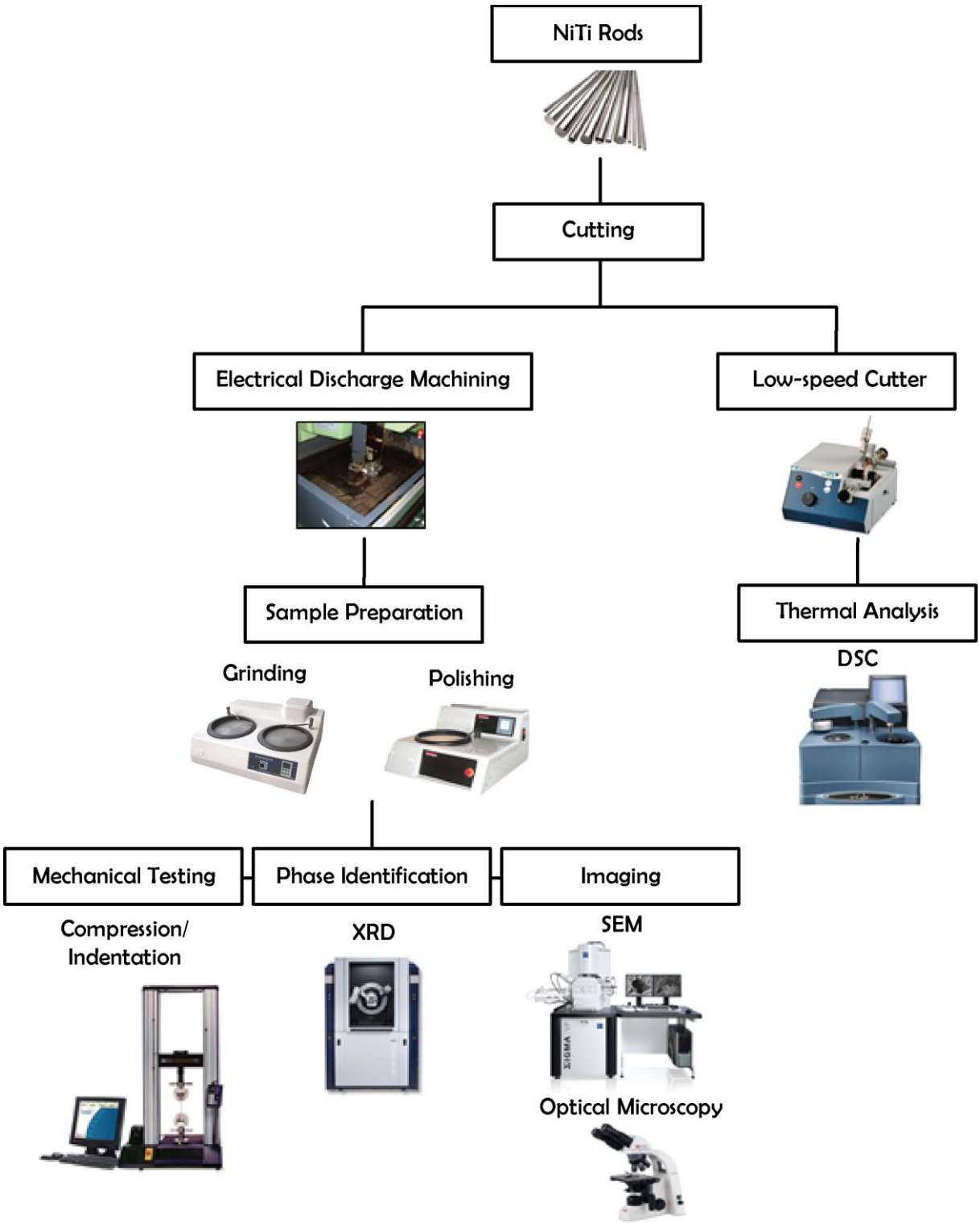

Figure 5.1. Sequence of procedures employed during the experimental work in this research.

5.1. Material Supply and Sample Preparation

The present investigation concerns a single type of sample. Rods of NiTi alloy ("Alloy BB") were obtained from Memry Metalle GmbH, specified as having an A_f (austenite finish) temperature of around -10˚C. This ensures that they should exhibit superelastic behaviour at room temperature (~20˚C).

These rods, which had been hot-worked and extruded, had a diameter of 13.3 mm and a length of 300 mm. They were sliced into sections of 3 mm in length by Electrical Discharge Machining (EDM). Then, the samples were hot mounted in a hot press, using a pressure of 20 MPa at a temperature of 150˚C for 8 minutes. After mounting, grinding was carried out on two different grades of SiC paper: 1200 and 2500 grit. The samples were then sequentially polished with alumina paste of 6, 3, 1 and 1/4 μm for 10 minutes each. Fine polishing was performed with Colloidal Silica 0.06 μm for 15 minutes. This is a polishing suspension that provides a chemical mechanical polishing action for soft metals that produced grain contrast without etching.

5.2. Differential Scanning Calorimetry

A schematic of DSC analysis is shown in Figure 5.2. This technique consists of measuring the difference in the amount of heat required to increase the temperature of a sample, compared with a reference (blank pan), as a function of temperature.

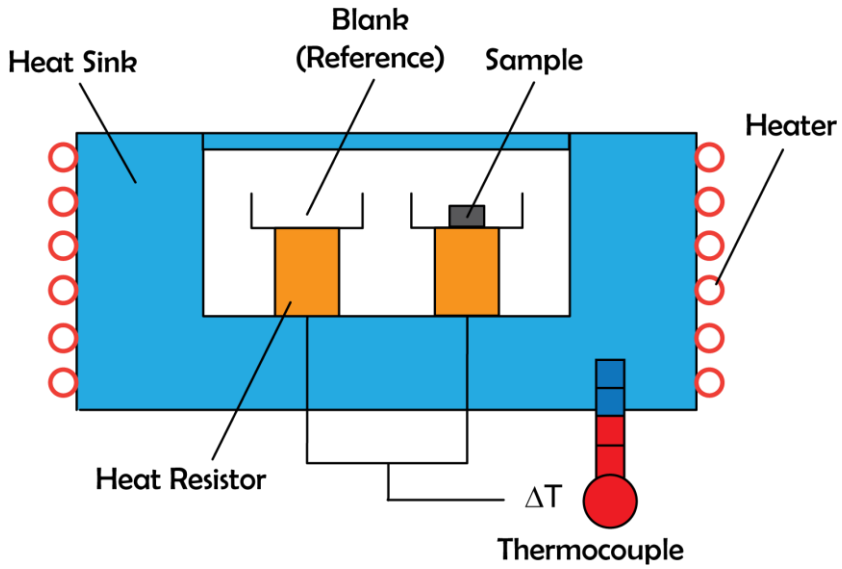

Figure 5.2. A schematic illustration of a DSC experiment.

DSC runs were carried out with a Q20 Thermal Analysis instrument to determine the transition temperatures. Small samples (~5 mg) were cut from the as-received rod and placed in a high-purity aluminium pan. Runs were performed over a temperature range between -150 and 100˚C, with heating/cooling rates of 10˚C min^{-1}. The transformation temperatures (martensite finish, M_f, martensite start, M_S, austenite start, A_S, and austenite finish, A_f) were determined according to ASTM F 2004-05 [126].

A typical resultant DSC plot is shown in Figure 5.3, where it can be seen that the transition temperatures M_S, M_f, A_S and A_f are respectively about -37˚C, -78˚C, -32˚C and -10˚C. As expected, this DSC curve shows that there is considerable hysteresis in the transitions. That confirms that the material should be entirely austenite at room temperature (in the absence of applied stress).

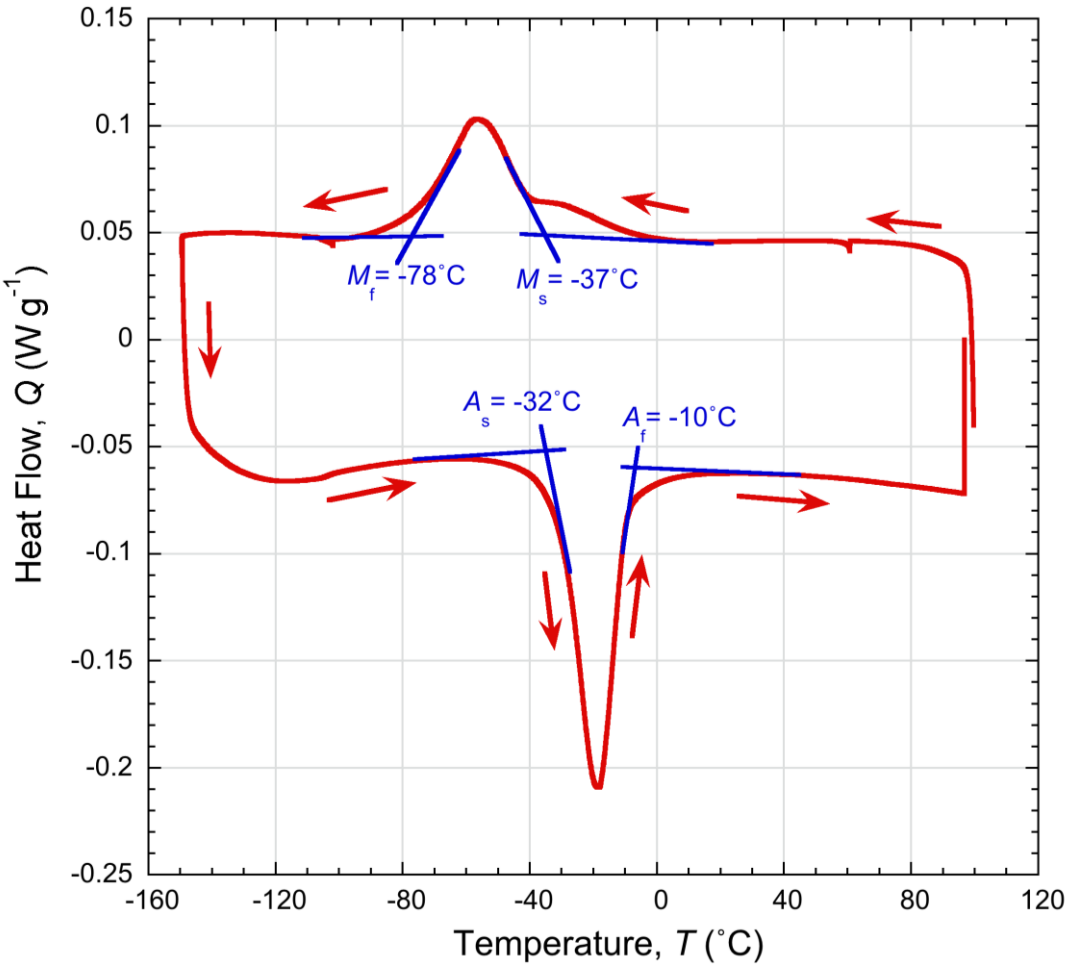

Figure 5.3. DSC curve, showing the values obtained for the transition temperatures M_S, M_f, A_S and A_f.

In Figure 5.3, the first peak that forms upon cooling represents the transformation from the parent phase to the martensitic phase. Upon heating, the observed peak represents the reverse transformation into the parent phase (B2).

The “shoulder” peak next to the martensite peak is too short to characterise a phase transition such as R-phase, which usually presents a peak of the order of the martensitic phase peak [127]. This “shoulder” could be attributed to machine calibration, thermal inertia and/or impurities in the reference pan, which possibly triggered a voltage peak when the material started transforming into martensite. These have all been reported in the literature [128] as a potential source of errors during DSC experiments.

5.3. X-Ray Diffraction

X-ray diffraction (XRD) was performed with a high-speed Bruker D8 Advance XRD system with Cu-K_α radiation, tube current of 40 mA, tube voltage of 40 kV and radiation wavelength of 1.5418 Å (λ in Figure 5.4).

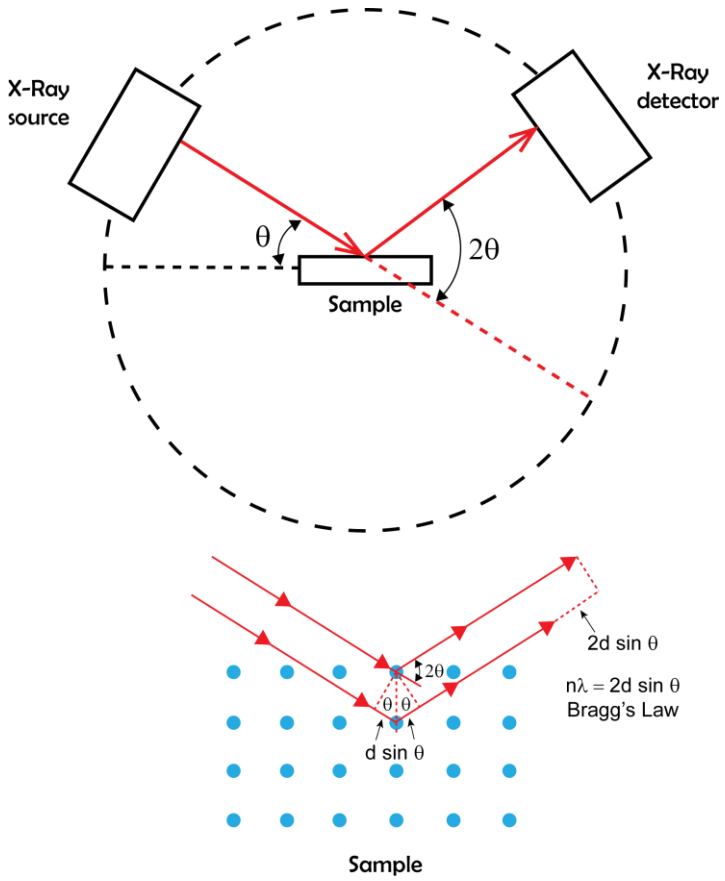

Figure 5.4. A schematic illustration of X-ray diffraction tests with Bragg’s law.

Diffraction patterns were analysed using the High Score software, in which they were compared against patterns from the International Centre for Diffraction Data (ICDD). A diffraction pattern is obtained by measuring the intensity of scattered waves as a function of scattering angle (θ). Very strong intensities (Bragg peaks) are obtained in directions for which the scattering angles satisfy the Bragg condition [129].

The scan was performed in the range between 30° and 120° (2θ), with a step size of 0.05° and count time at each step of 0.25 s. The specimen had a diameter of 13.3 mm and thickness of 3 mm. The resultant XRD spectrum is shown in Figure 5.5, where it can be seen that (at ambient temperature) the material is composed solely of the B2 austenitic phase.

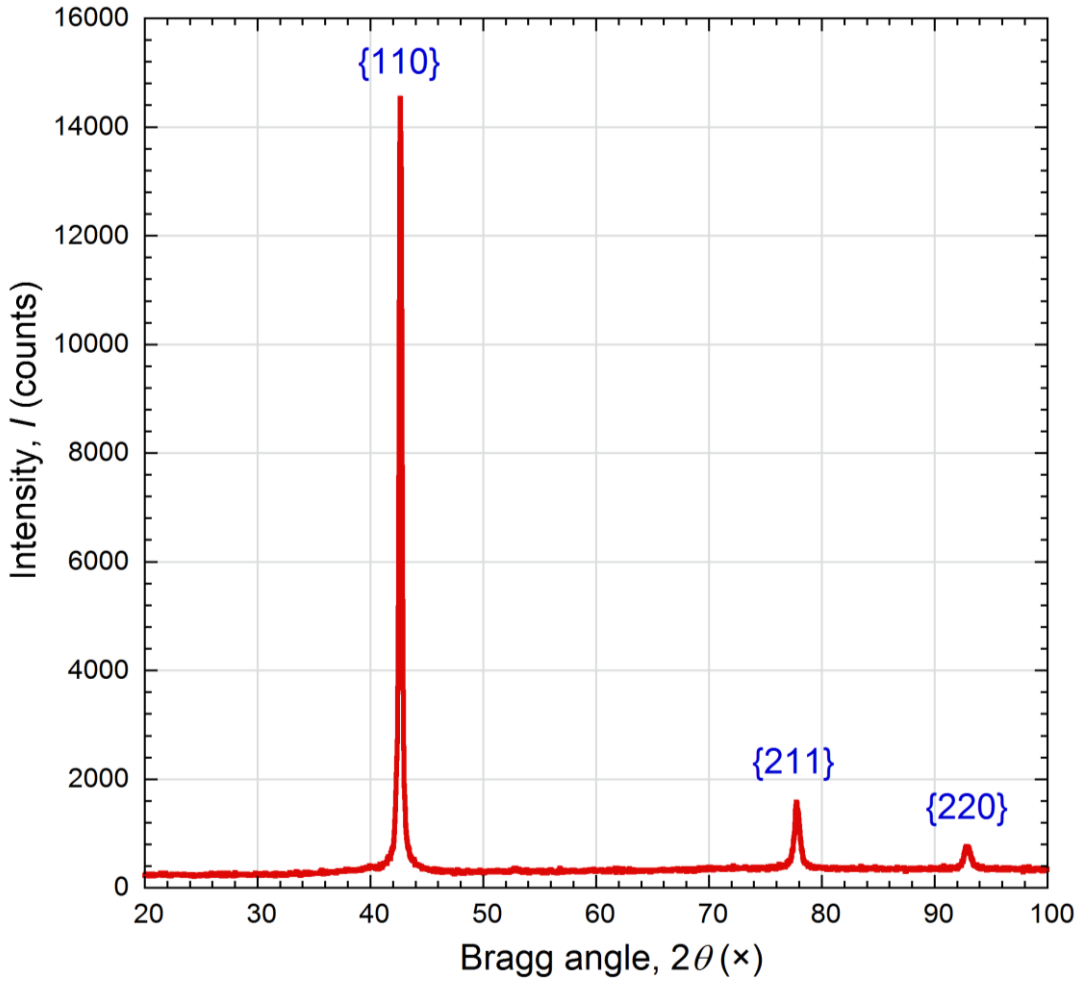

Figure 5.5. XRD spectrum from a NiTi sample, showing peaks from only the austenitic (B2) phase, which is cubic (with a lattice parameter of 0.2998 nm).

The peak list in Table 5.1, was obtained for powder diffraction from the ICDD database [130].

Austenite (B2) *a = b = c = 2.998 Å* $\alpha = \beta = \gamma = 90^{o}$		***Cubic system:*** $d = \frac{a}{\sqrt{h^2 + k^2 + l^2}}$	
2θ (º)	***d (Å)***	***hkl***	***Identified peaks***
29.7	2.99	{100}	no
42.6	2.11	{110}	yes
52.8	1.73	{111}	no
61.8	1.49	{200}	no
70.1	1.34	{210}	no
77.8	1.22	{211}	yes
92.8	1.06	{220}	yes

Table 5.1. Peak list, interplanar spacing and Miller indices for a superelastic NiTi alloy over the range of the experiment.

From this spectrum, the strong {110} peak is a clear indication that the austenitic phase (B2) has developed a more marked texture. This is a strong preferred orientation of austenite with the {110} lattice planes parallel to the surface. It is not unusual since the sample consisted of a disk cut from an extruded rod made of a polycrystalline NiTi alloy, which tends to present texture in the axial (extrusion) direction. The {100}, {111}, {200} and {210} peaks also satisfy Bragg's condition, but their relative intensities detected in this experiment were very low (lower than 1.5%) and, therefore, not visible in the spectrum. This has also been reported in the literature [131, 132] for textured NiTi alloys (especially wires).

5.4. Microscopy

Optical microscopy (OP) was performed using an optical microscope (Leica DM 4000B) in reflected mode, in which the images were captured using a Moticam 1000 digital camera.

The grain structure, which can be seen in the optical micrograph in Figure 5.6, is approximately equiaxed (in transverse section), with a grain size of around 30-70 μm, determined by using the intercept line method. Axial sections exhibited a similar microstructure. The composition was investigated using EDX (Energy-Dispersive X-Ray spectroscopy) in an SEM, which yielded a value of Ni-49.2 at%Ti.

This is approximate as expected, although this is not a highly accurate technique and the averaged error on this figure is as high as ±0.3% from 10 analysed regions.

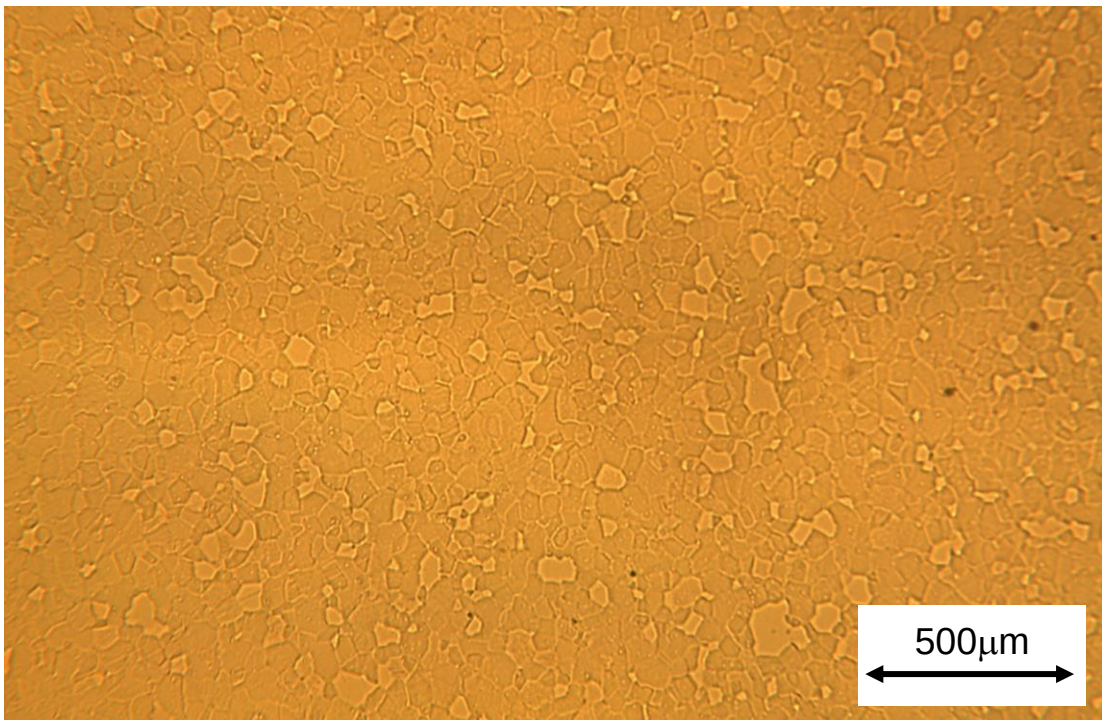

Figure 5.6. Optical micrograph of a transverse section of the NiTi rod.

Thus, the grain size is small in comparison with the indenter diameters used in this work (4 mm and 8 mm). This assures that the indents will interrogate a large number of grains, which is crucial when the objective is to extract bulk properties from indentation testing. In this regard, it is possible to capture the influence of an assembly of grains being deformed, not only of the crystallographic texture of the material but also of the way that cooperative deformation of neighbouring grains takes place.

5.5. Resonant Frequency and Damping Analyser

Low strain measurements of Young's moduli for both phases were carried out using a Resonant Frequency and Damping Analyser (RFDA) (model system 23, version 6.3.0, supplied by IMCE NV). The RFDA is a system designed for impulse excitation measurements. The RFDA basic system measures the resonant frequencies and internal friction or damping and calculates Young's modulus of samples, according to ASTM E1876-15 [133]. The specimen is mechanically tapped by a small flexible hammer with an automatic excitation unit. The induced vibration signal is detected with a USB-microphone and the elastic modulus was inferred by the built-in software.

Tests were performed within a frequency range of 10-16 kHz. The measurements were performed at room temperature (~20˚C) for the austenitic phase. For the martensitic phase, fully achieved only at very low temperatures according to the DSC results (M_f = -78˚C), the sample was dipped into liquid nitrogen (~-190˚C) and quickly tested. In this context, the obtained value for the modulus of austenite (E_A) was 72 GPa ± 1.0 GPa, whereas for the modulus of martensite (E_M) the value was 93 GPa ± 1.0 GPa. These moduli will be used as input parameters in the material formulations in the next chapters.

5.6. Summary

The following topics can be summarised from this experimental chapter:

- The transition temperatures M_s, M_f, A_s and A_f, obtained via DSC, are respectively about -37°C, -78°C, -32°C and -10°C. That confirms that the material should be entirely austenite at room temperature (in the absence of applied stress).

- The austenitic phase has a marked texture, as shown by the {110} peak in the XRD spectrum. The {100}, {111}, {200} and {210} peaks also satisfy Bragg's condition, but their relative intensities were very low (lower than 1.5%) and, therefore, they are not visible in the spectrum. This is not unusual for a polycrystalline material from an extruded rod, such as this one, which tends to present some degree of texture in the axial (extrusion) direction.

- The optical micrograph revealed that the grain structure is approximately equiaxed (radial and axial direction), with a grain size of around 30-70 μm. This result establishes that the grain size is small in comparison with the indenter diameters used in this work (4 mm and 8 mm). This assures that the indents will interrogate a large number of grains, which is crucial for the extraction of bulk properties from indentation testing.

- The chemical composition, investigated via EDX, was Ni-49.2 at%Ti (±0.3%), which was approximately that provided by the manufacturer of the NiTi rods investigated here.

- Young's moduli of both phases were investigated using RFDA. The value obtained for the modulus of austenite was 72 GPa ± 1.0 GPa, whereas for the modulus of martensite the value was 93 GPa ± 1.0 GPa.

6. DEVELOPMENT OF FINITE ELEMENT MODELS

6.1. NiTi in Commercial Codes

Currently, there are finite element solvers, such as ABAQUS, which incorporate built-in routines to predict the superelastic behaviour of NiTi. This user-material subroutine (UMAT - *ABQ_SUPER_ELASTIC*) can be used in either Abaqus/Standard or Abaqus/Explicit [66]. This routine is based on the mathematical and phenomenological descriptions proposed by Auricchio and Taylor [27] (§3.5.1), Auricchio [63] and Auricchio and Sacco [59] (§3.5.2).

The complete set of parameter values to be specified for implementation of the ABAQUS package is shown in Table 6.1. The first seven parameters (identified in Figure 2.7) can be obtained directly from stress-strain curves.

Parameter	Symbol
Young's modulus of Austenite	E_A
Young's modulus of Martensite	E_M
Transformation strain	ε_L
Martensite start stress	σ_{Ms}
Martensite finish stress	σ_{Mf}
Austenite start stress	σ_{As}
Austenite finish stress	σ_{Af}
Poisson's ratio of Austenite	ν_A
Poisson's ratio of Martensite	ν_M
Temperature coefficient of phase transition stress (loading)	C_A
Temperature coefficient of phase transition stress (unloading)	C_M

Table 6.1. NiTi alloy parameter values for use in the ABAQUS model, adapted from ABAQUS User Manual [66].

There are other material formulations capable of capturing, with limitations, the behaviour of such materials (see §3.5.3). However, these are not necessarily available, and sometimes they include "calibration factors", making them difficult to understand. Lagoudas et al. [71] proposed an energy-based formulation, also used in this work,

which requires some more material parameters, as presented in Table 6.2. This is an open-source formulation, and its input parameter values are obtained from uniaxial mechanical testing and DSC as well as some material constants.

Material properties	Symbol
Phase transition parameters (from stress-strain curve)	
Martensite start stress	σ_{Ms}
Transformation strain	ε_L
Austenite start stress	σ_{As}
Temperature coefficient of phase transition stress (loading)	C_A
Temperature coefficient of phase transition stress (unloading)	C_M
Elastic constants	
Modulus of austenite	E_A
Modulus of martensite	E_M
Poisson's ratio of austenite	ν_A
Poisson's ratio of martensite	ν_M
Phase transformation temperatures (DSC)	
Martensite start temperature	M_s
Martensite finish temperature	M_f
Austenite start temperature	A_s
Austenite finish temperature	A_f
Density and thermal properties	
Density	ρ
Coefficient of thermal expansion of austenite	α_A
Coefficient of thermal expansion of martensite	α_M
Specific heat	c
Thermal conductivity	K

Table 6.2. Material parameters for NiTi alloys for use with the energy-based formulation proposed by Lagoudas et al. [71].

6.2. FE Indentation Model

An axisymmetric FEM model for simulating spherical indentation was built in ABAQUS. Both indenter ball and specimen were modelled as illustrated in Figure 6.1. The parts will be modelled as deformable bodies and meshed with first order quadrilateral and triangular elements.

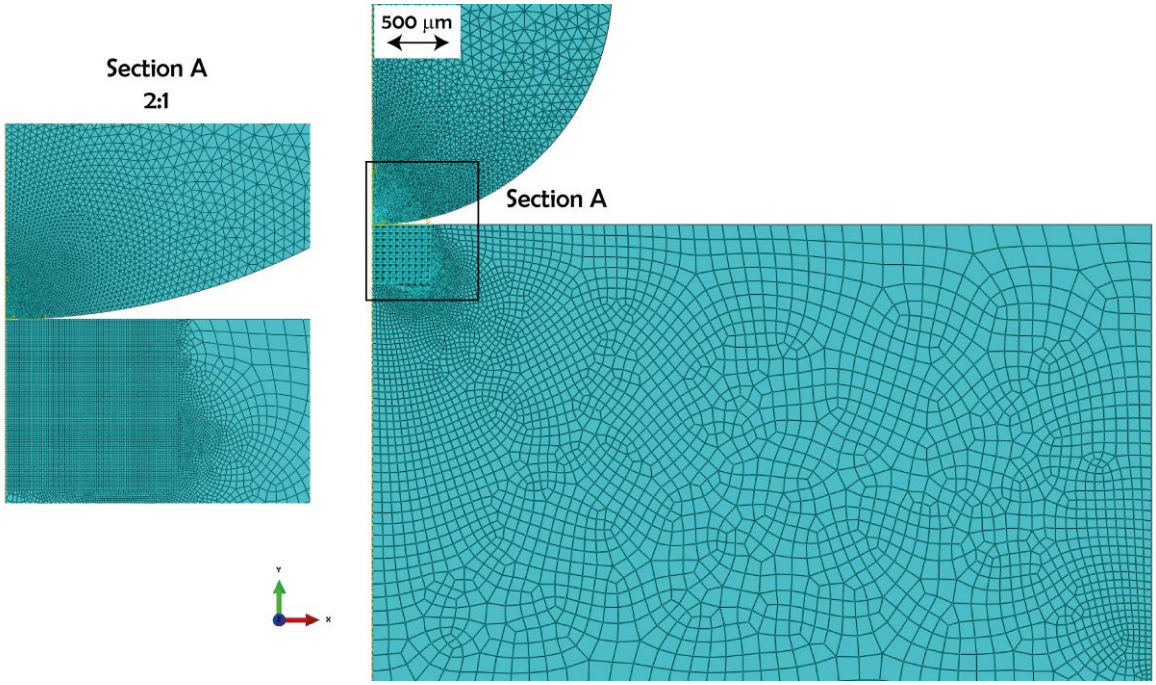

Figure 6.1. FE model of indentation with magnified fine-mesh partition.

The spherical indenter is expected to remain elastic throughout, although it can be important in high precision work of this nature not to treat it as a rigid body: not only is it possible for its elastic deformation to make a significant contribution to the overall displacement, but its lateral Poisson's expansion could affect the outcome, particularly if attention is being focused on the shape of the residual impression, regarding the indenter. The two elastic constants, Young's modulus and Poisson's ratio, used for the WC-Co cermet indenter were 650 GPa and 0.21, respectively. Such modelling also allows a check to be made on whether there is any danger of these parts being plastically deformed.

The spherical indenter had 5637 quadratic triangular elements of type CAX6, and the sample had 16532 linear quadrilateral elements of type CAX4H (coupled temperature-displacement). Meshes were refined in regions of the sample close to the indenter (see Figure 6.1 - Section A).

Sensitivity analyses confirmed that the meshes employed were sufficiently fine to achieve convergence, numerical stability and mesh-independent results. The complete sample was included in the simulation, with its rear surface rigidly fixed in place. When modelling the complete sample, contributions to the displacement caused by its elastic deformation (as well as plastic deformation) are fully captured. Assuming that

conventional plasticity does not take place and that any tensile-compressive asymmetry can be ignored, the user material subroutine for superelastic deformation previously mentioned can be used.

6.3. FE Uniaxial-Compression Model

A three-dimensional FE model for simulating the mechanical behaviour of NiTi was built in ABAQUS, attempting to reproduce the cube subjected to uniaxial compression, as illustrated in Figure 6.2.

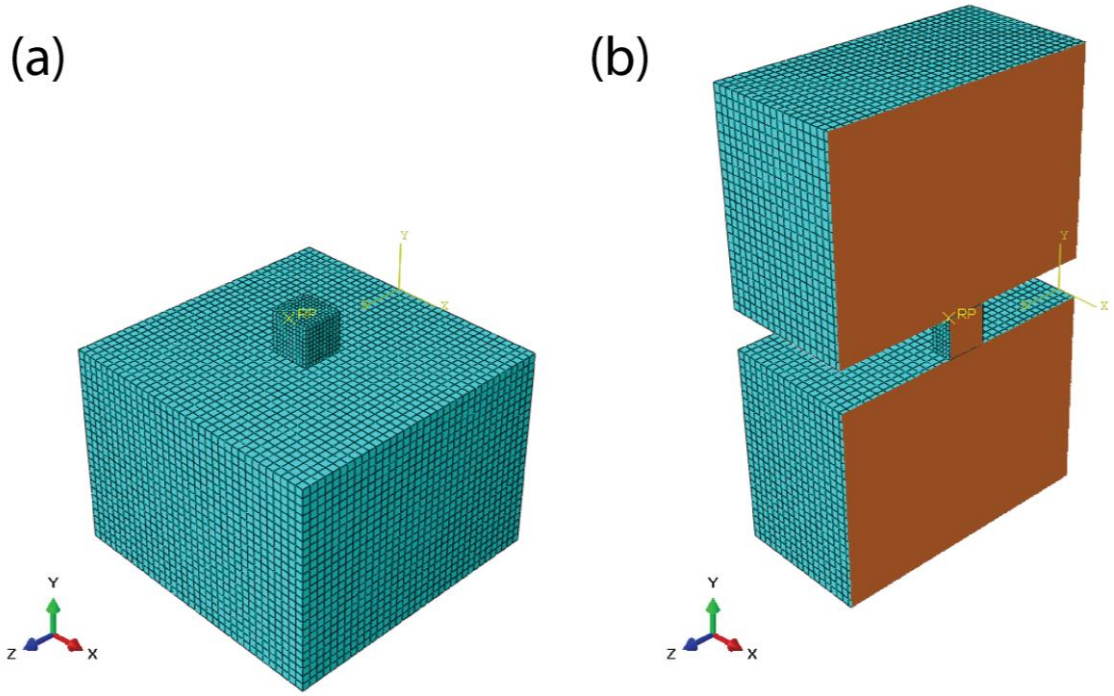

Figure 6.2. FE modelling of NiTi cube undergoing uniaxial compression between steel plates: (a) sample on steel platen (without top platen) and (b) Cut-through view of the specimen between the platens.

The model has taken into account the elasticity of the compression platens (E ~ 195 GPa and ν ~ 0.27) which, in this case, could affect the experimentally measured displacement. The volume elements in the model were linear hexahedra, type C3D8 (8-node linear brick), with 30625 elements in each platen and 1000 elements in the sample (coupled temperature-displacement).

6.4. Summary

This chapter can be summarised as:

- Finite Element Models were built to simulate the behaviour of superelastic NiTi under indentation and uniaxial compression.
- Modelling aspects such as mesh, boundary conditions and element type were defined.
- Experimental input parameters for use with the selected material formulations were identified.

7. ALGORITHM FOR EXTRACTION OF MATERIAL PROPERTIES

7.1. Quantification of the Goodness-of-Fit

The procedure used in the current work to quantify the goodness-of-fit between predicted and target indentation outcomes was least squares regression. This is popular for optimising a set of model parameter values, by quantifying the fit between the modelled values of a scalar variable and corresponding expected values [9-11]. These are the parameter values that minimise the sum of the squares of the residuals, which are the differences between expected and modelled values of the variable.

For the current work, the primary outcome is a load-displacement plot, the variable is the load (as a function of displacement), and the parameters are those in the selected constitutive law for material superelasticity. It would also be possible to include in this set other parameters that influence the indentation process, such as the coefficient of friction, although that has not been done for the results presented here. It may also be noted that other outcomes could be used, either alternatively or additionally. For plasticity, the other outcome that is likely to be used is the residual indent shape (indent depth as a function of radial location), although that has not been done in the current work since there was no residual indent.

More generally, when other material properties are being sought, there are several options concerning the outcomes that might be obtained from experimental load-displacement-time datasets and used as target variables. In recent work, for example, Burley et al. [134] evaluated a strain rate sensitivity parameter from ballistic indentation experiments, using both displacement-time and residual indent shape datasets as outcome variables. Having more than one target variable can complicate the convergence procedure, although, in that particular case (with just a single material property parameter to evaluate), simple linear scans in parameter space allowed rapid identification of optimal values.

The sum of the squares of the residuals, S, can be expressed:

$$S = \sum_{i=1}^{N} \left(\delta_{i,\mathrm{M}} - \delta_{i,\mathrm{E}} \right)^2 \tag{7.1}$$

where $\delta_{i,\mathrm{M}}$ is the *i*th value of the modelled displacement (predicted by FEM) and $\delta_{i,\mathrm{E}}$ is the corresponding experimental (target) value. The value employed for *N* was around 100. The perfect fit will lead to a value of zero for *S*. Since *S* is dimensional, it has units, so that its magnitude cannot be used to give a universal indication of the quality of the fit. For this purpose, the quantity S_{red}, a "reduced sum of squares" is used:

$$S_{\mathrm{red}} = \frac{\sum_{i=1}^{N} \left(\delta_{i,\mathrm{M}} - \delta_{i,\mathrm{E}} \right)^2}{N \ \delta_{\mathrm{av,E}}^2} \tag{7.2}$$

where $\delta_{\mathrm{av,E}}$ is the average of the experimentally-measured displacements (across the range of loads being used) and *N* is the total number of displacement increments. The parameter S_{red} is a positive number, with a value that ranges upwards from 0 (corresponding to a perfect fit).

A value of S_{red} below about 10^{-3} represents a degree of fit that might generally be regarded as "good". It has been found [11] during the extraction of plasticity parameters that such values indicate that the material response is being captured well by the analytical equation concerned. However, it should be recognized that there are some differences with superelasticity. An important point is that the penetration ratio (δ/R) must be kept low (<0.7%) in order to avoid stimulating irrecoverable strains (i.e. creating peak strains above about 4%). This does generate a considerable potential for "compensation", i.e. for various sets of input parameter values to give effectively the same (load-displacement) outcome. This is exacerbated by the fact that several (at least about 5) independent parameter values are required to characterise the superelastic stress-strain behaviour, whereas 3 variables are required to characterise plasticity.

Furthermore, a valuable capability for plasticity is to use the residual indent profile as an additional, or alternative, outcome on which to target the modelling. This is not an option for superelasticity, which leaves no residual indent. The upshot of these effects is that a value of S_{red} corresponding to "good" fit does not necessarily

correspond to a reliable set of parameter values. Also, convergence is likely to be slow − much slower than for plasticity, which is often completed in fewer than 100 iterations.

7.2. Iterative Convergence on Best-Fit Parameter Values

7.2.1. Convergence Method

Modelling the indentation testing using best-fit set of parameter values obtained from uniaxial testing is a relatively simple operation, and hence to obtain a predicted outcome − focused here on the load-displacement relationship, although the model can also be used to monitor other outcomes (such as the evolving stress and strain fields and progression of the phase transformation). However, simply checking the consistency, in this way, is not the main objective of the current exercise, which is to explore the inverse operation of starting with the load-displacement plot and inferring from this the stress-strain relationship − i.e. the values of the SE parameters that define this relationship within the ABAQUS formulation. This has been done in the current work by using the well-known convergence algorithm of Nelder-Mead [121], which is based on a study of how the sought parameters behave in the multi-coordinate space of the parameters to be evaluated (the SE parameters of the material concerned).

For a model with m parameters, the search is performed within an m-dimensional parameter space, within which a *simplex* is defined. This is a *polytope* with (m+1) vertices (i.e. a triangle in 2D, as the example illustrated in Figure 7.1, a tetrahedron in 3D etc). Each vertex corresponds to a particular combination of all of the m parameters in the set, and the simplex covers a range of values for all of these. These points can be expressed as vectors (first rank tensors) in parameter space, designated $\boldsymbol{x}_1$, $\boldsymbol{x}_2$,…$\boldsymbol{x}_{m+1}$, each of which consists of a set of m parameter values. After each iteration (new set of FEM simulations), the objective is to “improve” the simplex by replacing the worst vertex (i.e. the one with the highest value of S) with a better point. The search for this better point is along a line in parameter space defined by the worst point and the centroid of the rest of the simplex, which is the average position of the remaining points (after removal of the worst point). A new simplex is then created, and the process is repeated until the gradient is approximately zero (e.g. it reaches the established tolerance).

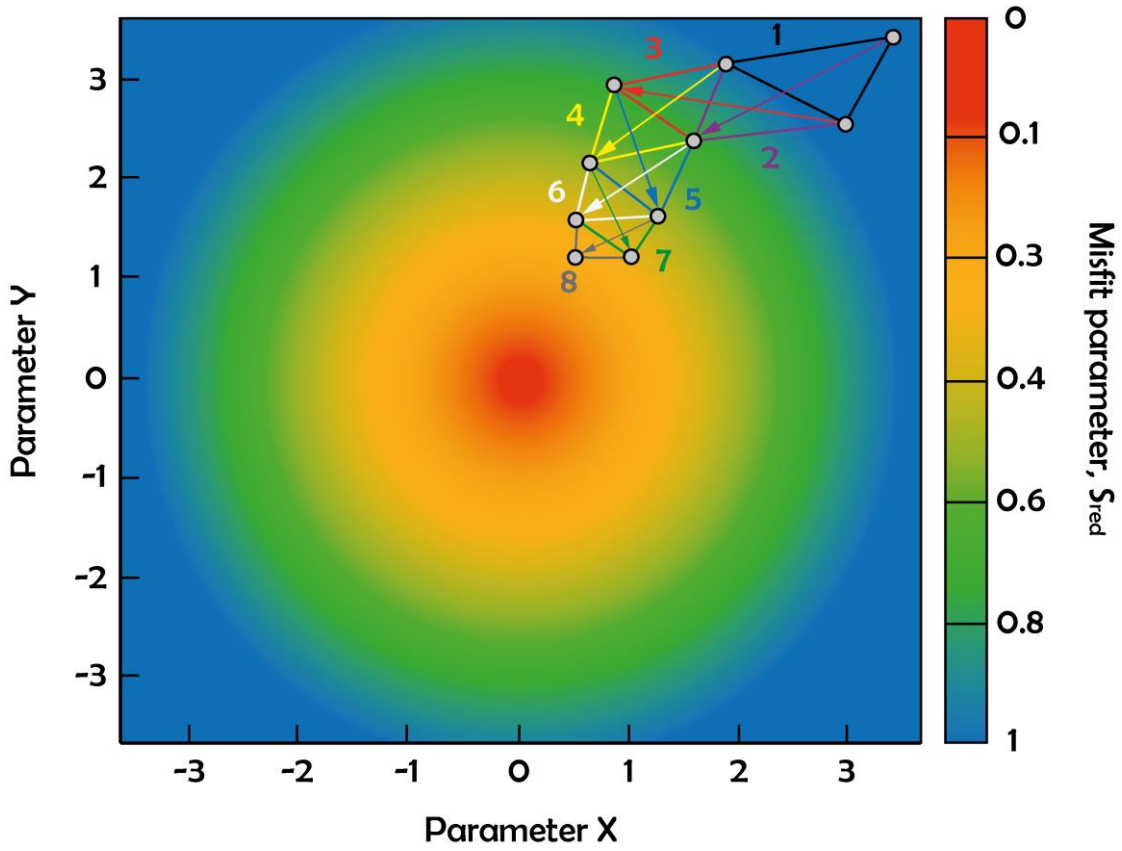

Figure 7.1. A schematic example of the “downhill” Nelder-Mead algorithm in two-dimensions, with an idealised $S_{red} = 0$.

It is worth noting that the step size at each stage reduces in size as the algorithm moves forward [135, 136]. The Nelder-Mead simplex can change in five different ways during an iteration, as illustrated in 2D in Figure 7.2. Except in the case of shrink, the worst vertex of the simplex at iteration k (point x_3) is replaced at iteration $k + 1$ by one of the reflection, expansion, or contraction points.

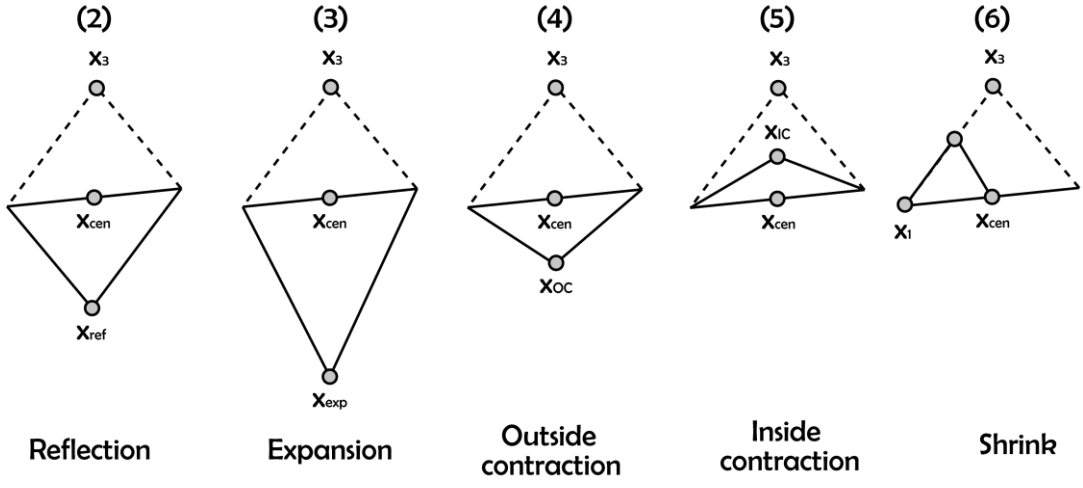

Figure 7.2. Nelder-Mead simplices after reflexion, expansion, outside contraction, inside contraction, and shrink. The original simplex is shown with a dashed line.

Once an initial simplex has been created, each iteration comprises the following steps:

I. The values of S are calculated for each vertex and the vertices are ranked, such that $S(\boldsymbol{x}_1) < S(\boldsymbol{x}_2) < \ldots < S(\boldsymbol{x}_{m+1})$. The point to be replaced is $\boldsymbol{x}_{m+1}$. The centroid of the (reduced) simplex is calculated from:

$$\boldsymbol{x}_{cen} = \frac{1}{m}\sum_{j=1}^{m}\boldsymbol{x}_j \tag{7.3}$$

This defines the search direction ($\boldsymbol{x}_{\text{cen}} - \boldsymbol{x}_{m+1}$).

II. Reflection: A trial point is established by reflection of $\boldsymbol{x}_{m+1}$ through $\boldsymbol{x}_{\text{cen}}$.

$$\boldsymbol{x}_{\text{ref}} = \boldsymbol{x}_{\text{cen}} + a\left(\boldsymbol{x}_{\text{cen}} - \boldsymbol{x}_{m+1}\right) \tag{7.4}$$

where α is a scale factor. The value of S is calculated for this point. If $S(\boldsymbol{x}_1) < S(\boldsymbol{x}_{\text{ref}}) < S(\boldsymbol{x}_m)$, so that $\boldsymbol{x}_{\text{ref}}$ is of intermediate quality, then $\boldsymbol{x}_{\text{ref}}$ is accepted, replacing $\boldsymbol{x}_{m+1}$. Otherwise, the algorithm proceeds to step 3.

III. Expansion: If $S(\boldsymbol{x}_{\text{ref}}) < S(\boldsymbol{x}_1)$, so that $\boldsymbol{x}_{\text{ref}}$ is the best point yet, this could indicate that the simplex is on an extended downward gradient and an expanded point is trialed

$$\boldsymbol{x}_{\text{exp}} = \boldsymbol{x}_{\text{cen}} + b\left(\boldsymbol{x}_{\text{cen}} - \boldsymbol{x}_{m+1}\right) \tag{7.5}$$

where β is a scale factor ($>\alpha$). The value of S is calculated for this point. If $S(\boldsymbol{x}_{\text{exp}}) < S(\boldsymbol{x}_{\text{ref}})$, then $\boldsymbol{x}_{\text{exp}}$ is accepted, replacing $\boldsymbol{x}_{m+1}$. Otherwise, $\boldsymbol{x}_{\text{ref}}$ is accepted, replacing $\boldsymbol{x}_{m+1}$.

IV. Outside contraction: If $S(\boldsymbol{x}_m) \leq S(\boldsymbol{x}_{\text{ref}}) < S(\boldsymbol{x}_{m+1})$, so that $\boldsymbol{x}_{\text{ref}}$ is an improvement on $\boldsymbol{x}_{m+1}$, but would become the new worst point, the value of S is calculated for a point between $\boldsymbol{x}_{\text{ref}}$ and $\boldsymbol{x}_{\text{cen}}$, called the outside contraction point.

$$\boldsymbol{x}_{\text{OC}} = \boldsymbol{x}_{\text{cen}} + g\left(\boldsymbol{x}_{\text{cen}} - \boldsymbol{x}_{m+1}\right) \tag{7.6}$$

where γ is a scale factor ($<\alpha$). The value of S is calculated for this point. If $S(\boldsymbol{x}_{OC}) \leq S(\boldsymbol{x}_{ref})$, then $\boldsymbol{x}_{OC}$ is accepted, replacing $\boldsymbol{x}_{m+1}$. Otherwise, the algorithm proceeds to step 6.

V. Inside contraction: If $S(\boldsymbol{x}_{m+1}) \leq S(\boldsymbol{x}_{ref})$, so that $\boldsymbol{x}_{ref}$ is worse than all of the points in the existing simplex, then the value of S is calculated for a point between $\boldsymbol{x}_{cen}$ and $\boldsymbol{x}_{m+1}$, called the inside contraction point.

$$\boldsymbol{x}_{IC} = \boldsymbol{x}_{cen} - \delta\left(\boldsymbol{x}_{cen} - \boldsymbol{x}_{m+1}\right) \tag{7.7}$$

where δ is another scale factor. The value of S is calculated for this point. If $S(\boldsymbol{x}_{IC}) < S(\boldsymbol{x}_{ref})$, then $\boldsymbol{x}_{IC}$ is accepted, replacing $\boldsymbol{x}_{m+1}$. Otherwise, the algorithm proceeds to step 6.

VI. Shrink: If none of the previous steps are able to improve the simplex, then it is shrunk towards the best vertex. This operation is defined by:

$$\boldsymbol{x}'_j = \boldsymbol{x}_j + \delta\left(\boldsymbol{x}_1 - \boldsymbol{x}_j\right) \tag{7.8}$$

for $2 \leq j$ (m+1). The algorithm then starts the next iteration at step 1.

The scale factors (α, β, γ and δ) are often ascribed values of 1, 2, 0.5 and 0.5 respectively, but these can be tuned to cope with particular situations, such as different levels of noise. The Scientific Python implementation allows for these scale factors to be adapted as the algorithm proceeds, as described in Gao and Han [120].

7.2.2. Code for Extraction of Optimised Material Parameters

The algorithm for extraction of superelastic parameter values was developed in Python. The code with the search algorithm in ".py" format is available in Appendix §12.2. The flowchart in Figure 7.3 shows the working sequence of the proposed algorithm. It is necessary to establish initial guesses for each parameter. The model is then run for this particular parameter combination, generating a modelled load-displacement curve, which is compared with an experimental one, yielding a value of S. If the sum of squares is within the specified tolerance, then the process is

terminated. If not, then the algorithm carries on the process repeatedly until the tolerance is reached.

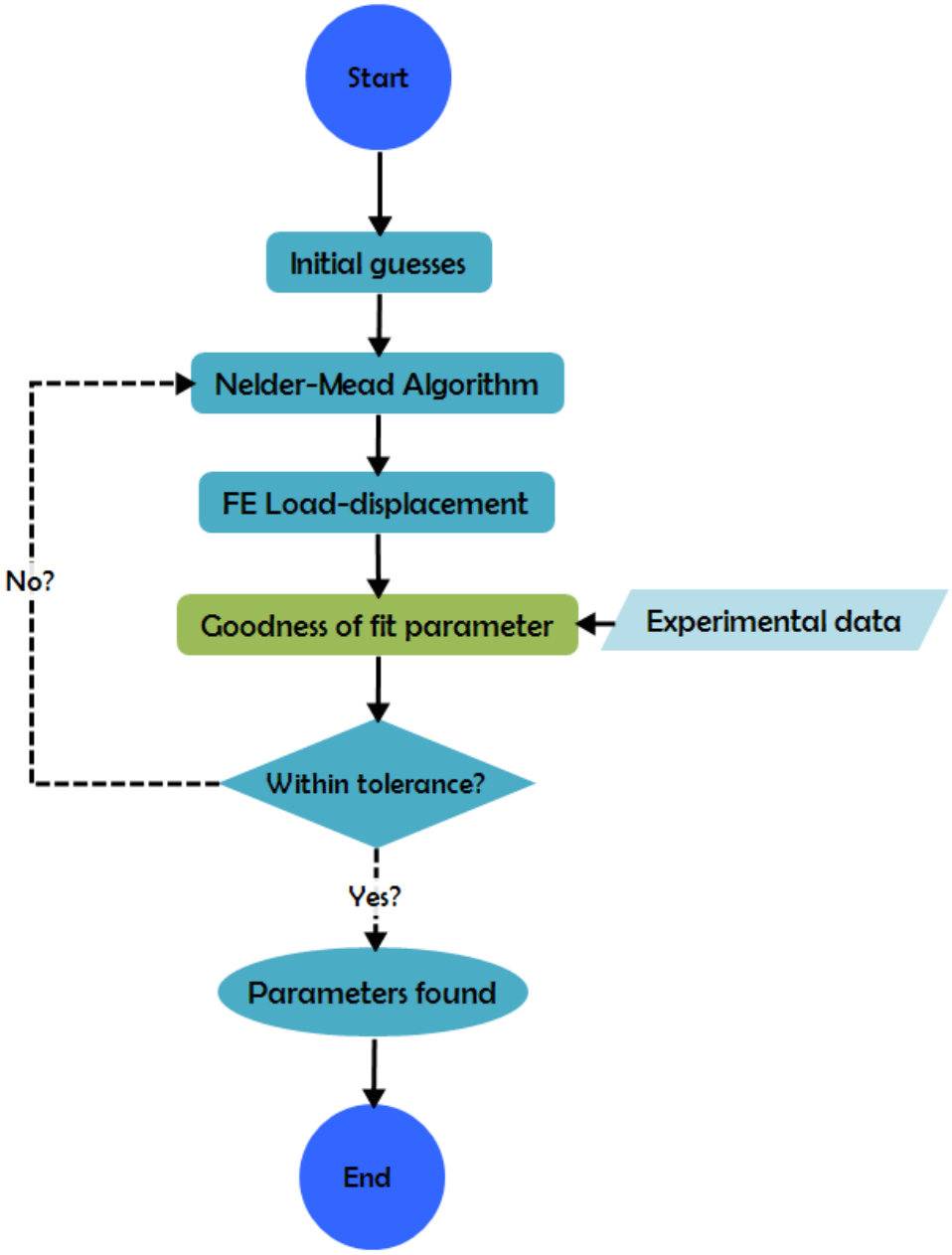

Figure 7.3. Flowchart of the convergence algorithm for parameter search.

Regarding the sought parameters, firstly, the values of the elastic properties of the indentation rig were taken to be invariant and excluded from this algorithm. This was also done with the Poisson's ratio of the phase (ν) and the temperature coefficients of phase transition stress (C). These parameters have a relatively small effect on the overall behaviour (discussed in more detail in §10.1). The Young's moduli of the two phases in the NiTi alloy were taken from the mechanical testing since the experimental

measurement of these two (in the uniaxial test) should be reasonably reliable. If only indentation data were available (which is the target scenario for this methodology), then these would not necessarily be available, so they might have to be included in the convergence algorithm. However, in practice it is likely that they might be at least reasonably well-established, so the procedure described here might be appropriate. This leaves a set of 5 parameter values to be optimised in terms of fit between measured and modelled indentation load-displacement curves, when using the formulation proposed by Auricchio and Taylor [27]. Obtaining convergence in a 5-parameter space might be expected to be a relatively slow operation, possibly requiring a large number of iterations of the FE modelling operation. However, it is clear that, in this case, some of the parameter values will predominantly affect the loading curve, while others will mainly influence the unloading curve.

The algorithm is terminated once a specified convergence criterion has been met. This can be defined as a relative difference (commonly 10^{-4}) in S and/or $\boldsymbol{x}$ between successive iterations. In the present work, this requirement was applied to both S and $\boldsymbol{x}$. The number of iterations to achieve convergence depends on a number of factors, in addition to this criterion specification. These mostly relate to the way that the goodness of fit varies in parameter space, which in turn depends on several issues (including how well the stress-strain curve can be captured by the selected constitutive law). There may in some cases be a danger of converging on a local minimum.

Difficulties can also arise from the presence of “plateau regions”, where various parameter value combinations give very similar degrees of fit. In general, however, it has been found that the algorithm employed performs reasonably well in this context.

Overall, the computational operation is tractable in most cases. The procedure could, however, be facilitated if the starting values for the simplex are in an appropriate region of parameter space (i.e. if the initial trial values are reasonably close to the best solution set). Otherwise, the number of iterations for convergence may go up significantly.

7.3. Summary

The main findings of this chapter can be summarised as:

- The quantification of the goodness-of-fitness, in this work, will be made by the sum of the squares of the residuals between modelled (predicted by FEM) and corresponding experimental (target) load-displacement curves. For a universal indication, this quantity was normalised and converted into the “reduced sum of squares”.

- The well-known convergence algorithm of Nelder-Mead, which is based on a study of how the sought parameters behave in a multi-coordinate space of the parameters, will be used in this work with the SE parameters of the material concerned. This algorithm has been successful with plasticity, where the optimal combination was searched in a 3D parameter space.

- An algorithm for extraction of superelastic parameter values was developed in Python. The moduli of both phases were not included in this search procedure for simplification purposes (as well as other material constants). This leaves a set of 5 parameter values to be optimised in terms of fit between measured and modelled indentation load-displacement curves, when using the selected material formulation. The “reduced sum of squares” below about 10^{-3} represents a degree of fit that might generally be regarded as “good” for the convergence of this algorithm. It has been found, during the extraction of plasticity parameters, that such values indicate that the material response is being captured well by the analytical equation concerned. A different response, in terms of degree of fit, might be found when applying this procedure to superelastic parameter values.

8. UNIAXIAL COMPRESSION TESTING

8.1. Set-up for Uniaxial Compression Testing

In order to obtain the “correct” (quasi-static) superelastic parameter values for this material, samples were subjected to uniaxial compression testing between rigid (hardened steel) platens. Testing was carried out under displacement control at a rate of 1 mm min^{-1}, using an Instron 5562 screw-driven testing machine, with a load cell having a capacity of 30 kN. The strain rate generated during these tests was thus about 4 10^{-3} s^{-1}. A schematic illustration of the set-up for uniaxial compression is shown in Figure 8.1.

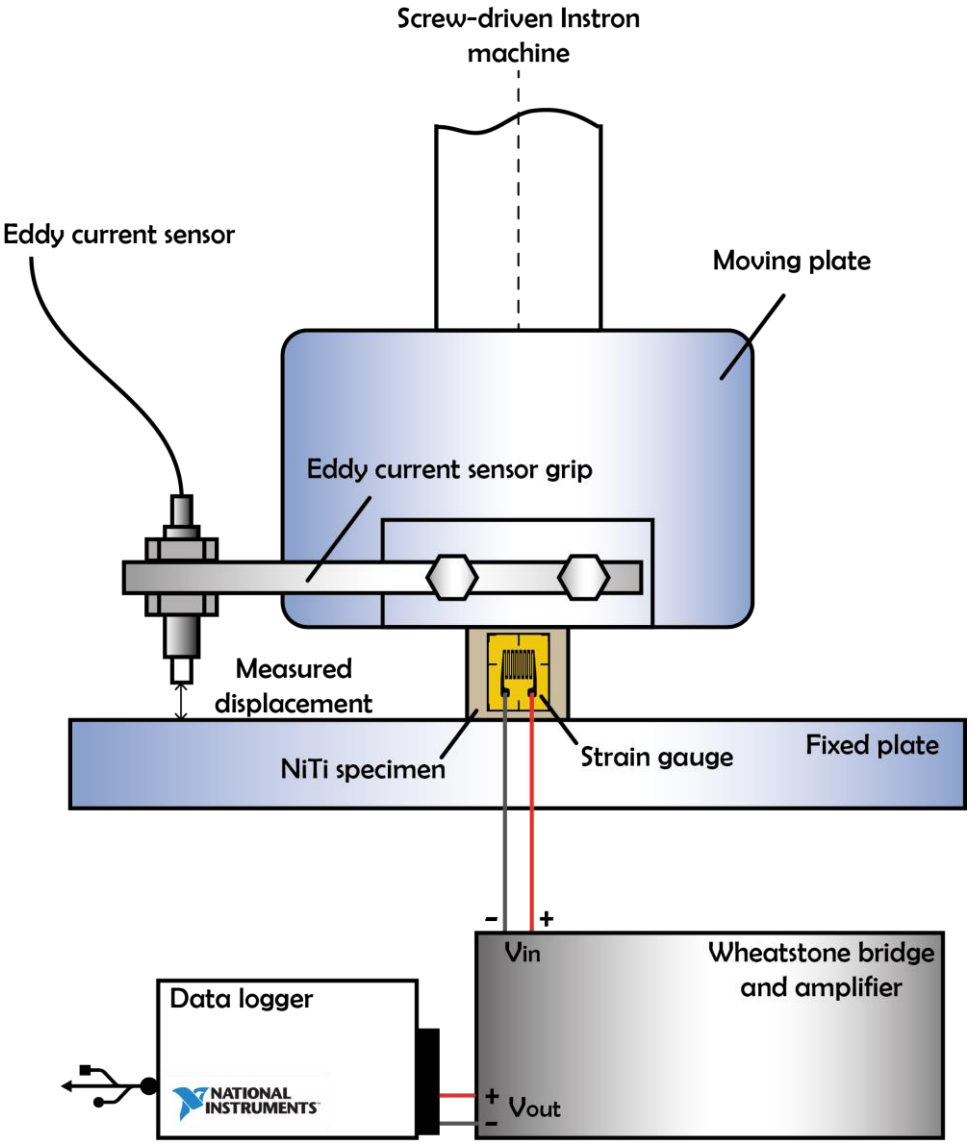

Figure 8.1. A schematic illustration of the mechanical testing set-up for compression testing.

This set-up was designed to allow strains to be simultaneously measured using two techniques. Firstly, pre-wired strain gauges with a resolution of about ±0.1 μm (linear 0.3 mm grid, 120 Ω, two leads and a gauge factor of 1.51, supplied by Omega Engineering Ltd) were stuck onto the samples, using epoxy adhesive. The limitation of this technique is its low strain range, around 2.5% (uniaxial compression), which is not enough to capture the full superelastic loop (~4%) and higher strain levels. Secondly, an eddy current gauge (supplied by Micro-Epsilon Ltd) was attached to the upper platen and actuated against the lower platen. This had a resolution of about ±0.25 μm. Only the eddy current gauge could be used for the complete stress-strain loop, but these readings needed to be corrected for the compliance of the loading train over which the gauge was measuring. While this compliance was small, the correction was necessary, since the sample was also quite stiff, and the measurements were being made over relatively small displacement ranges. Some issues that might induce errors when measuring strains by “indirect” methods are the deformation of the compression platens (despite being only a few microns, it may cause noticeable errors), and the loaded faces not being perfectly parallel or normal to the loading axis.

Tests were performed up to displacements of about 0.2 mm (~4-5%) so that each test took about 12 s to complete. Several repeat tests were carried out. Both stress and strain levels were converted from nominal to true values, using the standard expressions:

$$\sigma_T = \sigma_N(1+\varepsilon_N) \tag{8.1}$$

$$\varepsilon_T = \ln(1+\varepsilon_N) \tag{8.2}$$

with the strains, in this case, being negative (compressive), so that the true stress has a magnitude lower than the nominal value, while the true strain has a larger magnitude than the nominal strain. This is based on deformation taking place at constant volume. In fact, both conventional elastic deformation and superelastic deformation (occurring via the phase transformation) do involve a volume change, the former being (1-2ν) times the axial compressive strain and the latter being about -0.4% in this case. These are both very small, so the assumption of constant volume should be acceptable for these purposes.

Cuboid samples (5 mm × 5 mm × 5 mm) were tested at room temperature (20°C ± 2°C), using MoS_2 lubricant to minimise barrelling. These were cut with one surface normal to the extrusion axis, and testing was carried out both along and transverse to this direction. Extruded rods commonly exhibit strong crystallographic texture and so are often significantly anisotropic in various mechanical properties: this can be significant even in materials, such as this one, that do not exhibit pronounced grain shape anisotropy.

8.2. Compliance of the System

It is essential to establish a correct location for the displacement transducer in order to precisely monitor the strains from the specimen. Moreover, depending on where the transducer is attached, the measured strains could easily be misinterpreted. In this regard, it is essential to use a second measurement system to crosscheck the results. Stress-strain plots with strain outcomes of two different measurement systems: strain gauge and eddy current displacement transducer. This is presented in Figure 8.2.

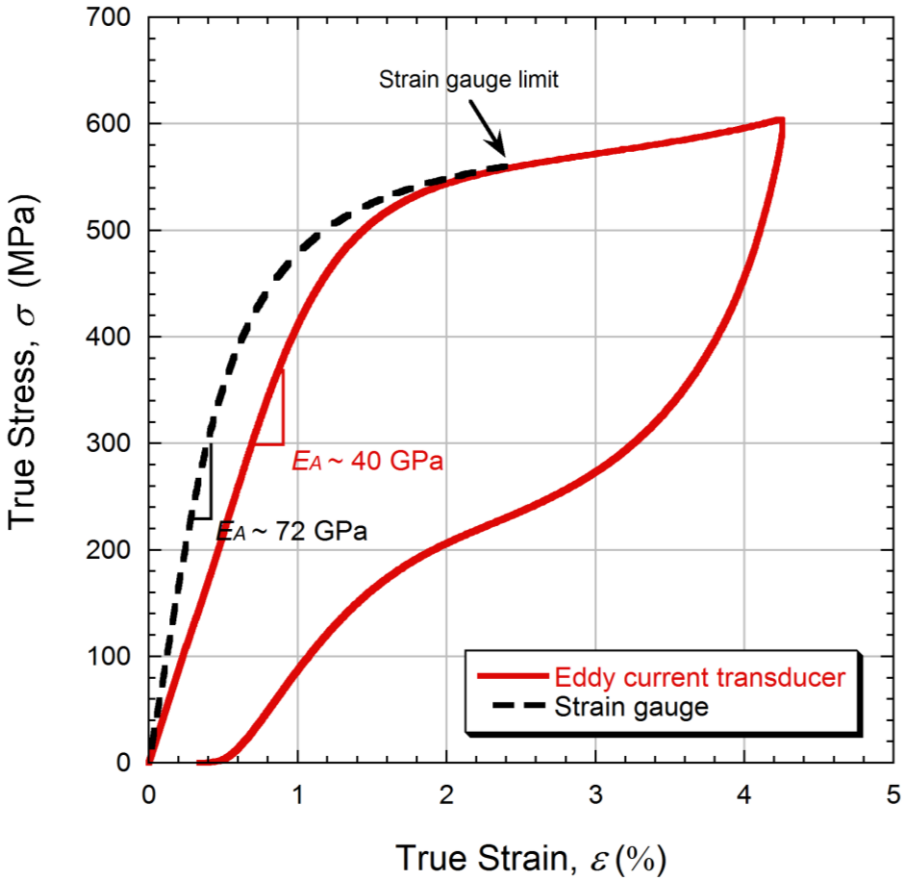

Figure 8.2. Stress-strain plot of a NiTi cube undergoing uniaxial compression (in the axial direction) using two different measurement systems: eddy current transducer and strain gauge.

It is clear that the compliance of the platens affects the data from the displacement transducer. The platens tend to deform around the specimen, which causes the initial gradient (lower than 1% strain) of the stress-strain curve (modulus of austenite, E_A) to be much lower than expected. This certainly affects the entire curve, and the measured strains will appear to be higher than their "correct" values. This is fully discussed in the FE modelling section (§8.7). The outcomes of the strain gauges, however, are not affected by the elasticity of the platens, given that these sensors are attached directly to the specimens, as illustrated in the set-up in Figure 8.1. The limitation of this method is its low strain range (up to ~2.5% in the axial direction). The correlation between strains measured simultaneously via eddy current sensor and strain gauges is shown in Figure 8.3.

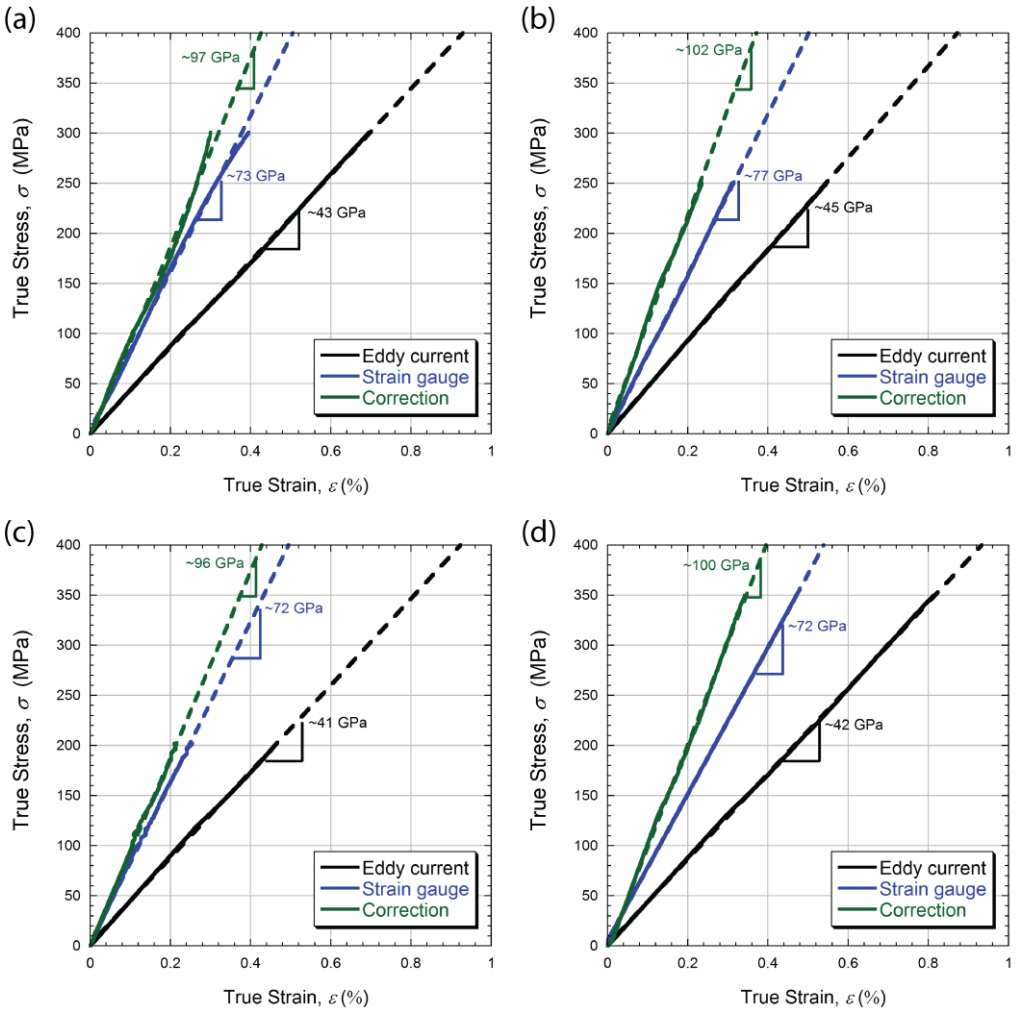

Figure 8.3. Correlation between strains measured simultaneously via eddy current sensor and strain gauges for four specimens: (a) axial specimen axial 1, (b) radial specimen 1, (c) axial specimen 2 and (d) radial specimen 2.

Ideally, the strains obtained from the strain gauges would, solely, be sufficient. However, the strain levels analysed in this current work are higher than the upper limit of the strain gauge (~2.5%). In this regard, a compliance correction procedure must be established. This is a common procedure in axial mechanical testing, but it is of greater importance in the present context as well as for conventional testing of most metals. The strains measured off the eddy current sensor were corrected with the strains measured off the strain gauge, at the same stress interval. This generated the correction curve (in green), and its gradient was used to correct the stress-strain plots obtained via eddy current transducer. The averaged "correction gradient" obtained from this procedure was 1 GPa ± 0.040 GPa. This implied a compliance value of ~2.1 μm kN^{-1}. The comparison between the corrected stress-strain curve and the ones obtained directly from strain gauge and eddy current measurements is presented in Figure 8.4. More corrected stress-strain plots are shown in Appendix §12.3.

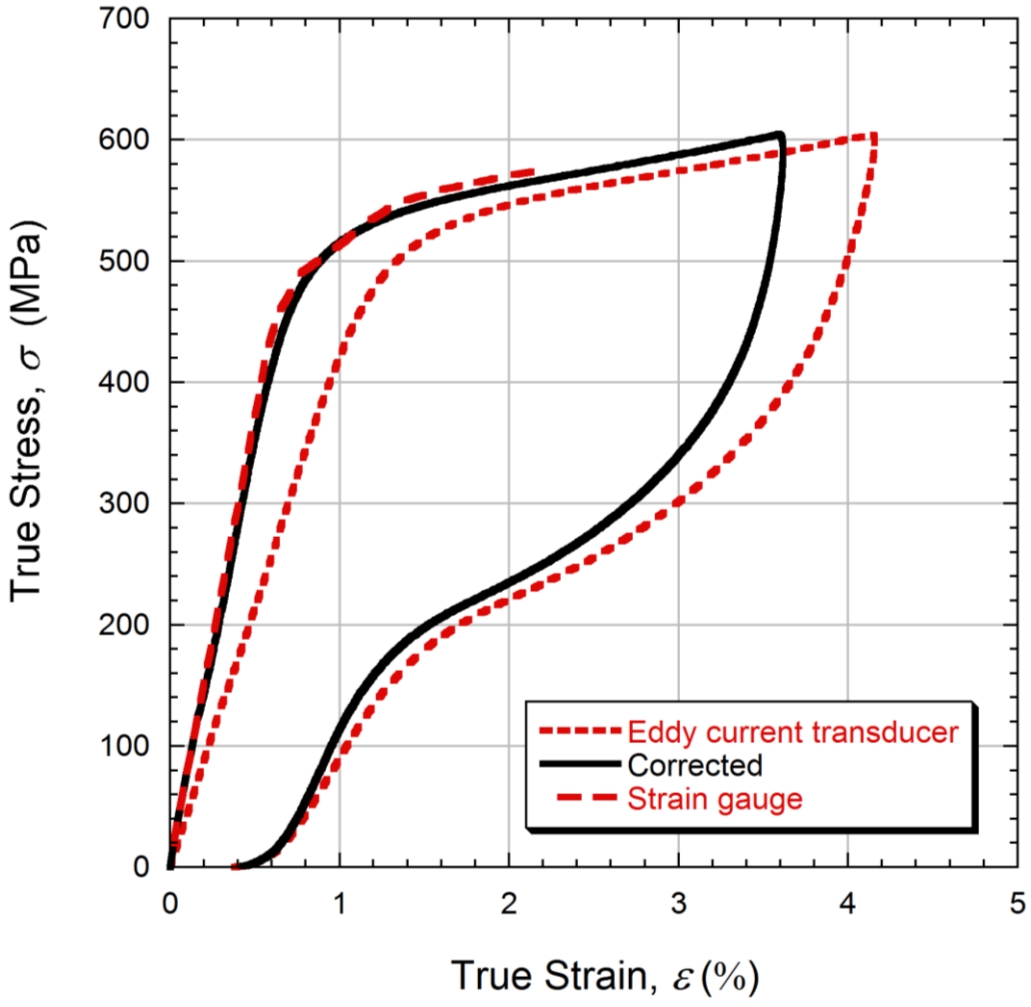

Figure 8.4. Comparison between a corrected stress-strain curve and the ones obtained simultaneously via strain gauge and eddy current sensor.

After the compliance correction, the value of E_A obtained via mechanical testing is similar to the one obtained via RFDA (§5.5) which was 72 GPa ± 1.0 GPa at room temperature (~20˚C). This result highlights the importance of having at least two independent measurement systems.

8.3. Superelastic Limit: Major and Minor Loops

The strain range of interest in the present work is that in which deformation occurs via superelasticity. The literature [4, 30, 34, 36, 37] reports a strain range of up to 10%, but for this material the limit is lower. It is possible to determine the superelastic limit experimentally from the stress-strain plot. It is defined as the point at which the material is fully transformed into martensite. The phase transition is completed at the end of the plateau (where the martensite fraction is equal to 1) during the forward transformation, as illustrated in Figure 8.5. It can be seen that the superelastic limit is below 4%.

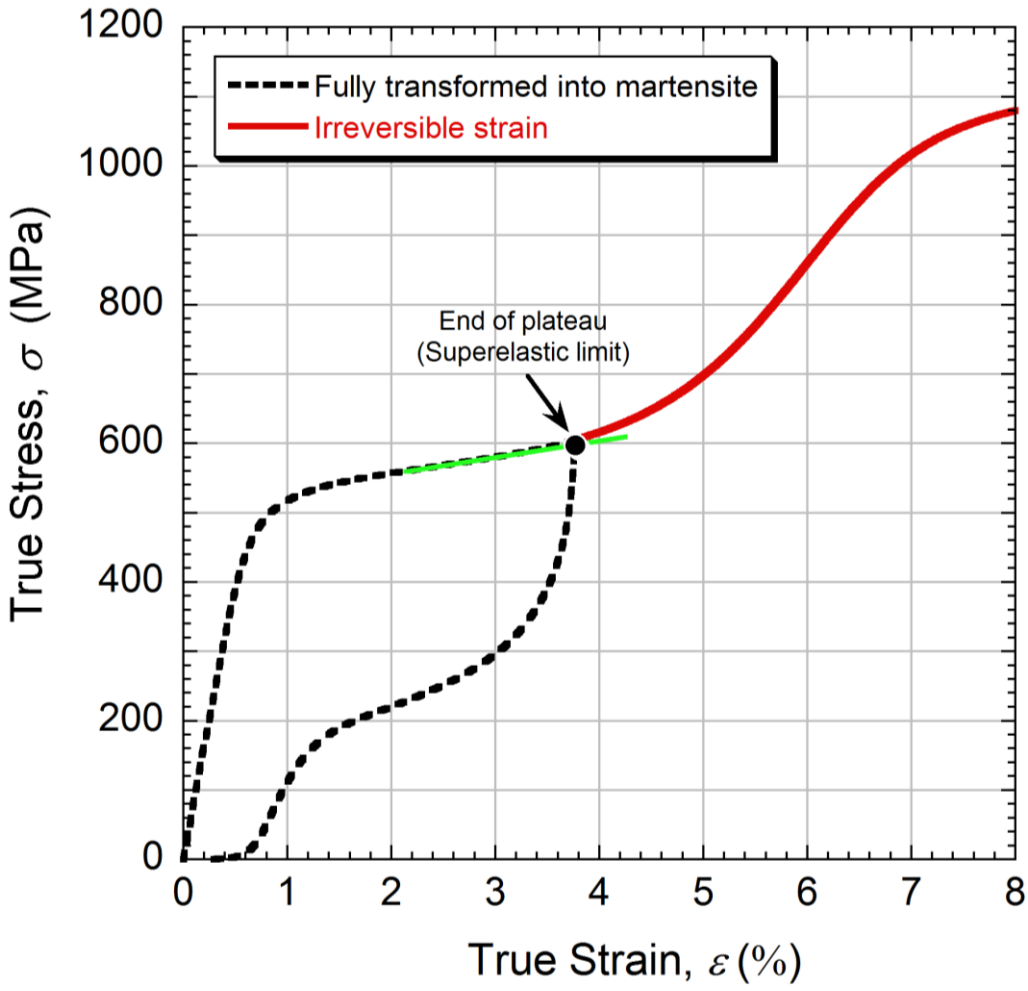

Figure 8.5. Stress-strain plot (in the axial direction) highlighting the definition of the superelastic limit.

The dashed loop is known in the literature [53] as the major (stress-strain) superelastic loop. It is possible to have minor superelastic loops, within the major one, when unloading starts when the material is not fully transformed into martensite, e.g. with the fraction of martensite greater than 0 and less than 1. Seven minor loops (specimens 1-7) are shown in Figure 8.6, each obtained from uniaxial compression in the axial direction of seven different NiTi cubes to avoid mechanical cycling effects [53].

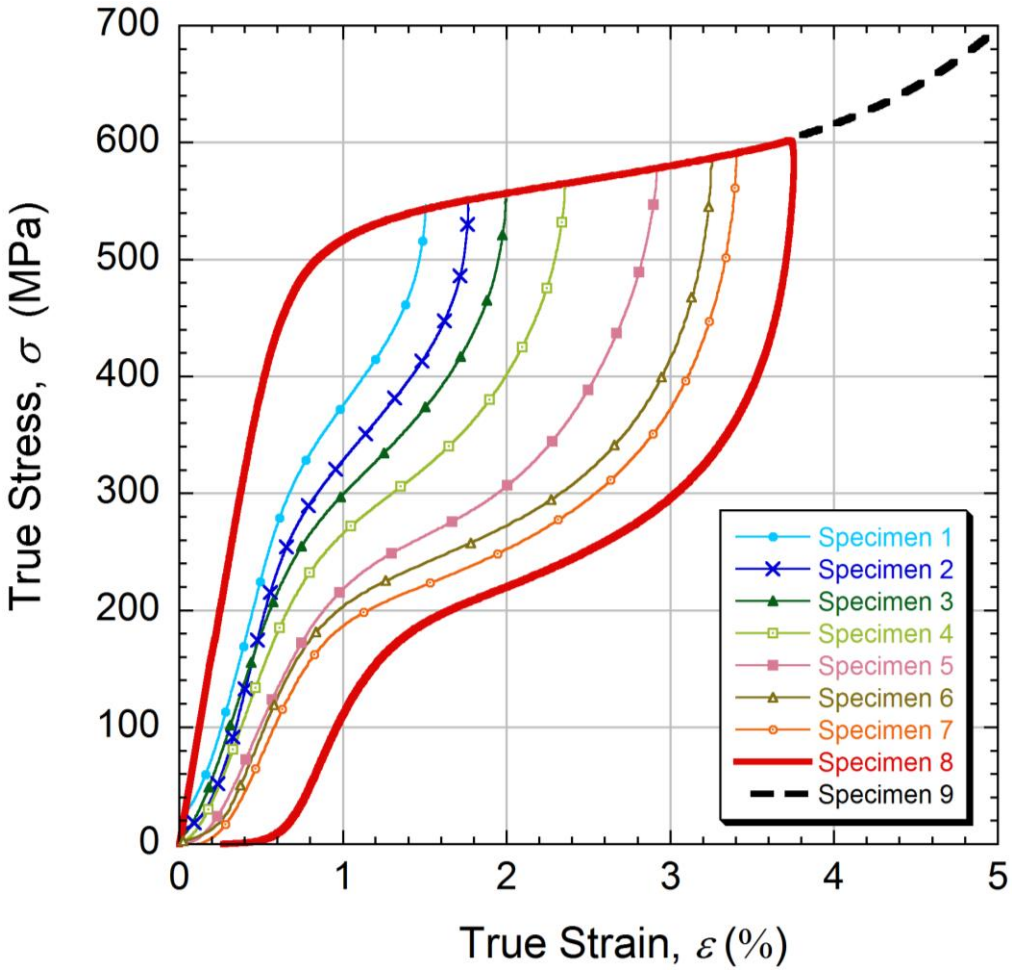

Figure 8.6. Seven minor loops (1-7) obtained from uniaxial compression (in the axial direction) of seven different NiTi cubes.

8.4. Anisotropy Investigation

Anisotropy has been investigated via mechanical testing in the axial and radial directions. Representative plots for compression testing of NiTi in both directions are shown in Figure 8.7.

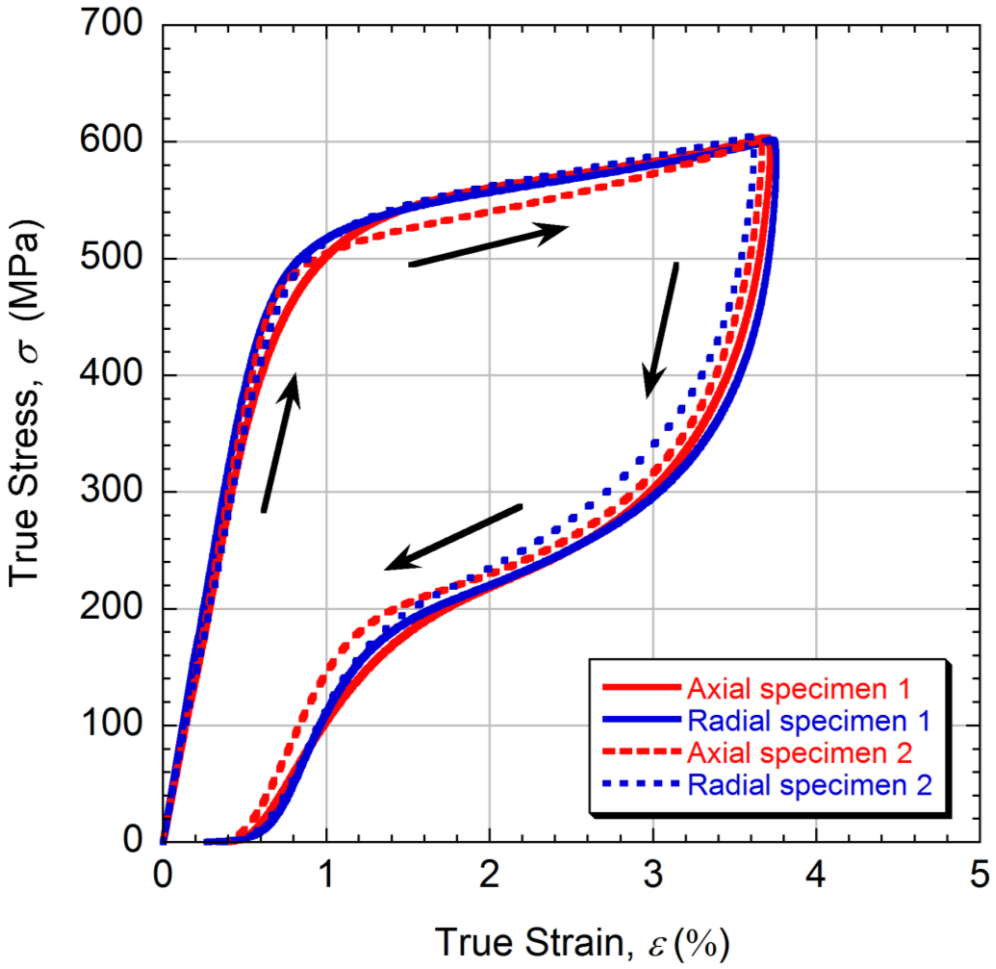

Figure 8.7. Stress-strain plots, during loading and unloading, for uniaxial compression in axial and radial directions (extruded rod coordinate system), from testing of 2 samples in each case. T = 20˚C (293K).

It can be seen from this figure that, within a small margin, there are no significant differences between the datasets, providing evidence that the material is effectively isotropic. Thus, although the sample has a <110> austenite phase texture, this does not translate into noticeable anisotropy in terms of the mechanical behaviour.

8.5. Superelastic Loop Parameter Values

According to the definition of superelastic limit established previously, the material parameter values commonly used to define the stress-strain curve of NiTi are shown in Figure 8.8, using the axial specimen 1 in Figure 8.7 as a “target” or “correct” curve. These superelastic parameter values will be used as inputs when modelling the superelastic behaviour of NiTi [63]. Some authors define this stress-strain curve differently [71], in which case other material parameters would be required. The moduli of the phases were measured via RFDA (§5.5). The measurements were made at room

temperature (~20˚C) for the austenitic phase, which produced a modulus of 72 GPa ± 1.0 GPa. This value agrees well with the value obtained via uniaxial compression, using strain gauges.

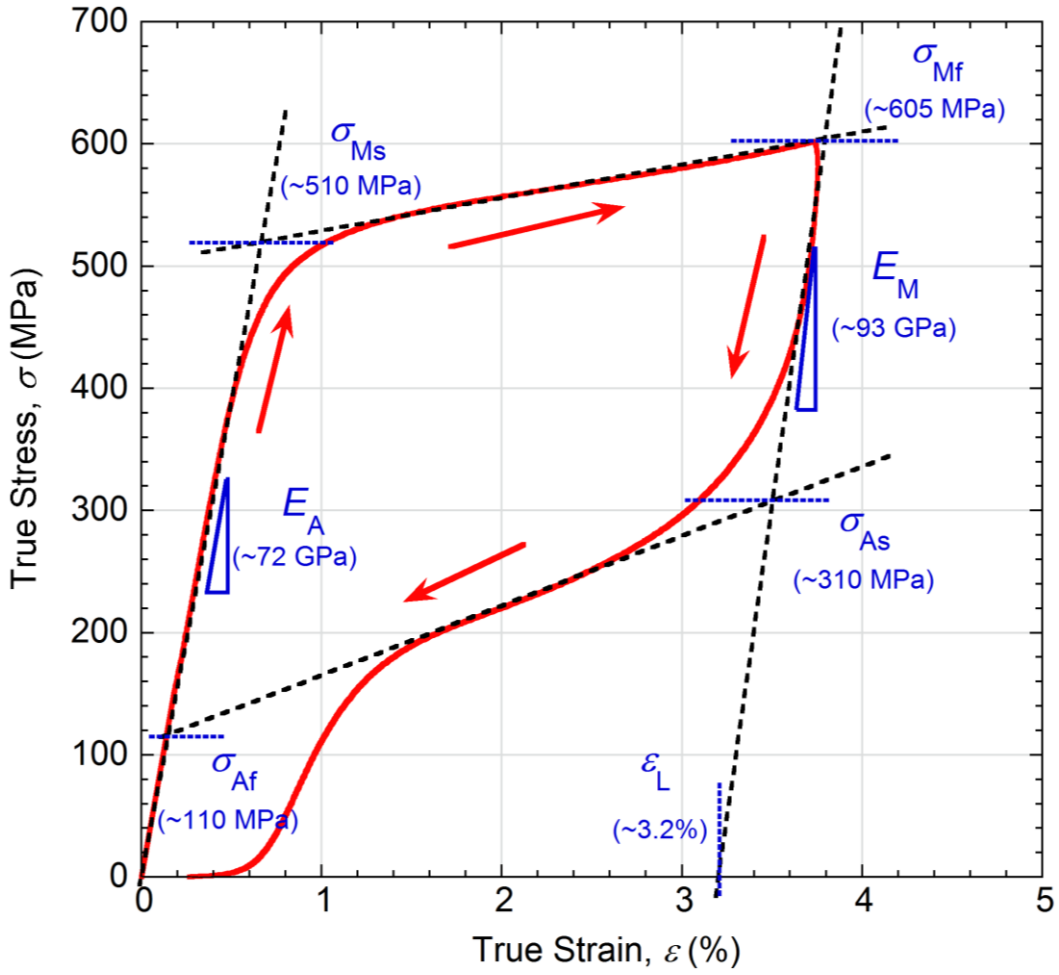

Figure 8.8. Stress-strain plot with 7 of the parameters required for input into the FEM model for SE deformation.

For the martensitic phase, the modulus determined via RFDA (§5.5) was 93 GPa ± 1.0 GPa. Some controversy concerning the modulus of this martensitic phase has been reported in the literature [5], with values in the range between 28-41 GPa being reported in some cases. However, Sittner and co-authors [5] reported that this low Young's modulus value is not valid for compression and other deformation modes. According to this research paper [5], much higher values (90-120 GPa) have been obtained from both mechanical testing and X-Ray (or neutron) diffraction methods (evaluating lattice strains from relative changes in lattice spacing).

Another material parameter, used as input in some material formulations, is the temperature coefficient of the phase transition stress (*C*), which can be extracted from the stress-strain-temperature diagram (§3.4). According to the Clausius-Clapeyron relationship, the stress required to induce the transformation increases linearly with temperature. This implies that *C* can be inferred from two points (transition stress, temperature). The transition temperatures were obtained from DSC at zero stress (§5.2). Thus, these points can be combined with those obtained from the stress-strain curve (see Figure 8.8) at room temperature. The outcome of this procedure is the stress-temperature plot presented in Figure 8.9.

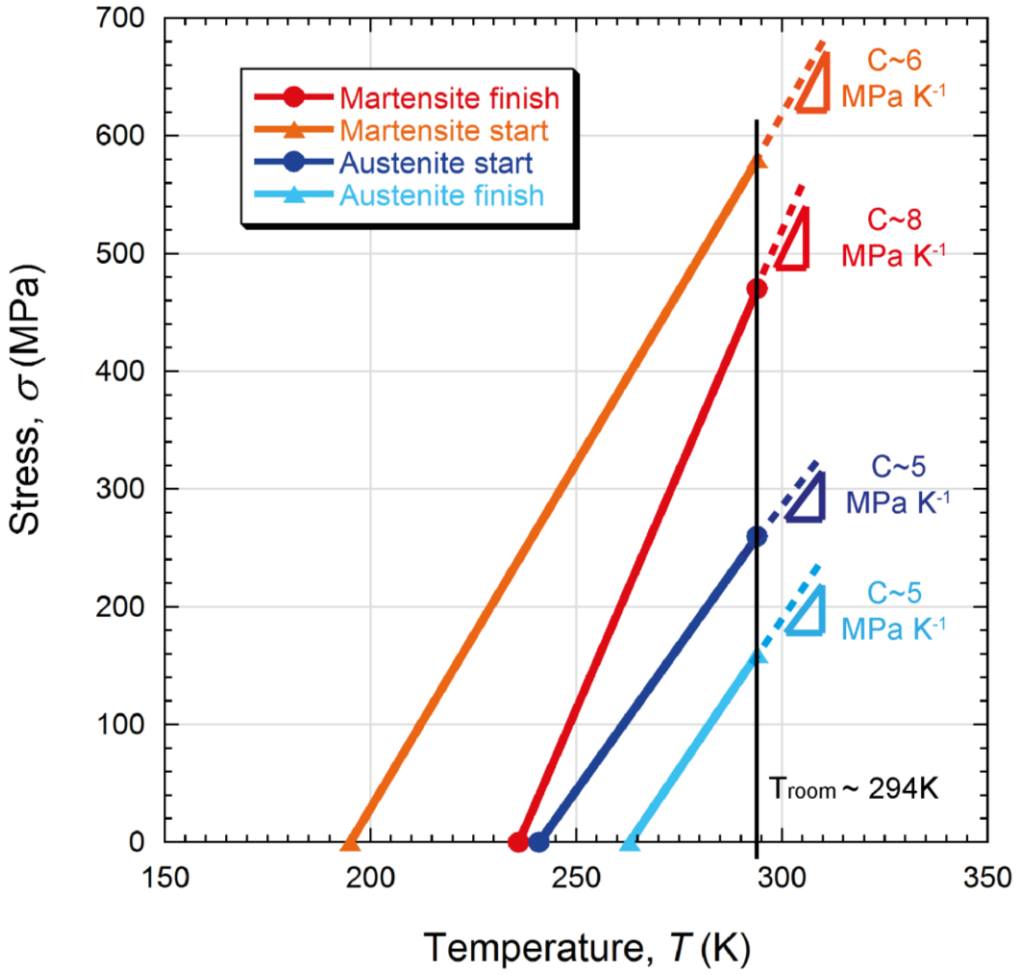

Figure 8.9. Stress-temperature plot obtained from stress-free DSC tests (Figure 6.2) and stress-strain tests (Figure 7.6) at room temperature (~294 K).

Numerical averages between the curves obtained for each phase gave values of 7 MPa K^{-1} for the martensitic phase and 5 MPa K^{-1} for the austenitic phase. These values are also within the range found in the scientific literature [5, 34, 45, 57].

This parameter is important when modelling is performed at a different temperature at which the experiments were carried out.

8.6. Stress-Strain Curves as a Function of Temperature

Stress-strain plots were also obtained at different temperatures, as shown in Figure 8.10. As demonstrated previously, the material does not show significant anisotropy, and for the purposes of this section, the axial direction of the rod is the loading direction.

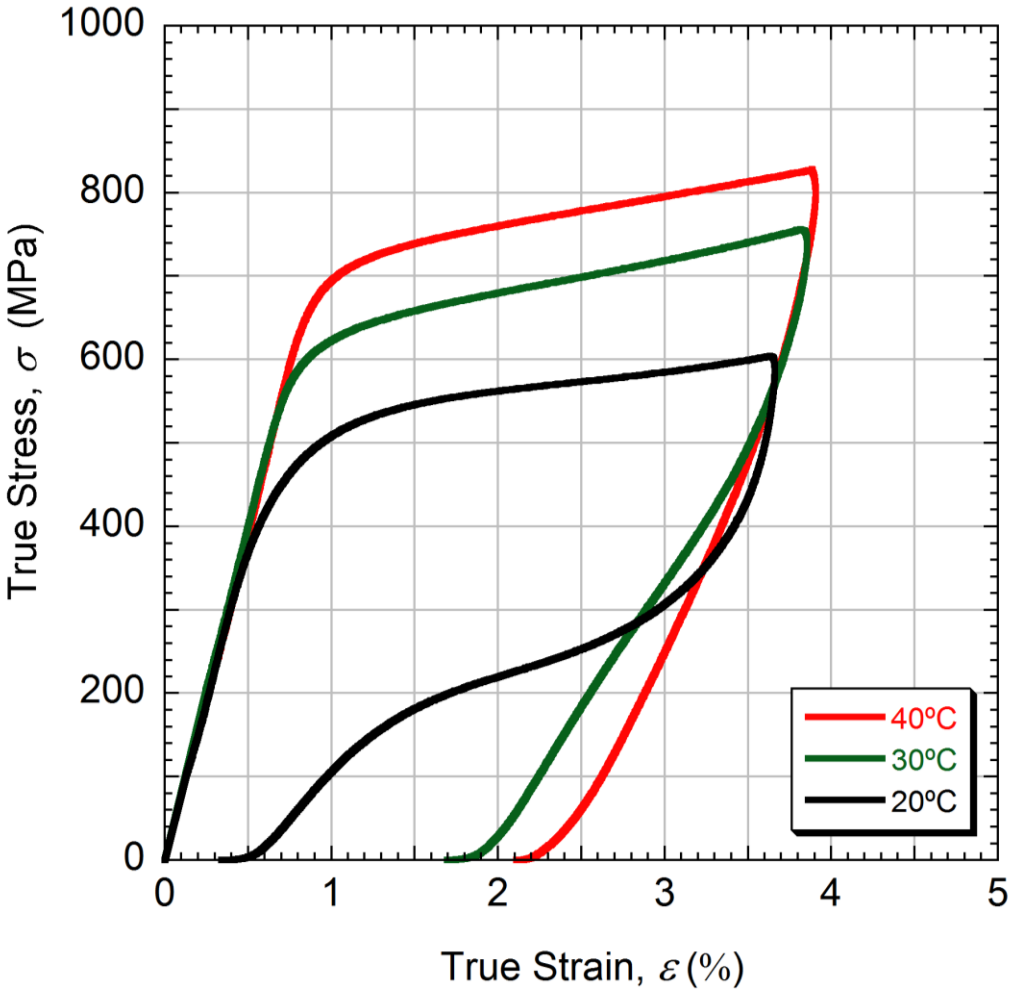

Figure 8.10. Stress-strain plots obtained from uniaxial compression of NiTi cubes (in the axial direction) at different temperatures.

Specimens tested at higher temperatures (above room temperature of ~20˚C) do not show evidence of superelastic recovery upon unloading, having a relatively large amount of “unrecovered” deformation instead. This is related to the decrease in the stress to induce slip as the temperature increases. This stress, together with the stress

to induce martensite, will delimit a “region of superelasticity” in the stress-temperature diagram, shown in Figure 2.8. In this plot, the line representing the critical stress to induce martensite, σ_{Ms}, has a positive gradient, since this stress increases with temperature, from the Clausius-Clapeyron relationship. The line representing the stress required to induce slip decreases with temperature, since dislocation motion becomes easier at higher temperatures, due to reduced energy barriers.

The austenite finish temperature, A_f, in this case, is -10˚C, which indicates that tests performed over 30˚C might have fallen out of the region of interest. NiTi alloys usually present a very narrow temperature range within which superelasticity can occur [45]. In this regard, these uniaxial tests provided guidance for the indentation experiments, meaning that testing above room temperature must not be performed, in order to avoid inducing plasticity.

8.7. Modelling of Uniaxial Compression

8.7.1. Issues with the Elasticity in the Compression Rig

The UMAT used, in this specific case, was the one embedded in ABAQUS, proposed by Auricchio and Taylor [27].

Parameter	Symbol	Value
Modulus of austenite	E_A	72 GPa
Modulus of martensite	E_M	93 GPa
Transformation strain	ε_L	0.032
Martensite start stress	σ_{Ms}	510 MPa
Martensite finish stress	σ_{Mf}	605 MPa
Austenite start stress	σ_{As}	330 MPa
Austenite finish stress	σ_{Af}	110 MPa
Temperature coefficient of phase transition stress (loading)	C_A	5 MPa K^{-1}
Temperature coefficient of phase transition stress (unloading)	C_M	7 MPa K^{-1}

Table 8.1. Parameter values obtained in the current work from the experimental stress-strain curve, for the formulation proposed by Auricchio and Taylor [27].

A summary of the material parameter values obtained from the uniaxial compression testing of NiTi cubes used in this work are presented in Table 8.1. These parameters were obtained via uniaxial compression (see §2.4). The stress fields in both specimen and platens are illustrated in Figure 8.11.

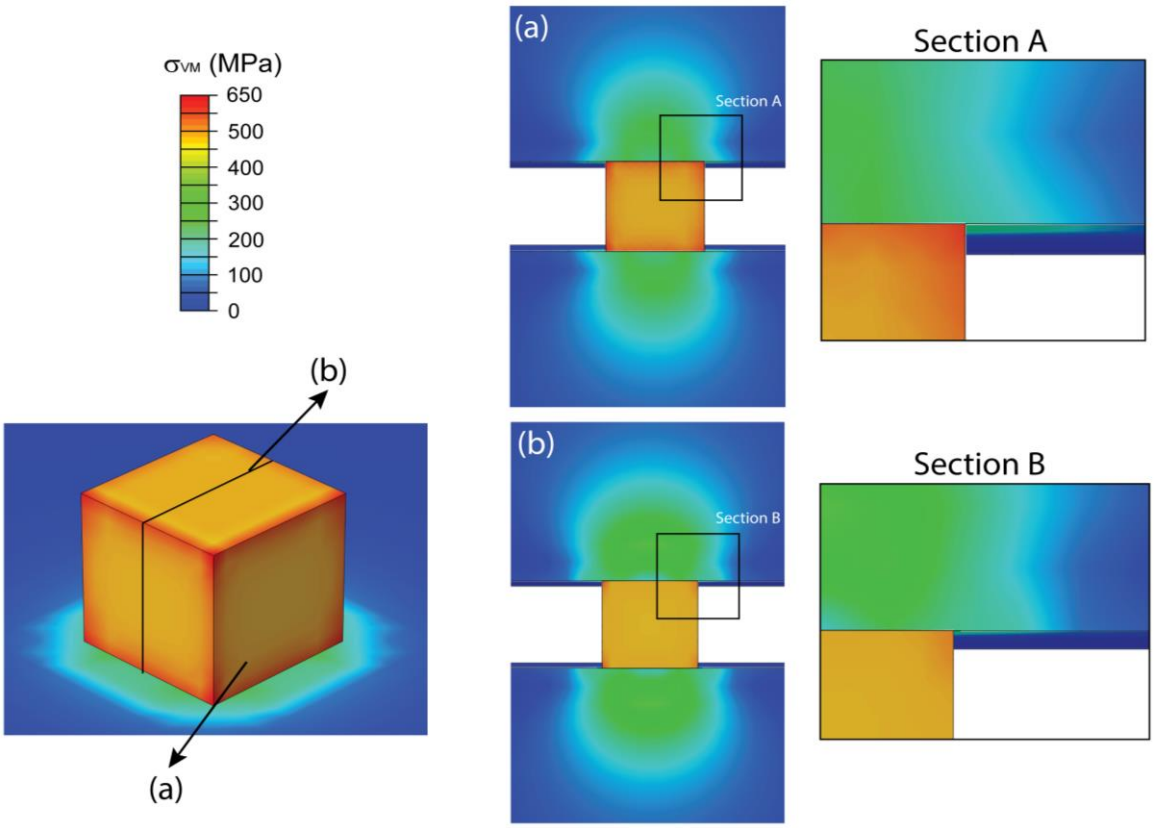

Figure 8.11. Stress fields of compression testing fixtures with focus on specimen undergoing compression: (a) One of the edge facets and (b) Cut-through view halfway into the specimen.

As expected, the specimen had a high-stress region (at least slightly higher than the martensite finish stress) around the edges and corners. These areas seem to be less pronounced further into the specimen (away from the corners). It is worth noting that stresses generated in the platens are well below their yield stresses (<1800 MPa). At a microscopic level, despite being relatively stiff (Young's modulus ~195 GPa), the stainless-steel compression platens tend to deform around the specimen, which causes the modulus of austenite (E_A) to be less steep than its expected value when measuring the displacement of the top platen.

As a result of the compliance, the measured strains appear to be higher than their "correct" (experimental) values. The outcome of the strain gauge, however, is not affected by the elasticity of the platens, since they are monitoring strains directly on

the specimen. This is also captured by the modelled stress-strain curves shown in Figure 8.12. These results highlight the importance of understanding the strains measured by the eddy current transducer. Furthermore, it is essential to establish a procedure to remove the compliance of the system from the data in order to correct the results from the mechanical testing.

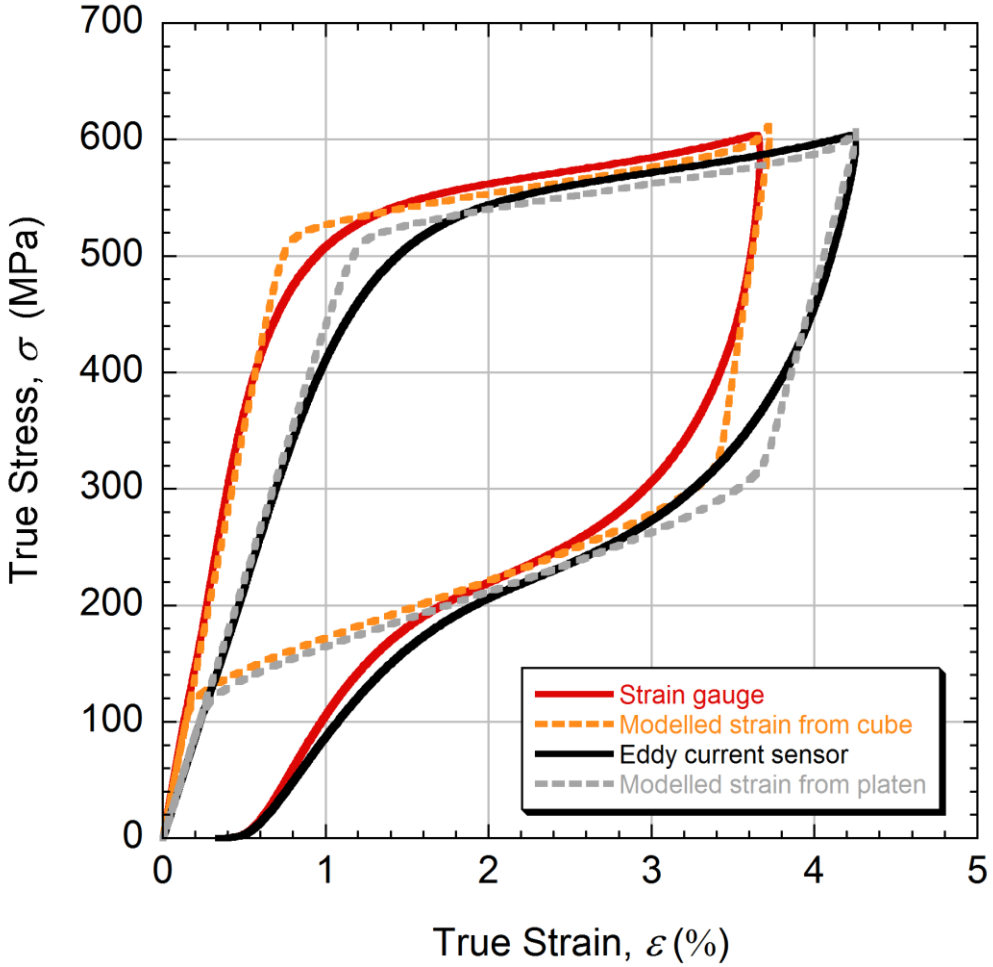

Figure 8.12. Comparison between FE modelled stress-strain curves highlighting the modelled strains measured at different locations (specimen and top platen).

8.7.2. Modelling Minor Stress-Strain Loops

Minor stress-strain loops have been modelled in this section using different material formulations. The superelastic loops were modelled with both ABAQUS-embedded UMAT [27] and open-source UMAT proposed by Lagoudas et al. [71]. The later is a constitutive model with different forms of the transformation hardening function (§3.5.2) and it needs more experimental input parameters than the one embedded in ABAQUS [27] (see Table 6.1). A summary of the parameters for the UMAT proposed

by Lagoudas et al. [71] is shown in Table 8.2. Some of these parameters are material constants and were taken from the literature [34, 53].

Material properties	Symbol	Value
Phase transition parameters (from stress-strain curve)		
Martensite start stress	σ_{Ms}	510
Transformation strain	ε_L	0.032
Austenite start stress	σ_{As}	330
Temperature coefficient of phase transition stress (loading)	C_A	5 MPa K^{-1}
Temperature coefficient of phase transition stress (unloading)	C_M	7 MPa K^{-1}
Elastic constants		
Modulus of Austenite	E_A	72 GPa
Modulus of Martensite	E_M	93 GPa
Poisson's ratio of austenite	ν_A	0.33
Poisson's ratio of martensite	ν_M	0.33
Phase transformation temperatures (DSC)		
Martensite start temperature	M_s	236K
Martensite finish temperature	M_f	195K
Austenite start temperature	A_s	241K
Austenite finish temperature	A_f	263K
Density and thermal properties		
Density	ρ	6450 Kg/m^3
Coefficient of thermal expansion of austenite	α_A	11.0 x 10^{-6} K^{-1}
Coefficient of thermal expansion of martensite	α_M	6.6 x 10^{-6} K^{-1}
Specific heat	c	329 J/(KgK)
Thermal conductivity	K	22 W/(mK)

Table 8.2. Material parameters for NiTi alloys [34, 53] together with DSC transition temperatures for use with the energy-based formulation proposed by Lagoudas et al. [71].

A comparison between modelled (with different formulations) and experimental curves is presented in Figure 8.13 for the different approaches. In general, the formulations capture well the material behaviour (major and minor loops) during the loading, except the one with the exponential hardening function. During unloading, in terms of major loops, the approaches give a reasonable agreement with the overall shape of the curve, but it is quite poor towards the end. The unrecovered deformation (less than 0.5% fully unloaded) might be attributed to retention of residual martensite, mismatch in grain boundaries and other irreversible phenomena

(i.e. dislocation motion) [53, 137]. This has also been observed in the literature [15, 34]. This is unsurprising, since the interactions between plastic (dislocation glide) and superelastic (phase transformation) strains will, in reality, be highly complex during compression (and even more complex during indentation). Even at low strains, some degree of nucleation and glide of dislocations is expected. The density and distribution of dislocations will affect the capacity for nucleation and growth of martensitic variants in the parent phase, and for their subsequent reorientation.

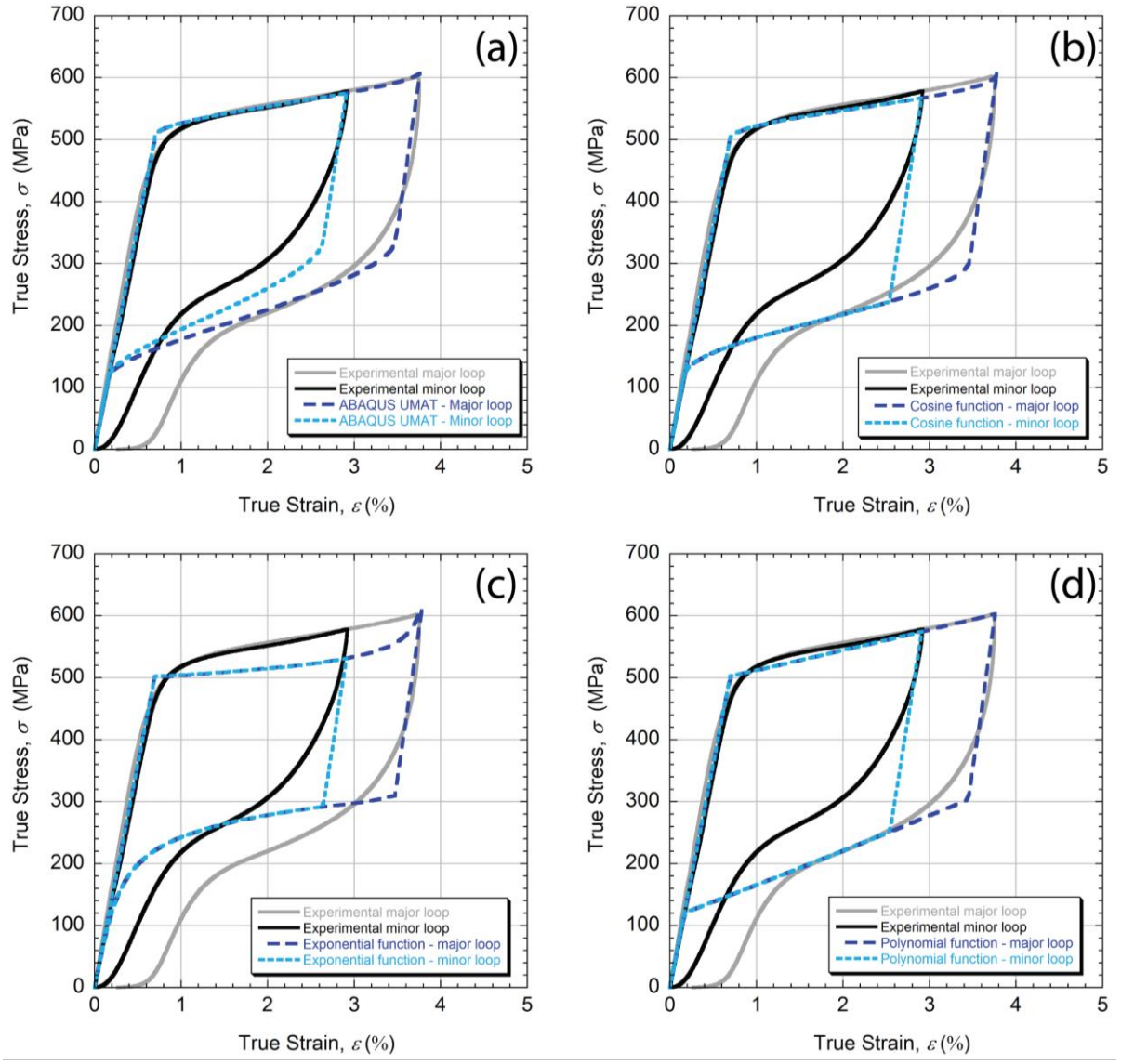

Figure 8.13. Comparison between modelled and experimental stress-strain curves: (a) modelled with an ABAQUS-embedded UMAT [27] and with a unified constitutive model [71] with (b) cosine, (c) exponential and (d) polynomial “flow rule” functions.

Regarding the minor loops upon unloading, all formulations overestimate the total dissipation of energy. This dissipation is related to the reorientation of martensite,

which is being poorly captured by the current formulations. NiTi exhibits a complex behaviour, and the minor-loop issue has been approached in the literature [75, 77, 80, 138, 139], but so far is still not well-understood.

The main idea behind modelling minor loops is the modification of the transformation function. The ones used here have the unloading path following the major loop, except the one proposed by Auricchio and Taylor [27], shown in Figure 8.13(a). Some formulations have additional minor-loop parameters, controlling the shape of the loop [80, 139]. Those approaches are tailored to specific datasets, under specific loading conditions, which usually requires calibration of such parameters for each case.

It is noteworthy that for modelling purposes, in the context of this research work, the material is considered as a continuous medium, and crystallographic aspects have not been taken into account. The material formulations used here do not take into account different types of martensite variants, and this partially explains the discrepancies between experimental and modelled stress-strain curves. Although the assumption of continuous medium for a polycrystalline material is reasonable, some information is lost in this analysis, as the contributions of the internal friction between martensite variants affect the net response.

8.8. Summary

The following was learnt from this chapter:

- Both conventional elastic deformation and superelastic deformation do involve a volume change, the former being $(1-2\nu)$ times the axial compressive strain and the latter being about -0.4% in this case. These are both very small, so the assumption of constant volume should be acceptable for these purposes. In this context, both stress and strain levels can be converted from nominal into true values, using the standard expressions.

- Some issues that might induce errors when measuring strains by “indirect” methods are the deformation of the compression platens, and the loaded faces not being perfectly parallel or normal to the loading axis. Both were taken into account during the preparation for uniaxial compression experiments.

- The compliance of the platens affected the data from the displacement transducer. The platens tend to deform around the specimen, which causes the initial gradient of the stress-strain curve (modulus of austenite) to be much lower than expected. This affected the entire curve, and the measured strains appeared to be higher than their “correct” values. This was solved by using strain gauges, directly to the specimens.

- The strain gauges are limited by their low strain range of deformation. To solve this, a systematic compliance-removal procedure was established. The strains measured off the eddy current sensor were corrected with the strains measured off the strain gauge at the same stress interval. This generated a compliance value of ~2.1 μm kN^{-1}.

- The effect of compliance was also studied by modelling. As shown by the stress field, the specimen had high-stress regions around the edges and corners. These areas seem to be less pronounced further into the specimen. At a microscopic level, despite being relatively stiff, the stainless-steel compression platens tend to deform around the specimen, which caused the modulus of austenite to be less steep than its expected value when measuring the displacement off the eddy current transducer (top platen).

- The superelastic limit was experimentally established from stress-strain plots. This limit was defined as the point at which the material is fully transformed into martensite. The phase transition is completed at the end of the plateau during the forward transformation. For this particular case, the superelastic limit was below 4%. The stress-strain loop obtained at this limit is known as major superelastic loop. Other loops, within this major one, are known as minor superelastic loops.

- Anisotropy has been investigated via mechanical testing (axial and radial directions) and, within a small margin, there were no significant differences between the stress-strain curves, providing evidence that the material is effectively isotropic.

- The “correct” superelastic parameter values for use with the material formulation were identified in the experimental stress-strain curve. These parameter values are used as inputs when modelling the superelastic behaviour of NiTi. In this work, they will be the “target” during the inverse operation (e.i. inferring stress-strain parameters from indentation data).

- Specimens tested at higher temperatures (above room temperature of ~20˚C) did not show evidence of superelastic recovery upon unloading, having a relatively large amount of “unrecovered” deformation instead. This is related to the decrease in the stress to induce slip as the temperature increases. This stress, together with the stress to induce martensite, will delimit a “region of superelasticity” in the stress-temperature diagram.

- In general, the formulations captured well the material behaviour (major and minor loops) during the loading, except the one with the exponential flow function. During unloading, in terms of major loops, the approaches give a reasonable agreement with the overall shape of the curve, but it is quite poor towards the end. Regarding minor loops upon unloading, all formulations overestimate the total dissipation of energy. NiTi exhibits a complex behaviour, and the minor-loop issue has been approached in the literature, but so far is still not well-understood.

9. INDENTATION TESTING

9.1. Considerations for the Design of the Indentation Rig

9.1.1. Choice of Indenter

There are several powerful motivations for using spherical indenters. One of these is that, since it is not a self-similar shape, the stress and strain fields change qualitatively as penetration takes place. Hence, the information being obtained over different depth ranges is analogous to carrying out separate tests with different indenter shapes (reducing the likelihood of different stress-strain curves giving very similar load-displacement plots). This point has been clarified by Dean and Clyne [9].

There are also more practical motivations. One is that a sphere is much less prone to becoming damaged than are shapes having edges or points, and it is also easier to specify and manufacture. Spheres having diameters in the preferred range of about 1-8 mm (see §9.1.2 below) are cheap and readily obtained. There is also reduced risk with spheres of encountering the computational problems that are often associated with simulation of behaviour in regions of high local curvature (edges or points) (see Figure 5.1). Furthermore, for the specific case of superelasticity, sharp indenters would generate high stress at very shallow penetrations, far beyond the superelastic limit, which would induce unwanted conventional plasticity in the material.

Finally, at least with (approximately) isotropic materials, a spherical indenter allows the FEM modelling to be radially symmetric (2D), which is not possible with many shaped indenters. The potential need for a large number of iterative FEM runs makes this a more significant issue than it would be under most other circumstances. The work described in this thesis relates to the use of spherical indenters.

9.1.2. Length Scale Effects

It is essential when the objective is to extract bulk properties, to indent on a suitable scale, while retaining the key advantages of being able to test small and flat samples, to carry out point-to-point mapping of properties, etc. In particular, the volume being interrogated must have a (stress-strain) response that is representative of the bulk.

It is on this mesoscale (such that indents are large enough for a representative material response, but small enough to allow small samples and mapping) that this type of work needs to be focused.

The minimum indent size for a representative response depends on the microstructure, but in many cases, it will require deformation of an assembly of grains − at least about a dozen and preferably more. Only when such an assembly is being deformed it is possible to capture the influence, not only of the crystallographic texture of the material, but also of the way that cooperative deformation of neighbouring grains takes place. This is likely to be affected, not only by texture but also by factors such as the ease of grain boundary sliding. Simply taking the average of the load-displacement responses from indents made in a large number of individual grains will not even approximately capture the bulk response. (The same arguments would apply to carry out conventional uniaxial tests on a set of single crystal samples having orientations representative of the texture of a polycrystal). A crude rule of thumb might be that, viewed on the free surface, the indent should straddle at least “several” grains. The corresponding minimum indent diameter might range from below 1 μm to above 1 mm, but it will undoubtedly be small enough in most cases to offer the attractions outlined above.

Grain sizes of around 100 μm or more are, of course, quite common. In general, therefore, indention diameters should be at least a few hundred μm. This does require relatively large indenters (~mm dimensions) and therefore large loads (~ hundreds of N, or even several kN), which may be beyond the range of some indentation systems (but perhaps below the commonly-used ranges of some conventional mechanical testing systems). However, systems in this “intermediate” load range are in general easier and cheaper to build and use than either of the other two types of system. Moreover, a relatively coarse scale of indentation minimises the problems associated with surface roughness, oxide films, contamination and so forth.

There is also a further issue, which relates to the indenter penetration depth, δ, as a ratio to the indenter radius, R. It might be imagined that, while the load needed to penetrate to a given δ/R, and the stresses in the material, would depend strongly on the material (hardness), but the strains would not. In fact, in the superelasticity case,

the indentation depths are expected to be very shallow in order to avoid conventional plasticity. The corresponding δ/R will be established via FE modelling.

9.1.3. Set-up for Indentation Testing

The indentation rig was designed to avoid compliance interference (e.g. the only component effectively loaded is the sphere into the sample). This is very critical since the maximum displacement to induce superelasticity in this work does not exceed 14 μm. A schematic illustration of the indentation test set-up is shown in Figure 9.1.

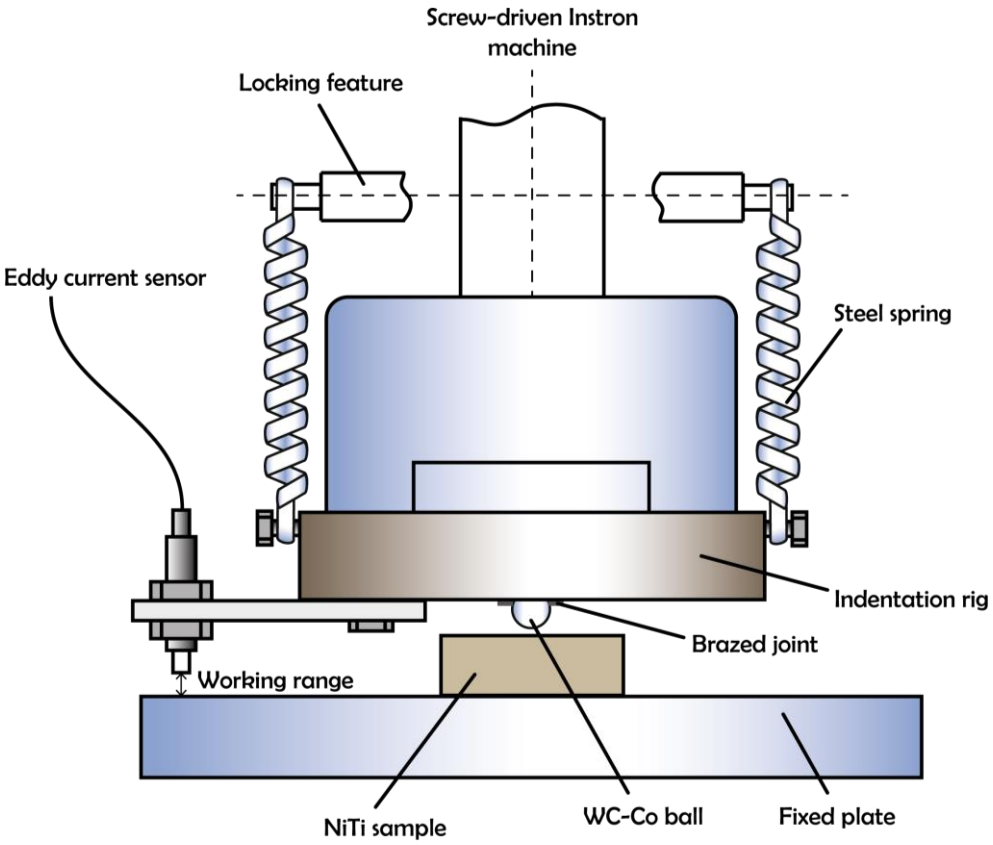

Figure 9.1. Schematic illustration of the indentation test set-up.

The displacement of the indenter rig was measured simultaneously by the eddy current transducer and the crosshead of the machine. The rig was secured in place by stiff steel springs, pushing it against the loading grip. The sphere was located in a matching recess in a stainless-steel housing, where it was secured by brazing. This recess was machined using a 2 mm diameter ball-nosed end mill. The spheres are made of a WC-Co cermet and supplied by Bearing Warehouse Ltd. WC-based cermets have hardness and stiffness values high enough for most purposes. However, the elasticity of the sphere is taken into account in the model (§6.2).

The indents were therefore created using relatively large spheres with diameters of 4 and 8 mm. It is essential that a representative volume of material should be tested. In this case, with a grain size of about 30-70 μm (see details in §5.4), an indent diameter of at least a few hundred microns, and a depth of the order of 14 μm, is likely to be suitable. As with the uniaxial compression testing, these tests were carried out both along and transverse to the extrusion axis. For the axial testing, indents were made at several radial locations (since it is possible that these experienced different degrees of plastic strain during extrusion, and hence have different textures). For the transverse testing, the indentation was carried out along a radial direction.

9.1.4. Compliance Calibration

Compliance calibration was also needed here since it is crucial in a work of this type that the displacement data should be obtained under conditions that correspond closely to those being simulated in the model. The compliance was measured by pushing the indenter into a matched recess (~500 μm deep), as shown in Figure 9.2, in a 5 mm thick plate of alumina.

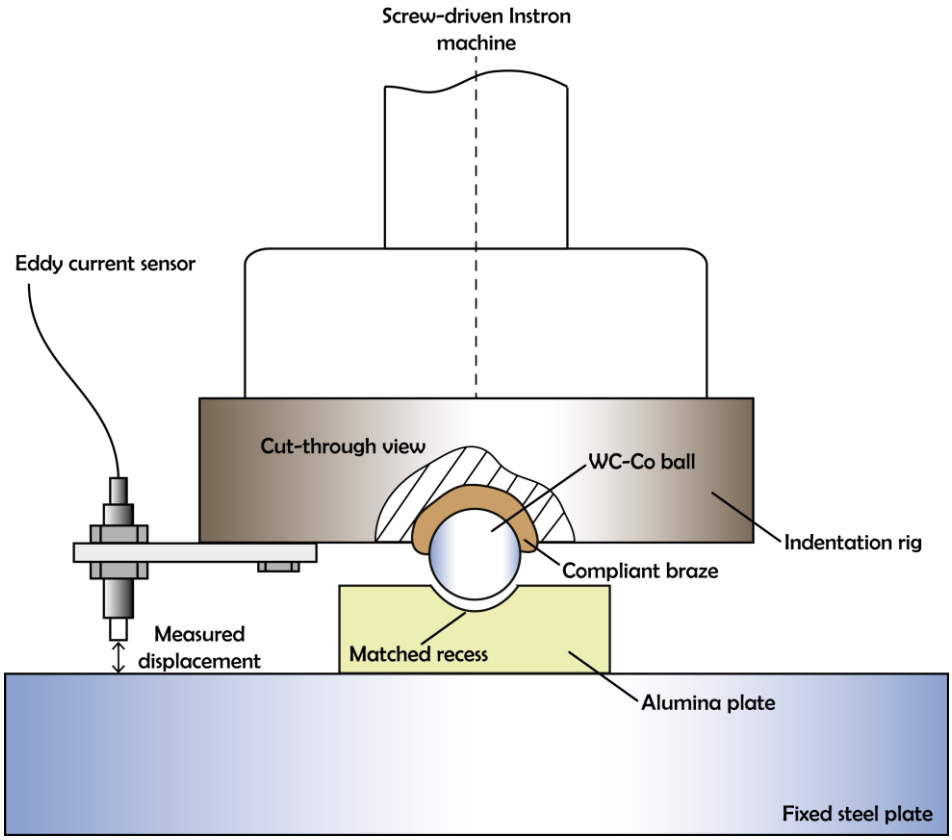

Figure 9.2. Indentation rig under compliance calibration.

The recess was created via abrasive rotational honing with the same type of indenter as that used in the tests. The displacement was simultaneously monitored by the eddy current transducer and the crosshead extension of the screw-driven machine. The load-displacement plots for these cases are shown in Figure 9.3. It can be seen that there is a short bedding-down regime (curvature at the beginning of the loading) followed by a straight line whose gradient is the compliance (for spheres with diameters of 4 and 8 mm). The contribution to the compliance from the alumina plate itself is considered to be negligible.

It is worth noting the first runs in both cases (in red) tend to be more compliant, especially for the 8-mm-sphere, since the braze was being accommodated into the housing upon loading. The following four runs showed reproducible curves given that the braze was already plastically deformed, and the plots overlap entirely.

The displacement measured by the eddy current transducer coped with the compliance of the housing, including the braze layer between indenter and housing, and also that of the top half of the indenter. However, it did not compensate for the (elastic) deformation of the bottom half of the indenter, which could be significant in the early stages of indentation (when the contact area is small, and the stresses and strains in the indenter could be relatively large). This part of the indenter was, therefore, included in the modelled domain. The displacement from the crosshead extension of the machine (measured from the rotation of a worm drive), on the other hand, coped with the compliance of the “entire” frame, including the elasticity of the braze layer and all fixtures (shown in Figure 9.2) experiencing loading. As expected, these compliance values were much higher than the ones measured by the eddy current transducer, as shown in Table 9.1.

Indenter diameters	**Compliance of the braze layer (from eddy current transducer) $\mu m\ kN^{-1}$**	**Compliance of the rig (from extension) $\mu m\ kN^{-1}$**
4 mm	3.3	23.5
8 mm	1.3	21.3

Table 9.1. Compliance values for indenter balls with diameters of 4 mm and 8 mm.

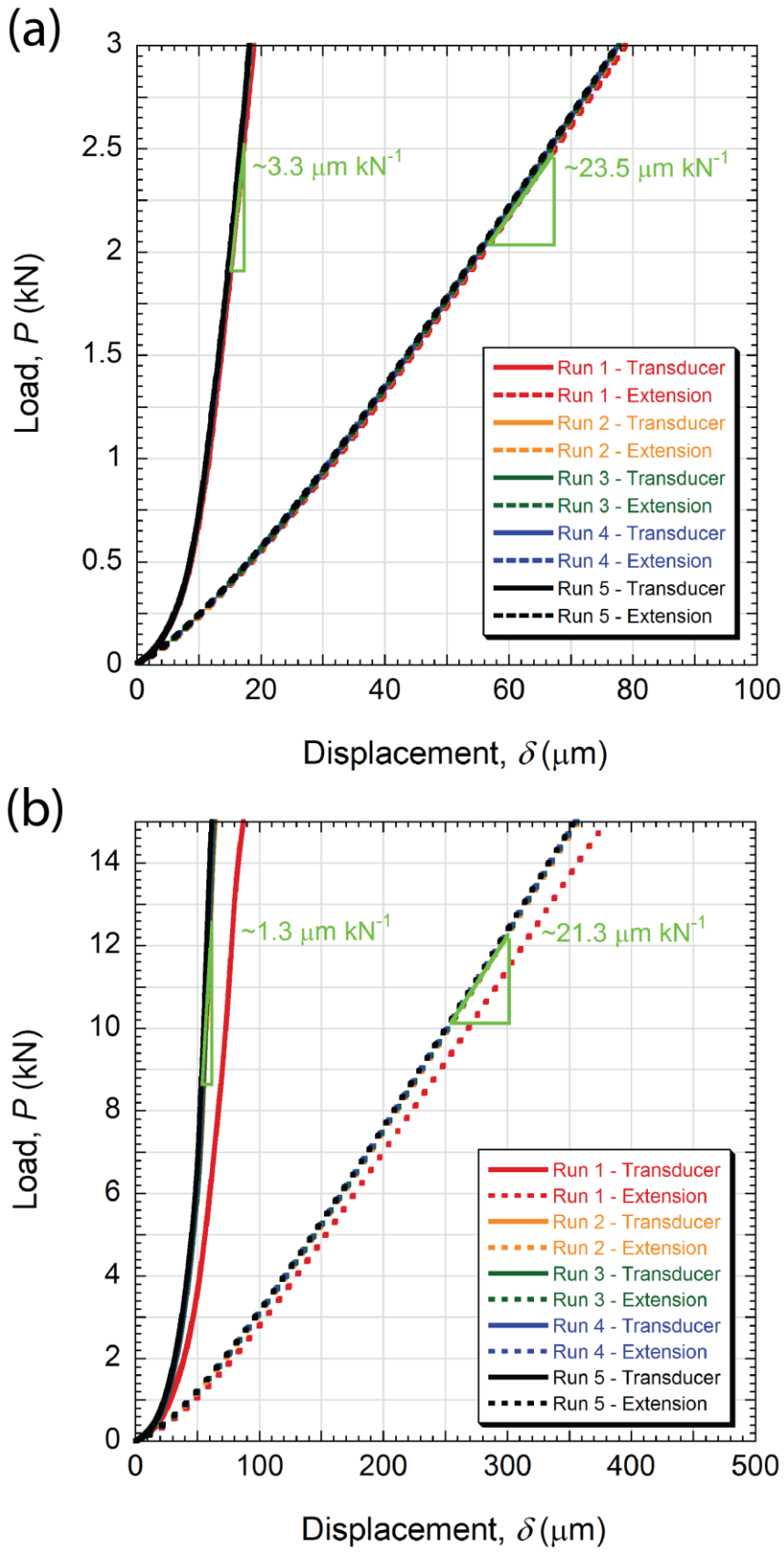

Figure 9.3. Compliance runs for indenter balls with diameters of (a) 4 mm and (b) 8 mm. The displacement was simultaneously monitored by the eddy current transducer and the crosshead extension of the screw-driven machine.

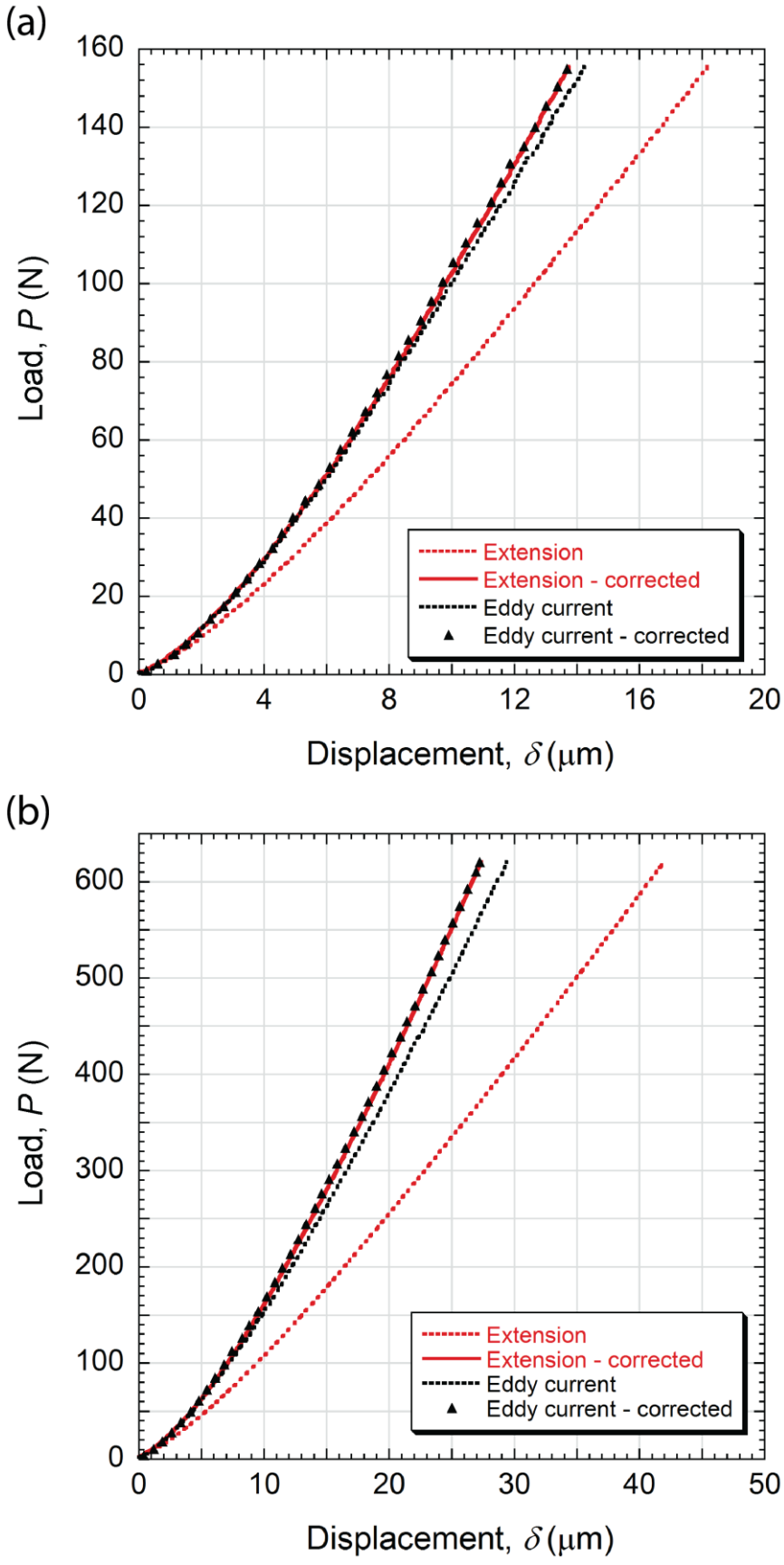

Figure 9.4. Load-displacement curves corrected with compliance values obtained from two indenters with diameters of (a) 4 mm and (b) 8 mm. The displacement was simultaneously monitored by the eddy current transducer and the crosshead extension of the screw-driven machine.

The compliance values from Table 9.1 were then subtracted from the load-displacement plots of the specimens, as shown in Figure 9.4. Unsurprisingly, both types of compliance-corrected curves (with displacements taken from the crosshead extension and the eddy current transducer) lead to very similar results (for both spheres), within a small margin of error, which proved that the compliance calibration procedure was successfully established.

9.2. Indentation Experiments

9.2.1. Loading Rate Dependence

To this end, indentation experiments were performed at four different loading rates, up to the same maximum load (155 N). Representative results are shown in Figure 9.5. More experimental results, including all five indents, run for each case, are presented in Appendix §12.4.

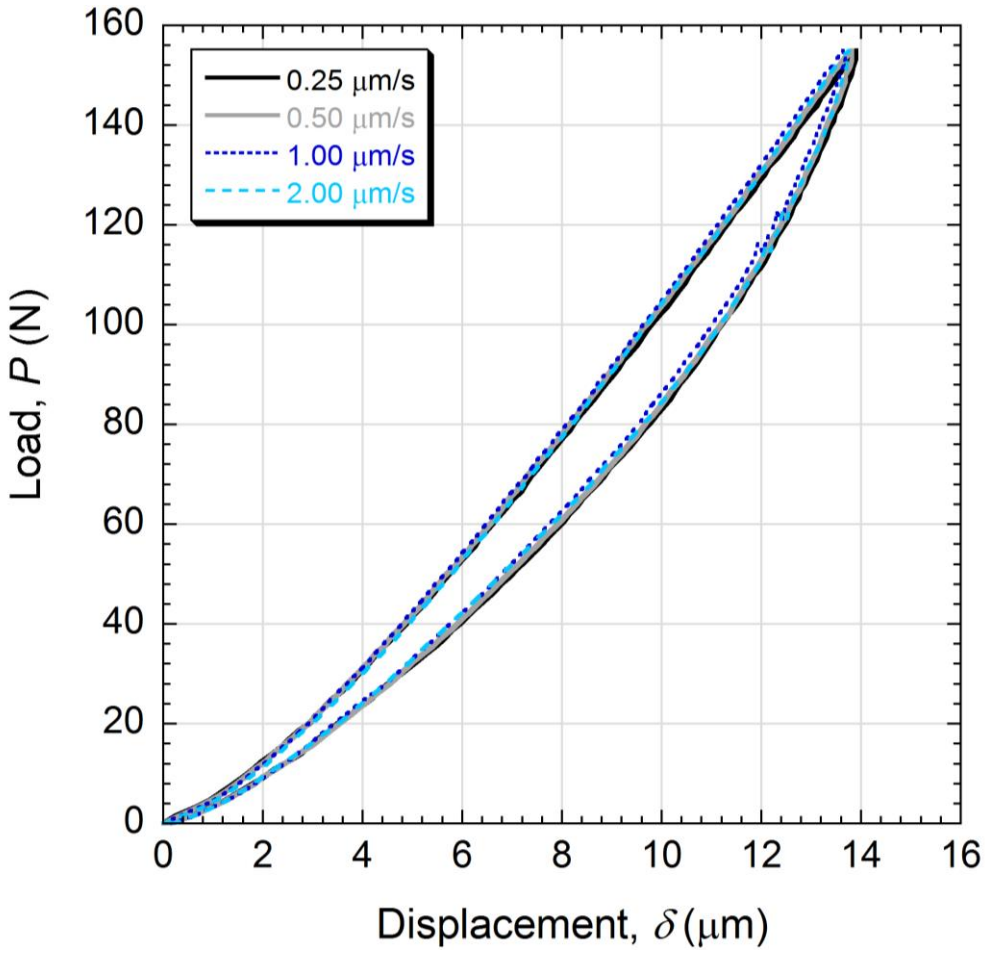

Figure 9.5. Representative (averaged) load-displacement plots obtained at different loading rates at the maximum load of 155N: (a) 0.25 μm/s, (b) 0.50 μm/s, (c) 1.00 μm/s and (d) 2.00 μm/s.

The loading rate can play an important role in indentation testing. In this regard, it is important to establish a range within which the indentation will be carried out with no time-dependence since the FE model does not take creep into account. As presented in Figure 9.5, no significant differences were found between the load-displacement plots obtained within the loading rate range concerned, attesting the rate-independent nature of such experiments. For experimental convenience, in order to avoid creep and to prevent the machine control from dealing with very high loading rates (which may damage the motor), all indents were made at 0.5 μm/s, which is an intermediate rate among the ones analysed. Thus, each indent took around 28 s.

9.3. Superelastic Limit

As mentioned previously, the penetration ratio (δ/R) must be kept low in order to avoid stimulating irrecoverable strains, i.e. creating peak strains above the superelastic limit. However, for an unknown NiTi alloy, it is hard to determine this limit. Experimentally, this can be done by merely indenting the sample at small load interval and checking the surface for “visible indents”. A series of indents, made at different loads, is shown in Figure 9.6.

For this specific material, the indents started becoming visible at loads higher than 150 N. The superelastic limit was precisely determined via FE modelling (see more details in §10.1), at a load of 155 N (δ/R ~ 0.70%). Superelastic deformation, which can only accommodate strains of up to ~4% in this case (stress-strain plot in Figure 8.8), is not expected to be the sole or even the predominant, deformation mode beyond a load of 155 N, so the observation that some of this strain is not recovered upon unloading from 250 N is not surprising, as observed in Figure 9.6. Since superelasticity cannot fully accommodate this deformation (δ/R ~ 1%), this strain will result in the generation of a high density of dislocations, through conventional plastic deformation. The presence of an increased density of dislocations will limit the formation of martensite within the parent phase since they stabilise the parent phase and will oppose its transformation to martensite. Any martensite that does form, however, might not be reversible, since the high dislocation density will both pin and aid the stabilisation of martensitic variants, limiting their reorientation into the parent phase,

upon unloading. Thus, in order to prevent conventional plasticity and, consequently, residual indents, indentation ratios must be kept very low (δ/R < 1%).

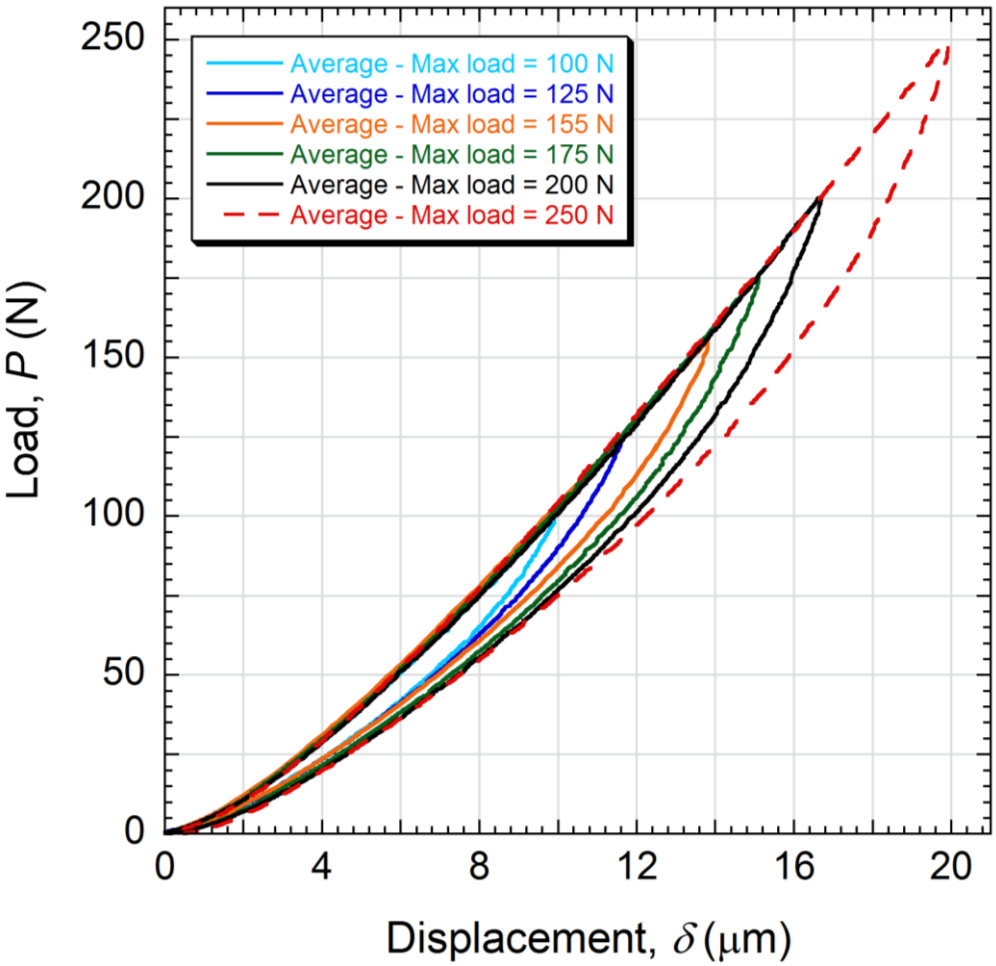

Figure 9.6. Averaged indents obtained at different maximum loads: 100, 125, 150, 175, 200 and 250 N.

9.4. Anisotropy Investigation

As with uniaxial compression testing, indentation testing was carried out both along and transverse to the extrusion axis of the rod. Representative (averaged) load-displacement plots for axial and radial indentation are shown in Figure 9.7. For the axial testing, indents were made at several radial locations (since it is possible that these experienced different degrees of plastic strain during extrusion, and hence have different textures). For the transverse testing, indentation tests were carried out along the radial direction.

As in the uniaxial case, no significant differences were found between these two datasets. This would be expected even if the uniaxial tests had revealed some

anisotropy. In fact, indentation is strongly multi-axial, implying that load-displacement plots obtained from the penetration of a spherical indenter into polycrystalline materials will be independent of the indentation direction. It is also apparent in this figure that, in both cases, there is little or no residual displacement, indicating that the deformation has resulted entirely from (reversible) phase transformations. This is an obvious check to make if the intention is to focus on SE deformation (see §9.3).

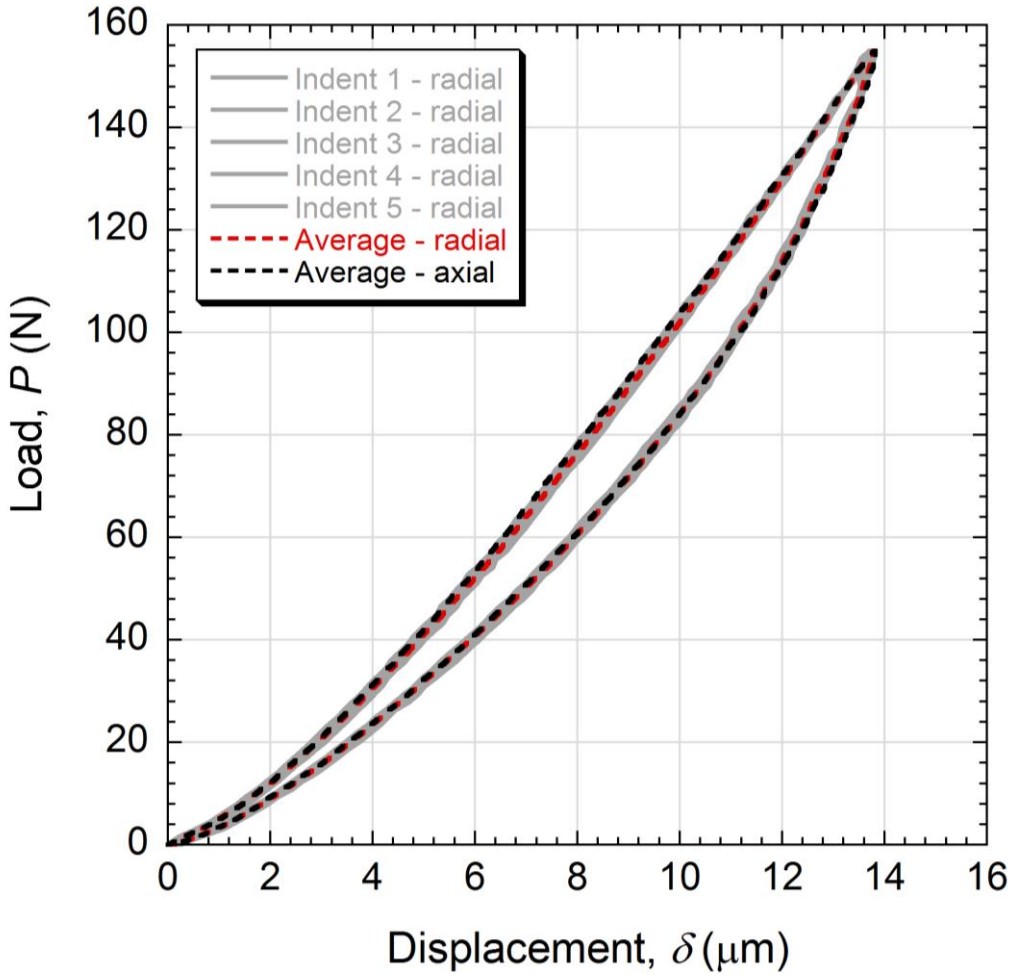

Figure 9.7. Representative (averaged) load-displacement plots obtained during indentation in axial and radial directions.

9.5. Spherical Indenters with Different Diameters

It is possible to correlate the load-displacement plots obtained from spherical indentation with different diameters. An example of indents made with different indenter diameters is shown in Figure 9.8.

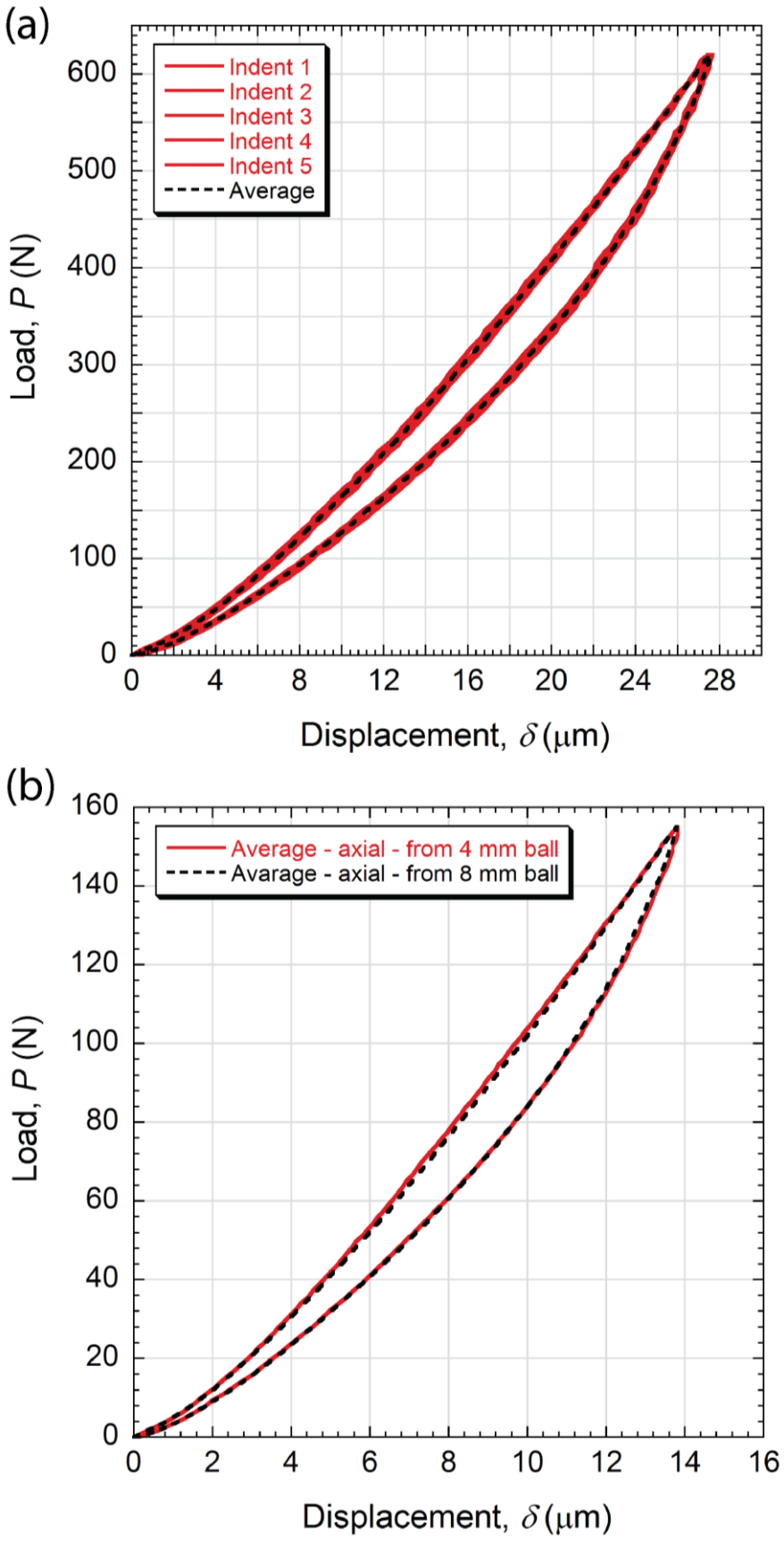

Figure 9.8. (a) Load-displacement plots obtained during indentation in the axial direction at a maximum load of 620 N with a sphere with a diameter of 8 mm; (b) Comparison between (averaged) plots obtained from spherical indentation with two different diameters: 4 mm and “converted” from 8 mm.

It is well-established that the stress and strain fields beneath an indenter are scale-independent [9]. In the example in Figure 9.8, for a family of spherical indenters with radii varying from 2 mm to 4 mm, the fields created by an indentation ratio of, say, 0.7% are identical. The absolute value of the load at this point will be 4 times greater for the latter case, while the penetration will be 2 times.

In Figure 9.8(a), indents were made at a maximum load of 620 N, which is 4 times the indentation load established as being the superelastic limit. This curve can be converted, if necessary, into various “equivalent” load-displacement curves for a family of indenter diameters. In this particular case, its “equivalent” one for a sphere with a diameter of 4 mm is shown in Figure 9.8(b). It is worth noting that the information being provided about the mechanical response of the material is the same, assuming that the volume being interrogated is in both cases large enough to be representative of the bulk response.

The comparison between the curves shows good agreement, as expected. This conversion is important when measuring the indentation load/displacement is an issue. For example, when indenting a particular material, the applied load might be high or low depending on the properties being investigated. If, say, plasticity characteristics are being sought via indentation testing, indent diameters should be at least a few hundred μm and, therefore, relatively high loads will be required (~ hundreds of N, or even several kN) [11]. On the other hand, in the case of superelasticity, very shallow indents should be made (a few tens of μm), implying that reasonably low loads will be required (a few hundred of N, depending on the indenter size). Most mid-range mechanical testing machines have load cells with capacity ranging from 10 to 30 kN, where such low loads would be close to the lower limit of the equipment. Thus, increasing the diameter size will increase the indentation load to a range within which the load cell output tends to be improved.

9.6. Summary

The following was learnt from this chapter:

- There are several practical motivations for using spherical indenters in this work. One is that a sphere is much less prone to becoming damaged than are shapes having edges or points, and it is also easier to specify and manufacture. Spheres are also relatively cheap and readily obtained. There is also reduced risk with spheres of encountering the computational problems that are often associated with simulation of behaviour in regions with edges or points. For the specific case of superelasticity, sharp indenters would generate high stress at very shallow penetrations, far beyond the superelastic limit, which would induce unwanted conventional plasticity in the material.

- The indentation carried out in this work was carried out on “mesoscale”. At this level, indents are large enough for a representative material response (bulk), but small enough to allow small samples and mapping. The minimum indent size for a representative response depends on the microstructure, but in many cases, it will require deformation of an assembly of grains − at least about a dozen and preferably more.

- The indentation rig was designed to avoid compliance influence. The deformation of the fixtures in the rig (including the braze layer) was well-understood. Thus, a compliance calibration procedure was carried out for both eddy current transducer and crosshead of the machine. The compliance values were 3.3 $\mu m\ kN^{-1}$ (transducer only) and 23.5 $\mu m\ kN^{-1}$ (crosshead) for the 4-mm-sphere, and 1.3 $\mu m\ kN^{-1}$ (transducer only) and 21.3 $\mu m\ kN^{-1}$ (crosshead) for the 8-mm-sphere. These values were used to correct the load-displacement curves throughout this work.

- No significant differences were found between the load-displacement plots obtained within the loading rate range concerned, confirming the rate-independent nature of such experiments. Thus, the indents were made at 0.5 $\mu m/s$ in order to prevent experimental issues.

- The superelastic limit was experimentally determined by merely indenting the sample at small load interval and checking the surface for “visible indents”. The indents started becoming visible at loads higher than 150 N. The superelastic limit was precisely determined via FE modelling, at a load of 155 N (δ/R ~ 0.70%). Superelastic deformation, which can only accommodate strains of up to ~4% in this case (stress-strain plot), is not expected to be the sole or even the predominant, deformation mode beyond a load of 155 N.

- As with the uniaxial tests, no significant differences were found between load-displacement plots obtained in different directions (axial and radial). This would be expected even if the uniaxial tests had revealed some anisotropy. In fact, indentation is strongly multi-axial, implying that load-displacement plots obtained from the penetration of a spherical indenter into polycrystalline materials will be independent of the indentation direction.

- Stress and strain fields beneath a spherical indenter are scale-independent. Thus, it is possible to correlate the load-displacement plots obtained with different indenter diameters. Although the indents are different, the information being provided about the mechanical response of the material is the same, assuming that the volume being interrogated is in both cases large enough to be representative of the bulk response. This correlation is important when measuring the indentation load/displacement is an issue.

10. ASSESSMENT OF THE INDENTATION METHODOLOGY

10.1. Experimental Validation of the Methodology

The experimental validation of this proposed methodology will be carried out on a single NiTi alloy, presented in more detail in §5.1. This is the most popular alloy for superelastic applications because of its transition temperature range. Its A_f is designed to be lower than the body temperature (~37°C), which makes it useful for both medical and dental applications [45].

It is not unusual, in a work of this type, to validate a methodology by testing only one alloy composition. Dean and Clyne [9], validated a methodology for inferring plasticity parameters by performing experiments on copper samples. Frost et al. [24] proposed a model that takes into account R-phase contributions on the mechanical behaviour of NiTi, and validated it with one sample of a particular alloy composition. Lagoudas and co-authors [80] also validated a material formulation with a single NiTi alloy.

The experiments were performed several times here, and the results showed that the curves (stress-strain and load-displacement ones) overlap in all cases. As long as the experimental results are not scattered over a significant range and the shape of the curves follows a systematic trend, this can be recognised as a legitimate way of validating numerical codes [140, 141].

10.2. Modelling Indentation with Experimental Uniaxial Data

It is a relatively simple operation to simulate the indentation process, using the set of parameter values fitted to the stress-strain curve (Figure 8.8), and to compare the predicted load-displacement plot with that obtained experimentally. This comparison is shown in Figure 10.1.

The level of agreement between the two curves is good for the loading curve, but poor for the unloading curve. This is not surprising, since the fidelity of the ABAQUS UMAT [27, 63] to the actual stress-strain curve (Figure 8.12) is quite poor towards the end of the unloading.

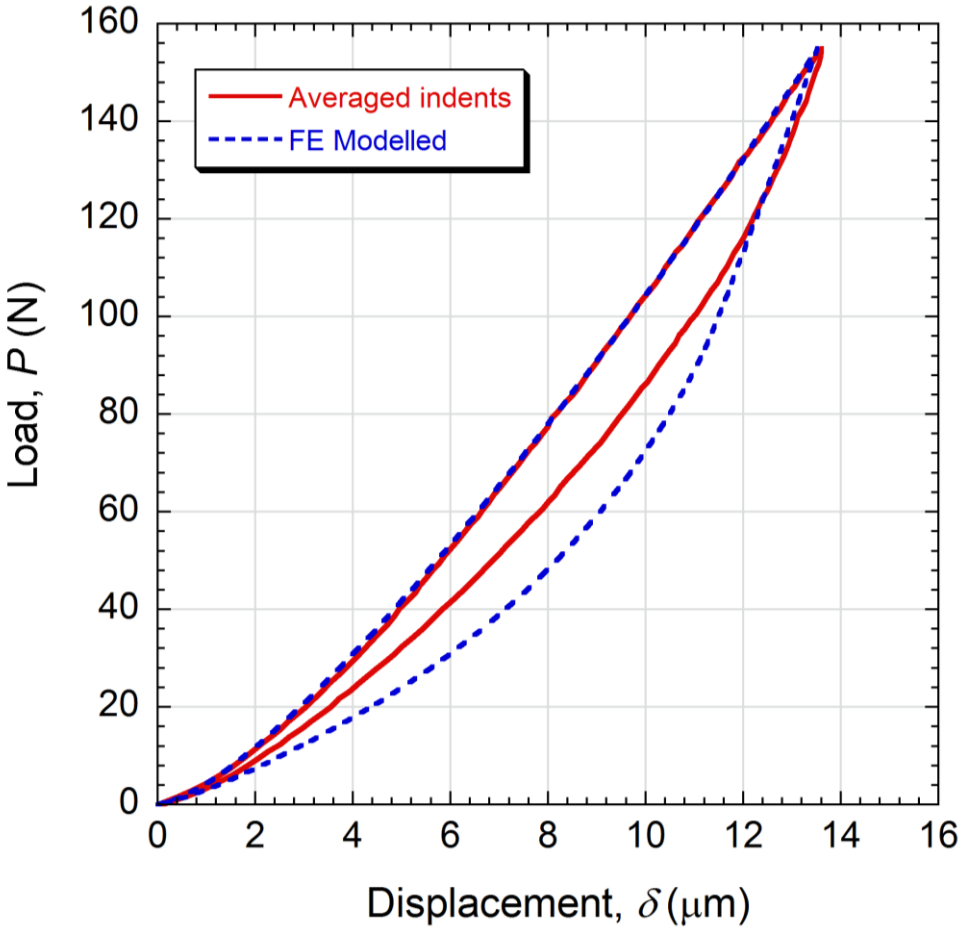

Figure 10.1. Comparison between the indentation load-displacement plots obtained experimentally and by FEM simulation (using the best-fit set of parameter values from the uniaxial stress-strain curve).

The analysis of the strain and stress fields obtained via FEM simulations, shown in Figure 10.2, revealed that most of the volume elements that deform during indentation do not fully transform into martensite, and those will follow minor loops in the stress-strain curve.

The UMAT formulation provides a particularly poor representation of the unloading curves for minor loops. In this context, a comparison between modelled (with different formulations) and experimental uniaxial stress-strain curves, with the loading taken to 2 different levels is shown in Figure 8.13. It can be seen that, for these minor loops, the formulation (Figure 8.13(a)) gives a very poor representation over virtually the complete unloading range (whereas the major loop, for a complete phase transformation, is only poor towards the end). This is a severe limitation of this formulation for modelling of the indentation of SE materials. It seems clear from this figure that, particularly for simulation of indentation, a formulation is needed that

represents these intermediate unloading loops much more closely. Nothing of this type appears to be available at present, at least regarding routines incorporated into commercial FEM packages.

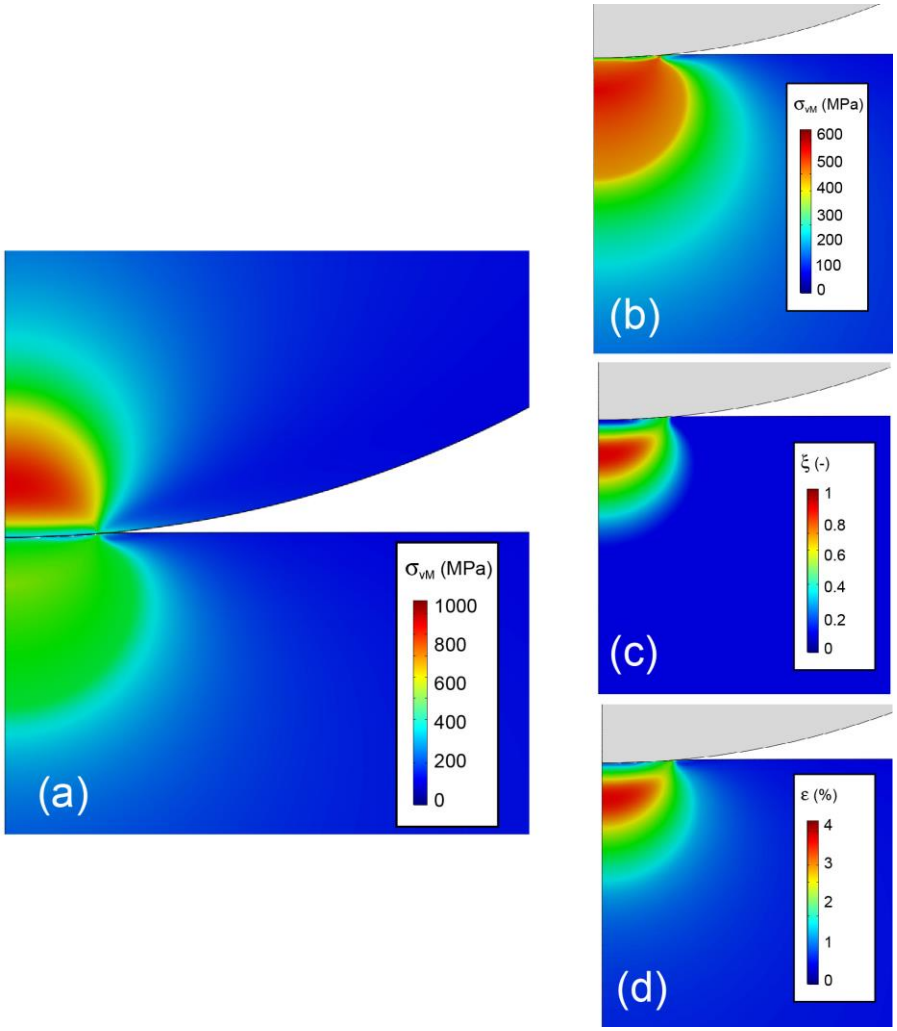

Figure 10.2. Outcomes of FEM simulation of the indentation process obtained using ABAQUS with the set of input parameters shown in Figure 7.6, for an applied load of 155 N and a sphere radius of 2 mm. Fields are shown for the (a) von Mises stress for both sample and spherical indenter, (b) von Mises stress for the sample (only), (c) local volume fraction transformed to martensite and (d) total strain.

10.3. Effect of Interfacial Friction

The effect of interfacial friction is usually simulated via a coefficient of friction, μ, such that sliding between the two surfaces requires a shear stress, given by $\tau = \mu\sigma_n$, where σ_n is the normal stress. The value of such a coefficient is expected to depend on the surface roughness of both indenter and sample, and it is hard to predict. The value of μ was therefore regarded as adjustable, to allow improvement of the fit between experimental and predicted load-displacement plots, as shown in Figure 10.3.

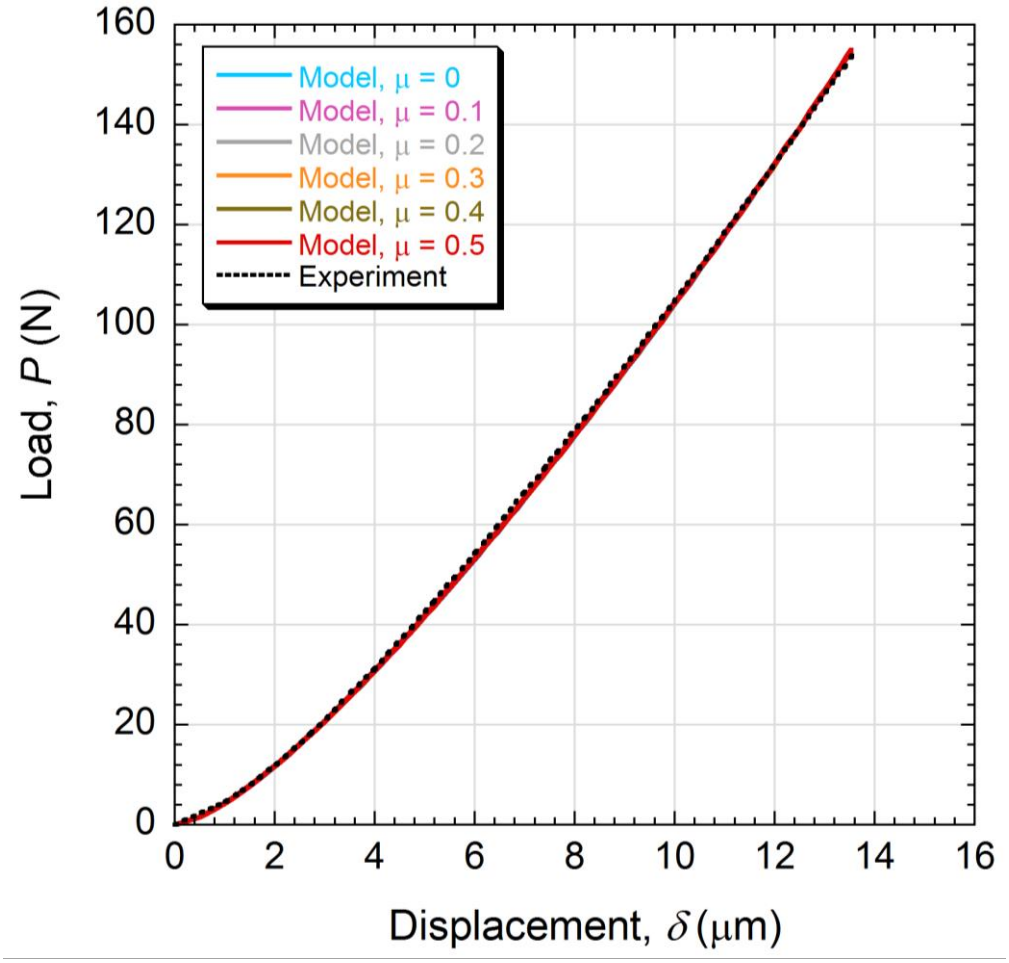

Figure 10.3. Comparison between experimental load-displacement plots and corresponding model predictions, obtained using the superelastic parameter values from Table 7.1 and the μ values shown in the legend.

As expected for this low penetration ratio (~0.70%), no differences were detected between load-displacement plots obtained from modelling of various friction coefficients, ranging from 0 to 0.5. In this regard, the value of μ adopted throughout this work was 0. This aided in reducing computational time.

It may also be noted that a new sample surface is created during indentation. Modelling experience [10, 11] showed that the predicted behaviour could be fairly sensitive to the value, particularly as the penetration ratio starts becoming relatively large (>10%), which is not the case of this present work, where penetration ratios (δ/R) tend to be lower than 1%. In practice, Campbell and co-authors found that best fit was usually achieved with a value of around 0.2-0.3, suggesting that this is typical of the effect of friction during experiments of this type. A similar value is expected here, but, as shown in Figure 10.3, it has no effect at such small δ/R values.

10.4. Sensitivities

A systematic parametric study has been carried out. Each parameter obtained from the experimental stress-strain curve (Table 6.1) was varied independently by a given factor, and then its effect on the modelled load-displacement plot was evaluated by comparing it with the experimental case (Figure 10.1). Each comparison generated a value of S_{red}. This is the simplest case, with just one parameter to evaluate, and hence the treatment is easy to follow. The comparisons can be seen in Figure 9.4.

The point at which the variation of parameters is zero is the point where the parameters are “correct” (e.g. parameters taken from the experimental stress-strain curve). For example, taking the experimental values of σ_{Ms} value to be 510 MPa (taken from Figure 8.8), and running the FEM model for a sphere, leads to a modelled load-displacement plot (assuming the other parameters remained constant). Comparing this plot with the experimental one leads to a value for S_{red} of ~5 x 10^{-3}. This is expected to be relatively high (i.e. poor agreement), in comparison with the S_{red} obtained for plasticity (of the order of ~10^{-4}), since the formulation adopted here does not represent well the material behaviour, as discussed previously. It is worth noting that, for an experimental plot as the “reference case”, S_{red} will never reach 0 for any trial value.

The elastic moduli of the phases are assumed to be known in the methodology implemented in this work. The exercise here is to investigate their influence on the load-displacement curve. From Figure 10.4(a), E_A has a strong influence on S_{red} values, especially when its trial value is higher than its experimental value. Modulus of martensite (E_M), on the other hand, only starts to make important changes on S_{red} when its trial value is higher than its experimental value by approximately 30%. Variations in S_{red} when E_M is lower than its experimental value tend to be very low (less than 0.5 x 10^{-3} for a parameter variation of 50%).

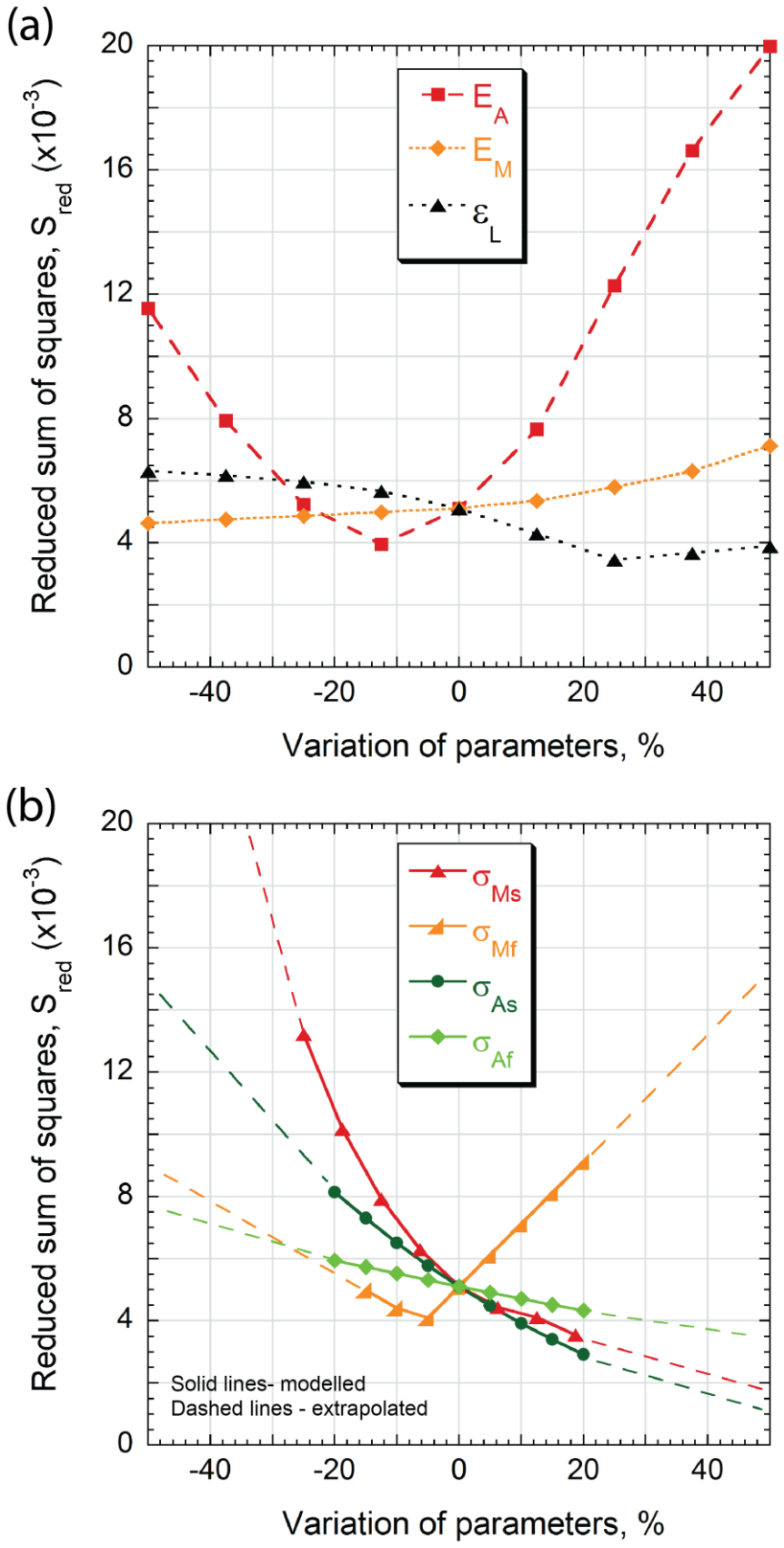

Figure 10.4. S_{red} as a function of the variation of parameters (trial values with respect to the experimental values taken from Figure 8.8), over a range either side of the experimental values, for a spherical indenter.

The transformation strain (ε_L) is an important parameter when defining the stress-strain curve. It defines the amount of recoverable deformation of the material. This parameter is included in the search algorithm. Figure 10.4(b) shows that S_{red} tends to be lower when the trial ε_L values increase. This has scope for "compensation", since the search algorithm was designed to minimise the S_{red} value.

Regarding the variation of transition stresses (Figure 10.4(b)), σ_{Mf} presents a minimal value of S_{red} when its trial value is slightly lower than its "correct" value (by approximately 5%), at which point S_{red} presents a linear increase on either side. The other stresses (σ_{Ms}, σ_{As} and σ_{Af}) tend to minimise S_{red} when moved towards high trial values. Again, this might generate some degree of compensation in this direction.

Although each parameter was independently varied, the overall outcome gives an indication of how these parameters might behave in the multiparameter space, where they will be moved towards minimising S_{red}.

10.5. Convergence Characteristics

The convergence operation was carried out using the averaged experimental load-displacement plot as a "target" (Figure 8.8). The outcome is shown in Figure 10.5. Successful convergence was achieved (after a relatively large number of iterations) and the resultant values of the SE parameter set are shown in this figure, presented in Table 10.1 and also plotted as a stress-strain curve in Figure 10.6.

It can immediately be seen that while the agreement is fairly good for the loading curve (except for the peak strain), it is deficient for the unloading curve. It seems clear that this is due to the poor fidelity between the actual unloading curves experienced by the various volume elements deformed during the indentation operation and the way that these are represented in the UMAT routine for their simulation. This is mainly associated with the poor agreement between experimental and modelled minor stress-strain loops (discussed in more detail in §8.7.2).

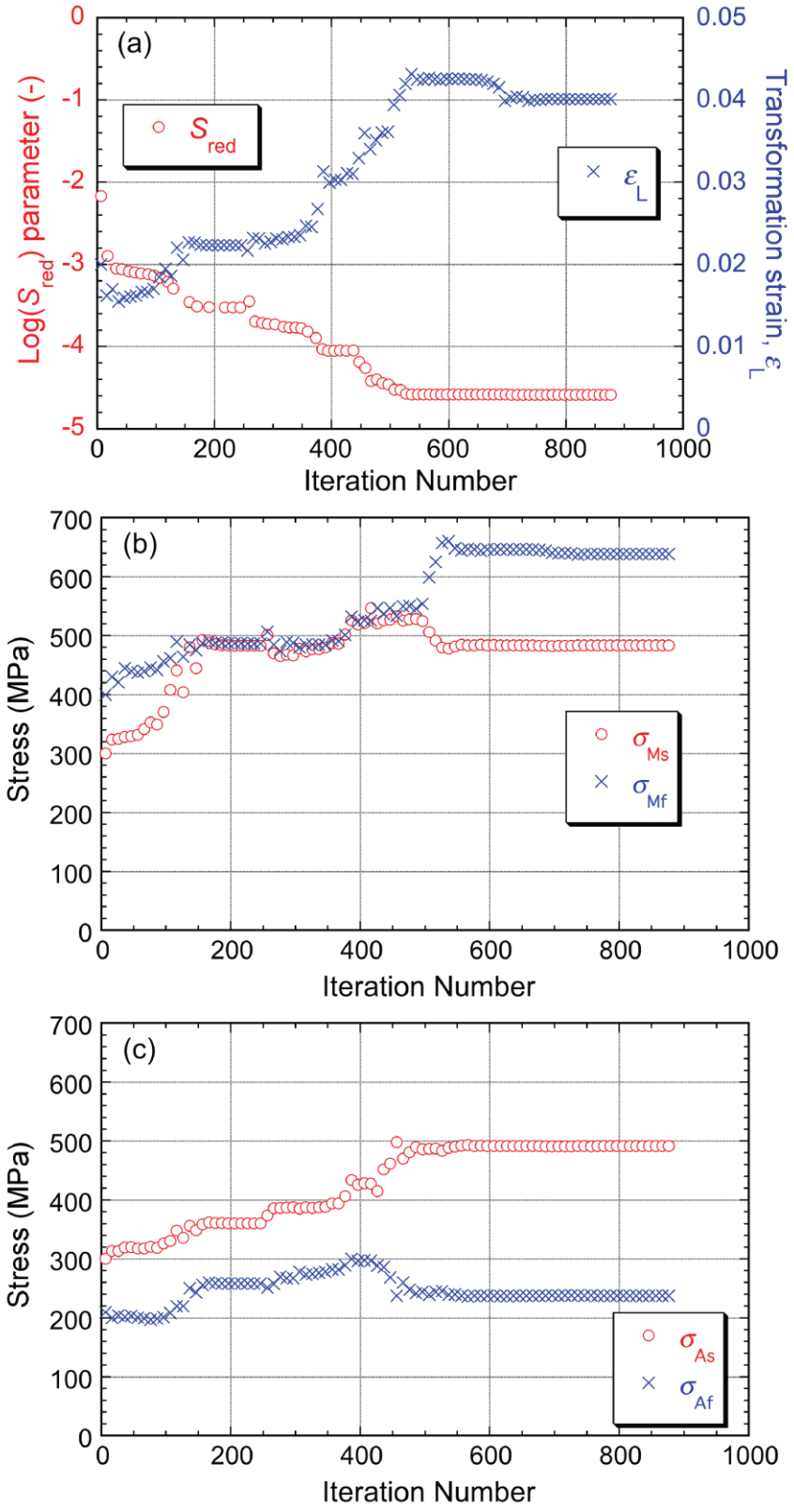

Figure 10.5. Nelder-Mead convergence on an optimal (UMAT) parameter set, targeting an indentation load-displacement plot, showing evolution with iteration number of (a) misfit parameter and transformation strain, (b) martensite start and finish stresses and (c) austenite start and finish stresses.

Parameter	Symbol	Direct fitting to uniaxial data	Inferred from indentation
Martensite start stress	σ_{Ms}	510 MPa	484 MPa
Martensite finish stress	σ_{Mf}	605 MPa	639 MPa
Transformation strain	ε_L	0.032	0.040
Austenite start stress	σ_{As}	310 MPa	491 MPa
Austenite finish stress	σ_{Af}	110 MPa	238 MPa

Table 10.1. Comparison between the SE parameter values obtained by direct fitting to the experimental stress-strain curve (Figure 8.8) and via iterative FEM using indentation data.

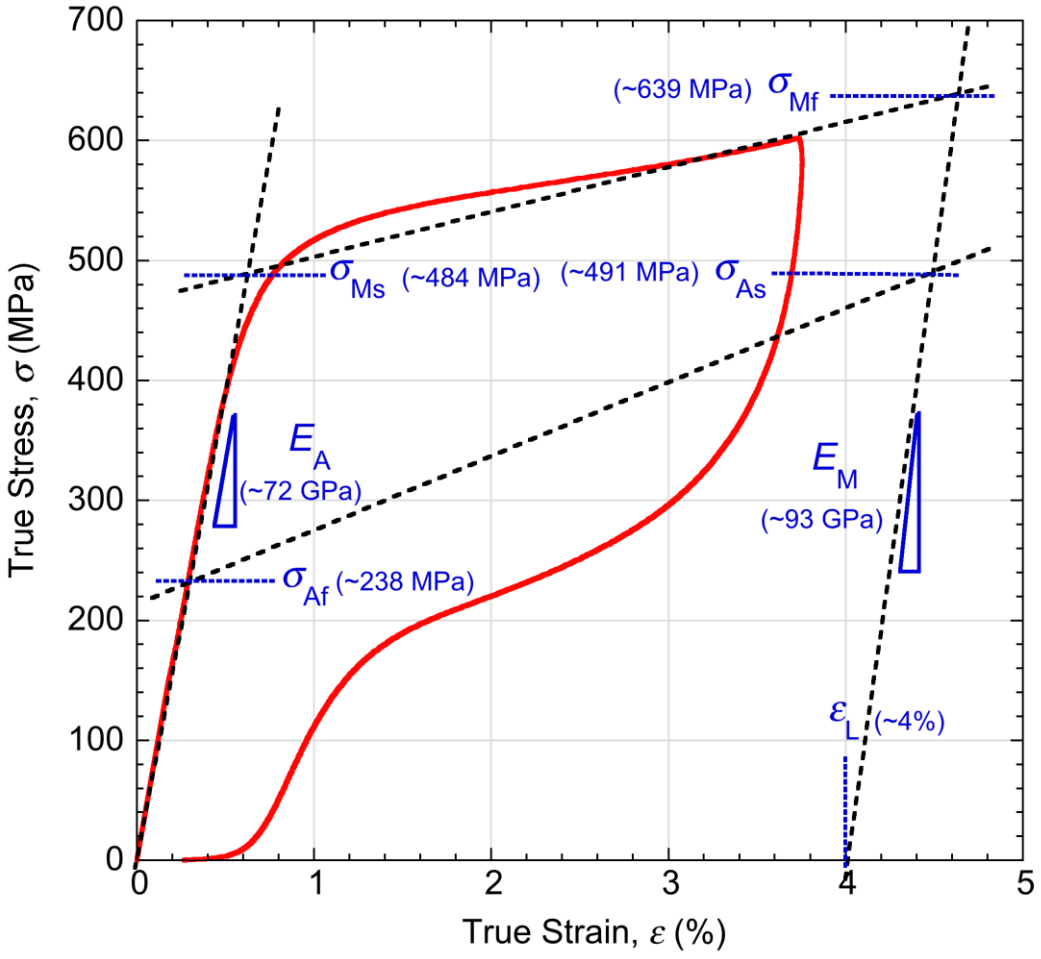

Figure 10.6. Comparison between the experimental stress-strain plot (also shown in Figure 8.8) and the SE parameter set inferred from the experimental indentation load-displacement plot (shown in Figure 10.1), via the Nelder-Mead convergence operation represented in Figure 10.5.

Furthermore, the nature of the discrepancy can be at least qualitatively understood. During unloading, at a given strain, the actual load carried by most individual volume elements is higher than that being simulated, at least until the strain becomes very small. When constrained by the UMAT representation, the convergence operation

leads to compensation for this by raising σ_{As} and σ_{Af}. Some of these "compensation effects" have been already predicted in the sensitivity analysis, where each parameter was varied independently. For example, ε_L, σ_{As} and σ_{Af} tended to increase their trial value towards minimising $S_{red.}$ In that sensitivity case (Figure 10.4), the σ_{Mf} presented an optimal region where S_{red} has a local minimum, which was not detected during the search of all 5 parameters. In fact, during the convergence, the algorithm also increased σ_{Mf} trail values in the direction where S_{red} will reach its minimum. It is important to highlight that the combination of all parameters can generate "plateau regions" in the parameter space, where S_{red} is uniformly low. The final load-displacement comparison is shown in Figure 10.7.

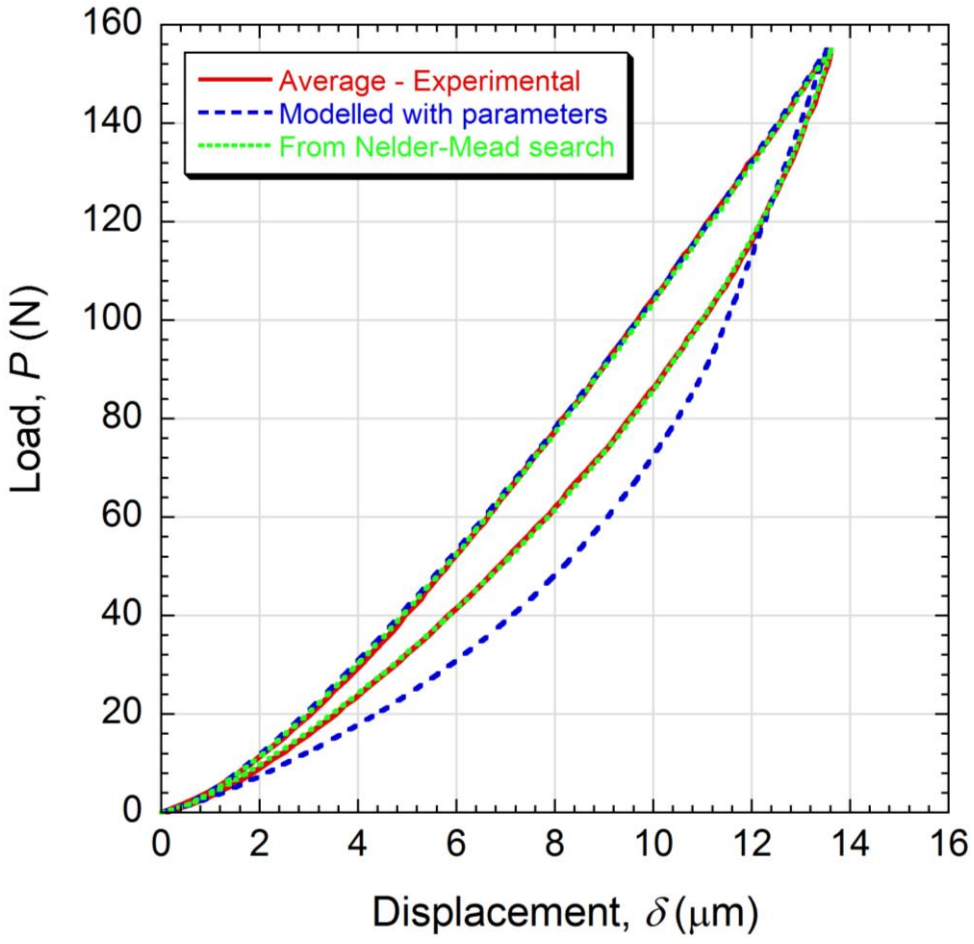

Figure 10.7. Comparison between the indentation load-displacement plots obtained experimentally, by FEM simulation (using the best-fit set of parameter values from the uniaxial stress-strain curve) and from the Nelder-Mead convergence operation.

It is clear that the algorithm found an optimal parameter combination (e.g. the one that minimised S_{red}, which was ~2.6 x 10^{-5}, indeed very low for this type of analysis). As discussed previously, S_{red} for modelled case (with the parameter set from the

experimental uniaxial stress-strain curve) is only ~5 x 10^{-3}, which causes the algorithm to move the parameters towards improving this misfit. In this context, the convergence operation has also been carried out on the stress-strain curve. The convergence characteristics are shown in Figure 10.8.

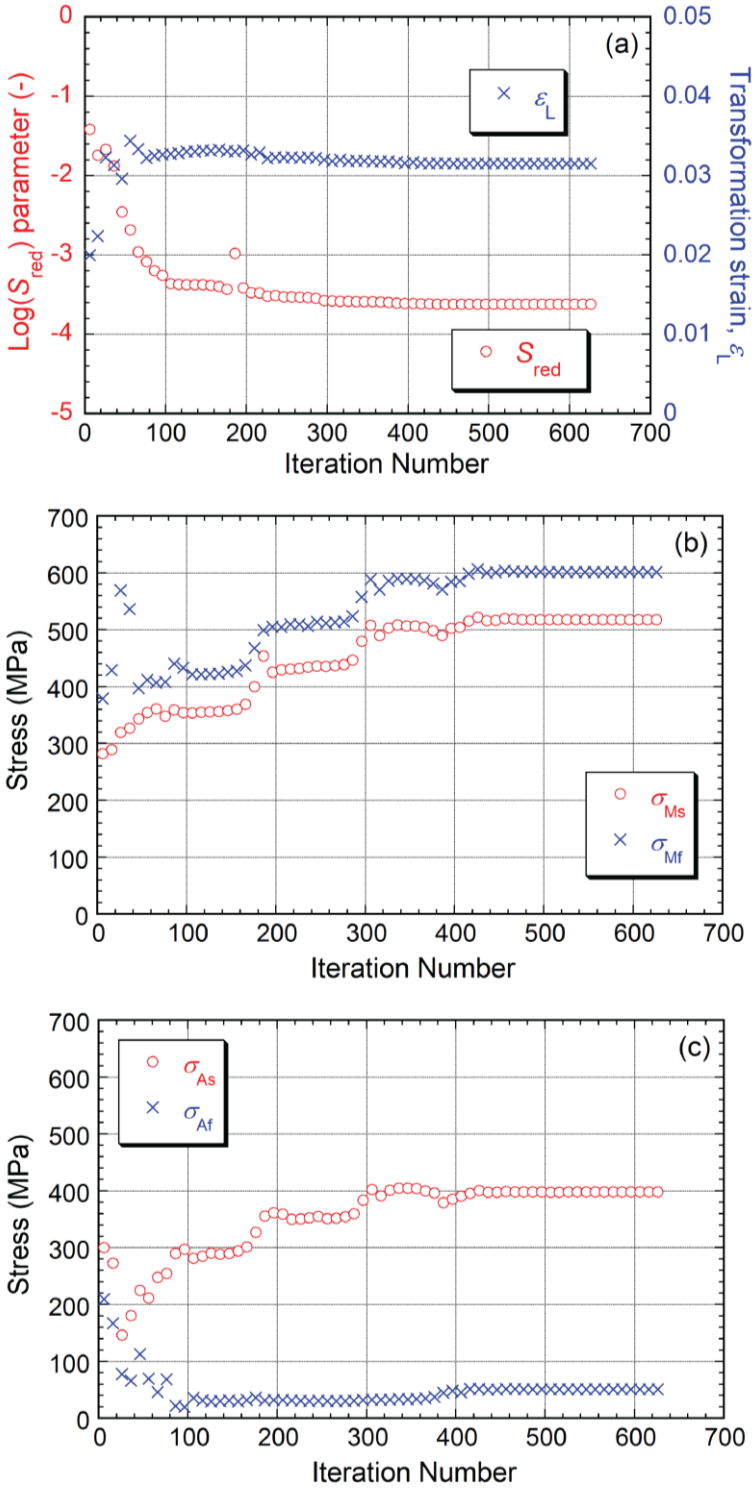

Figure 10.8. Nelder-Mead convergence on an optimal (UMAT) parameter set, targeting a stress-strain plot, showing the evolution with iteration number of: (a) misfit parameter and transformation strain, (b) martensite start and finish stresses and (c) austenite start and finish stresses.

This was a relatively fast and straightforward operation since it consisted of running a single-element model. The best-fit parameter values were found after approximately 400 iterations, despite having the initial guesses set relatively far away from the answer, as in the indentation case. The comparison between "optimal" and experimental stress-strain curves is shown in Figure 10.9. These values are not very different from the ones obtained "manually" from Figure 8.8.

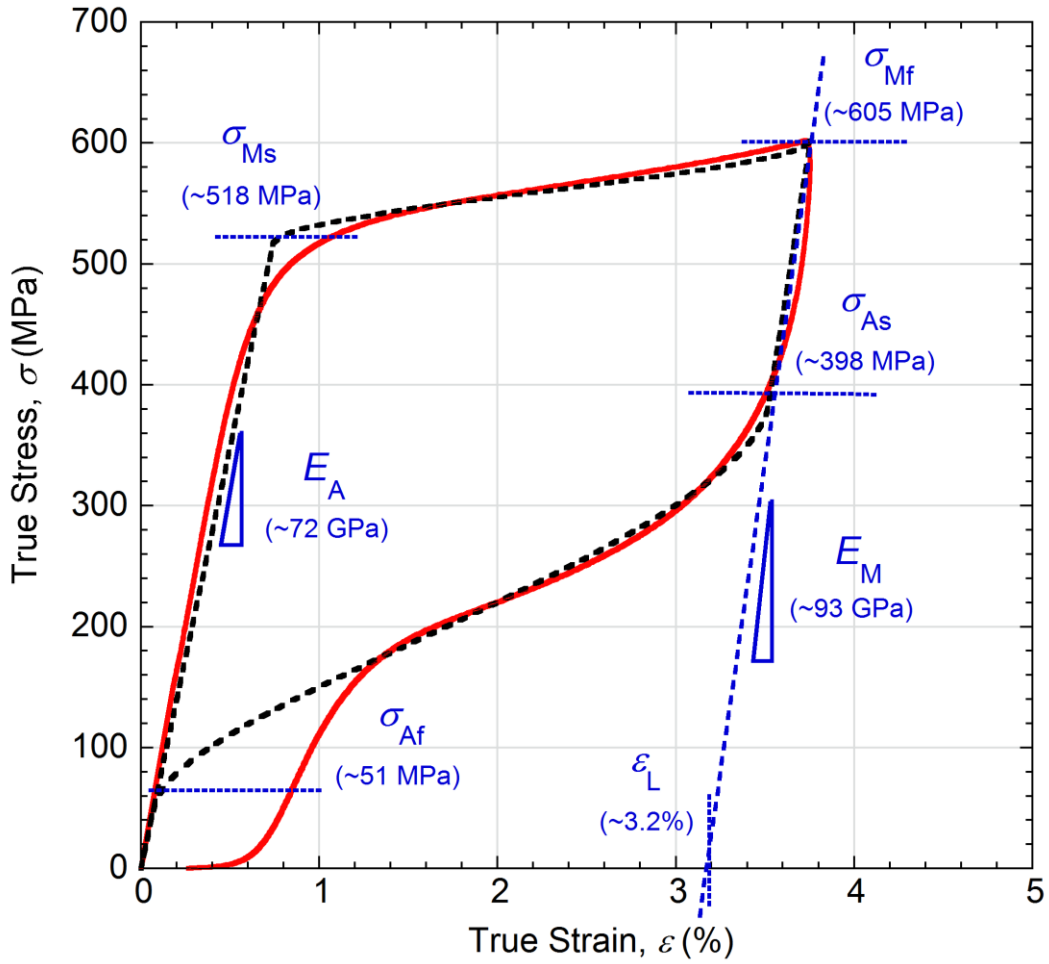

Figure 10.9. Comparison between the experimentally-obtained stress-strain plot (in red) and the modelled stress-strain (in black) obtained with the best-fit parameters (in blue) inferred from the convergence operation.

As presented previously, the modelled stress-strain curve is relatively well-captured by the search algorithm, apart from the final portion of the unloading part. The optimal S_{red} value obtained for this case was ~2.4 x 10^{-4}. This is not as high as the one obtained from the optimisation of the load-displacement case (S_{red} ~ 2.6 x 10^{-5}).

The misfit for the stress-strain case will increase when carrying out this operation on any minor superelastic loop, since these are poorly represented by the current

material formulation [63]. In this regard, given that the indentation case has most volume elements undergoing partial phase transformation, it is possible to say that its "best" S_{red} represents an amalgamation of effects (e.g. misfit of the major loops combined with misfit of the minor loops).

Overall, the computational operation is tractable for both cases (load-displacement and stress-strain curves). The procedure could, however, be facilitated if the "initial guesses" for the simplex were in an appropriate region of parameter space (i.e. if the initial trial values are fairly close to the best-solution set). Otherwise, the number of iterations for convergence may go up significantly.

As in the plasticity case, this operation is extremely dependent on the material formulation, meaning that the quality of the outcome of the convergence operation will be directly linked to the misfit between modelled and experimental stress-strain curves.

10.6. Improved Representation of the Unloading Curves

It seems clear that what is required here is a more realistic formulation for the unloading curves. From a mathematical point of view, this should not be a major challenge. For example, a "Dose-Response" expression (commonly used in biological investigations) of the following type (4-stage with zero background):

$$y = 1 - \exp(Ax + Bx^2 + Cx^3 + Dx^4) \qquad (10.1)$$

This can exhibit a similar shape to those of typical unloading curves. When the experimental unloading curves are normalised, they do not collapse accurately onto a single master curve, but they are not so far from doing this. This is illustrated by the plots shown in Figure 10.10, in which the unloading loops (from Figure 8.6) have been normalised and are compared with the curve obtained using Equation 10.1 with a particular set of coefficient values (shown in Figure 10.10).

The purpose here is simply to propose a function that could used to fit the unloading curves (or at least be better than the UMAT formulation) using a predetermined set of coefficient values in this way. Furthermore, since there seems to be a systematic trend, it may be possible to obtain a better fit.

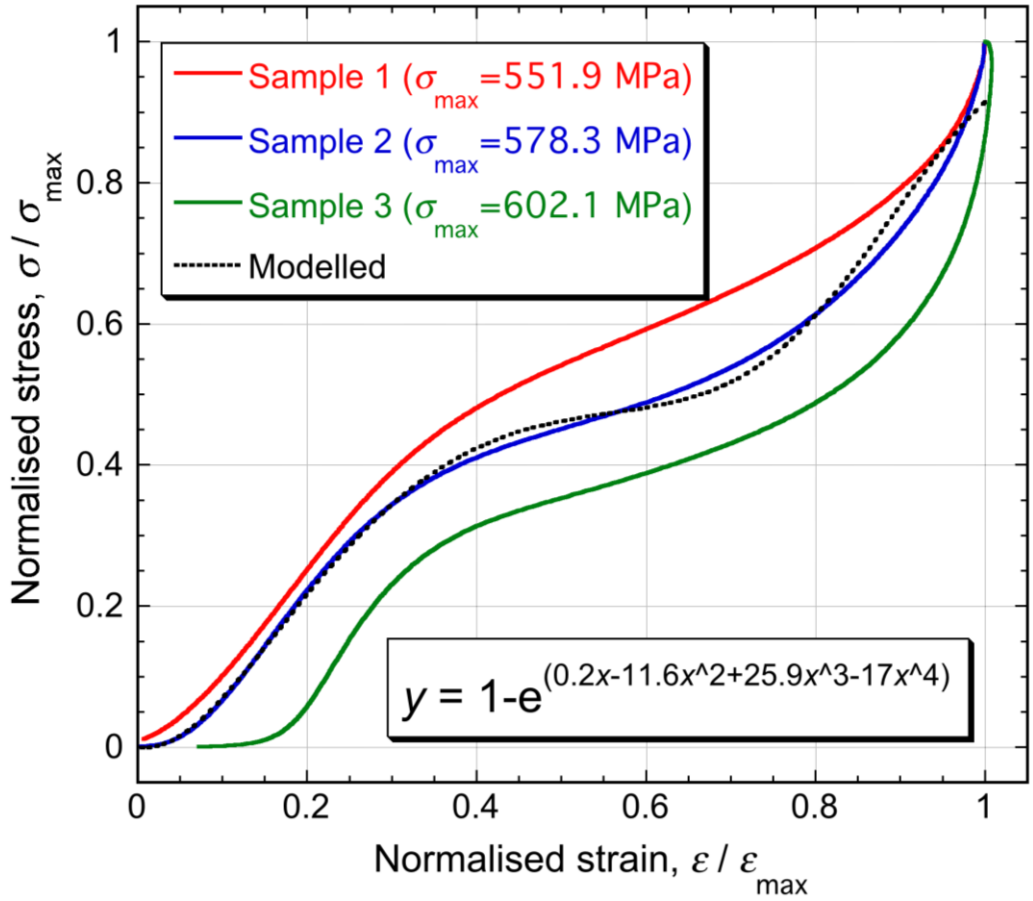

Figure 10.10. Unloading loops of the experimental stress-strain curves from Figure 8.6, in normalised form, together with an analytical equation that could be used to represent them.

The proposed operation would be a two-step procedure:

I. Modelling the loading part with the current formulation already implemented in ABAQUS [27, 63].

II. Identify the maximum stress (or strain) from step I, and then fit the unloading loop by using Equation 10.1: it is possible to establish an analytical relationship between the maximum load or strain (i.e. the fractional distance along the part of the loading curve where the phase transformation is occurring) and the values of the coefficients in Equation 10.1.

The step II consists of a systematic method of fitting load-displacement curves to experimental results. Thus, the Equation 10.1 could be implemented into an existing material formulation as a “flow rule” for the unloading parts (major and minor loops), such as the unified model proposed by Lagoudas et al. [71]. The next step would be to integrate this into a suitable FEM solver.

10.7. Summary

The following topics were learnt from this chapter:

- The level of agreement between experimental and modelled load-displacement curves is good for the loading curve, but poor for the unloading curve. This is expected since the fidelity of the ABAQUS UMAT to the actual stress-strain curve is quite poor towards the end of the unloading.

- The analysis of the strain and stress fields obtained via FE simulations showed that most of the volume elements that deform during indentation do not fully transform into martensite, and those will follow minor loops in the stress-strain curve.

- For the low penetration ratio of ~0.70%, used in this work, no differences were detected between load-displacement plots obtained from modelling of various friction coefficients, ranging from 0 to 0.5. In this regard, the value of μ adopted throughout this work was 0. This had an impact in the computational time.

- The sensitivity of each parameter was independently checked. The overall outcome gives an indication of how these parameters might behave in the multiparameter space, where they will be moved towards minimising S_{red}.

- The algorithm successfully converged in SE parameter values upon specified tolerance. These parameters were plotted against an experimental stress-strain curve. While the agreement is fairly good for the loading curve, it is deficient for the unloading curve. This is mainly associated with the poor agreement between experimental and modelled minor stress-strain loops.

- The convergence time largely depends on the “initial guesses” for the simplex. This will be facilitated if the initial trial values are fairly close to the best-solution set. Otherwise, the number of iterations for convergence may go up significantly.

- As presented previously, the modelled stress-strain curve is relatively well-captured by the search algorithm, apart from the final portion of the unloading part. The optimal S_{red} value obtained for this case was ~2.4 x 10^{-4}.

This is not as high as the one obtained from the optimisation of the load-displacement case (S_{red} ~ 2.6 x 10^{-5}), leaving considerable scope for "parameter compensation" towards minimising S_{red}.

- An improved representation of the unloading curve of the stress-strain curve is presented here. This would depend on the values of its coefficients as well as on the maximum stress, which could be obtained from the current ABAQUS UMAT. This function could be used as a "flow rule" for the unloading curve, but it would need to be implemented in ABAQUS (or another FEM package).

11. CONCLUSIONS AND FUTURE WORK

11.1. Conclusions

11.1.1. Issues Related to Experiments

- The requirement to use relatively large indenters and loads means that many small-scale (i.e. “nano-indenter”) systems are not well suited to this methodology. On the other hand, it also means that the experimental procedures are more straightforward, more transparent and less problematic than in many fine-scale systems. Surface preparation is straightforward − a standard polish to a roughness of a few microns is fine − and there will be few concerns about the effects of oxide layers or surface contamination. Furthermore, obtaining suitable indenters is relatively easy and cheap cermet spheres in this size range are readily obtainable. Displacement measurement must be accurate, although, again, the relatively coarse scale of the operation means that ultra-high precision is not needed and a standard eddy current gauge, LVDT should be adequate (or even the displacement taken from the rotation of a worm drive, with the appropriate compliance correction).

- Uniaxial compression and (spherical) indentation experiments have been carried out on a commercially-available NiTi alloy that exhibits superelastic behaviour at room temperature. A traceable and transparent method to determine compliance for both indentation and mechanical testing rigs has been successfully established.

11.1.2. Finite Element Models and Material Formulations

- The (major) uniaxial stress-strain loop is of the type expected, and it has been represented here via a set of parameter values that define a series of linear sections. Such a set of parameter values can be used within an ABAQUS FEM package (with the UMAT formulation). It is noted that this representation is not a very accurate one for the unloading part of the curve, particularly if the maximum strain experienced is significantly below that corresponding to the full transformation of the austenite into martensite.

- The friction coefficient during indentation is a parameter that does not need to be included in this optimisation, according to the FEM simulations. It is shown here that neglecting friction will not affect the outcome of the indentation response at the indentation ratio range over which the experiments were carried out.

- The sensitivity study has given an indication of how the parameters move in the multiaxial parameter space towards minimising the misfit value. That is important to understand the effects of parameter compensation.

11.1.3. Indentation Methodology for Extraction of SE Parameters

- The main objective of the work was to develop a methodology for obtaining the superelastic (stress-strain) characteristics solely from an indentation experiment. The approach used, which is already well-developed for plasticity, involved iterative FEM simulation of the indentation process, initially using trial values for the parameters involved in the constitutive law and converging on best-fit values by seeking to optimise the agreement between experimental and modelled outcomes (load-displacement plots in this case). This operation has been carried out and values obtained.

- The level of agreement between the experimental stress-strain plot and the one obtained via the indentation methodology is good for the loading part of the curve, but poor for the unloading part. This is attributed to limitations of the formulation for the unloading in the standard set of parameter values (in the UMAT routine available in ABAQUS).

- The current work has involved the study of experimental and some computational aspects of how the proposed methodology can be optimised (for superelasticity), as well as its limitations and sources of errors. It seems clear that, certainly in order for the indentation route to be viable, and perhaps more generally, an improved representation is required for the unloading part of superelastic stress-strain curves. An improved analytical formulation that could form the basis for this was suggested in this work.

11.2. Future Work

For future works, carrying on the line of research established during this thesis, the following could be suggested:

- Carry out indentation experiments on different types of superelastic NiTi alloys and then apply the FE-based methodology developed here to infer their properties.
- Investigate the residual strain left upon unloading of the major superelastic stress-strain loop.
- Develop a material formulation, based on the proposed function, capable of representing the minor stress-strain loops and use it to model indentation behaviour.
- Implement different approaches of search algorithms.
- Apply this methodology towards inferring properties of other materials with complex behaviour (multiple parameters required to infer the stress-strain curves).

12. APPENDICES

12.1. Considerations on Indentation and Hertzian Theory

12.1.1. Extraction of Young's Modulus from Indentation Data

The measurement of Young's modulus which, unlike hardness, requires continuous monitoring of load and displacement, is slightly more recent [81, 82]. Oliver and Pharr's method was developed to measure this material property from indentation data (P-δ) (see Figure 12.1(a)), obtained during one cycle of loading and unloading [81, 82].

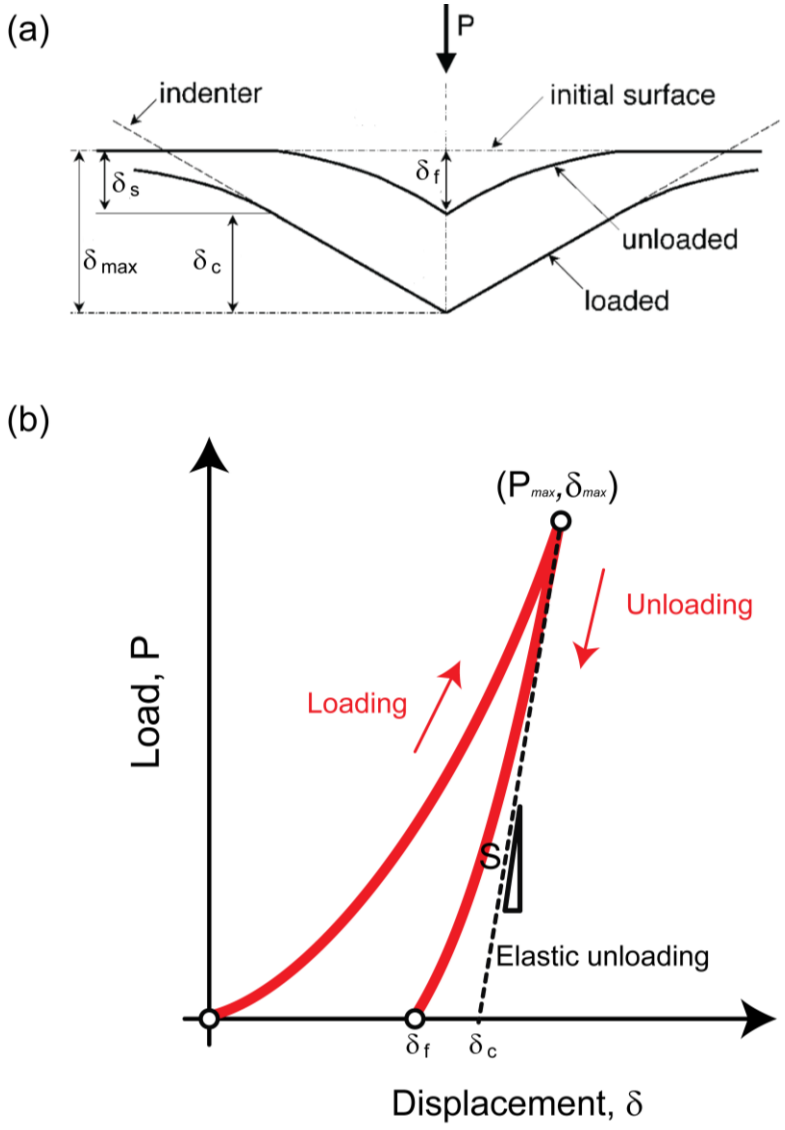

Figure 12.1. (a) Unloading process using a sharp indenter tip emphasising the geometric parameters and (b) Load-displacement curve, adapted from Oliver and Pharr [82].

Although this method was initially developed for sharp indenter tips, further researchers have proven that it can also be applied in any axisymmetric indenter geometry, including spheres [82]. A standard load-displacement curve obtained with Berkovich indenter is shown in Figure 12.1(b), where *P* is the indentation load and δ is the depth related to the initial undeformed surface. According to Oliver and Pharr [82], the deformation during unloading is considered to be both elastic and plastic in nature. The contact stiffness, *S*, is defined as the slope of the unloading curve at maximum indentation depth:

$$S = \frac{dP}{d\delta} \tag{12.1}$$

where *S* can be determined from a linear fit of the initial portion of the unloading curve.

Thus, assuming that the initial part of the unloading curve is almost entirely elastic recovery [81, 82, 142], the reduced modulus, E_r, is given by:

$$E_r = \frac{\sqrt{\pi}}{2\beta}\frac{S}{\sqrt{A_c}} \tag{12.2}$$

where A_c is the contact area (the contact area depends on the indenter shape and varies as a function of the penetration depth, δ) and β is a dimensionless correction factor which takes into account the deviation of stiffness due to the lack of asymmetry of the indenter tip. According to Kan et al. [122], β = 1, for [99] axisymmetric indenters, β = 1.012 for a square-based Vickers indenter, and β = 1.034 for a triangular Berkovich punch.

While the indenters are usually made of hard material (such as diamond or sapphire), they are not perfectly rigid. The reduced Young's modulus referred to above is designed to take account of the (non-zero) compliance of the indenter. The effective Young's modulus of the specimen (E_{eff}) can be calculated from E_r, including the effect of non-rigid tips, by:

$$E_{eff} = \frac{1-\nu^2}{\frac{1}{E_r} - \frac{1-\nu_i^2}{E_i}} \tag{12.3}$$

where ν_i and E_i are the elastic properties of the indenter.

The accuracy of the values of E inferred from indentation data modulus will strongly depend on the precision of the experimental set-up.

12.1.2. Hertzian Contact Theory for Spherical Indentation

The Hertzian theory of contact between elastic bodies can be used to find contact areas and indentation depths for simple geometries.

The method developed by Oliver and Pharr, previously discussed, is recognised to be a very accurate analysis for indentation with a sharp Berkovich or conical indenter not having, on the other hand, the same accuracy for determining hardness and modulus from spherical indentation. In that regard, some modifications based on the contact analysis should be applied. Consider that an elastic sphere of radius (R) indents an elastic half-space to depth, δ, and thus creates a contact area of radius, a_c, considering “sink-in” behaviour is given by:

$$a_c = \sqrt{R\delta} \tag{12.4}$$

According to Hertzian theory [143-147], assuming frictionless contact mechanics, the load-depth relationship is given by:

$$P = \frac{4}{3} E_{eff} R^{1/2} \delta^{3/2} \tag{12.5}$$

where E_{eff} is the effective modulus.

12.2. Code for the Extraction of Material Parameters

Code for searching material parameters, including the Nelder-Mead search method: “optimise_superelasticity_scipy_load_unload.py”

```
# coding: utf-8
# In[5]:
from __future__ import division, print_function, with_statement
import subprocess
import numpy as np
from scipy import optimize
import os
import glob
import math
import time


# In[4]:

def simulate_plasticity(epsilon, sigmaMS, sigmaMF, sigmaAS, sigmaAF, load):
    job_name = '{:3g}
ID{:g}_EP{:4g}_sMS{:4g}_sMF{:4g}_sAS{:4g}_sAF{:4g}'.format(load,
np.random.randint(99999), epsilon, sigmaMS, sigmaMF, sigmaAS, sigmaAF)

    job_name = job_name.replace('.', '-')
    job_name = job_name.replace(' ', '')

    parameter_file_text = ('\n' +
   'import numpy as np\n' +
   'epsilon={}\n'.format(epsilon) +
   'sigmaMS={}\n'.format(sigmaMS) +
   'sigmaMF={}\n'.format(sigmaMF) +
   'sigmaAS={}\n'.format(sigmaAS) +
   'sigmaAF={}\n'.format(sigmaAF) +
   'load={}\n'.format(load) +
   'job_name="' + job_name + '"\n')


    with open('job_params.py', 'wt') as file:
        file.write(parameter_file_text)

    # Grab the input file template and find the line number of the
superelastic parameters
    template = []
    with open('./template.inp', 'r') as template_file:
        for line in template_file:
            template.append(line)

    with open('./template.inp', 'r') as template_file:
        for index, line in enumerate(template_file):
            if '*User Material, constants=15' in line:
                line_number = index + 1
                break


    # replace the right line with the new superelastic parameters:
    template[line_number] = '72000.,  0.33, 93000.,  0.33,  {:},    7.,
{:},  {:}\n'.format(epsilon, sigmaMS, sigmaMF)
```

```
    template[line_number+1] = '   20.,    7.,  {:},  {:},  {:},  {:},
0.\n'.format(sigmaAS, sigmaAF, sigmaMS, epsilon)

    # write this to a file:
    with open('./'+job_name + '.inp', 'w') as file:
        file.writelines(template)
    try:
        subprocess.run(['abaqus', 'job=' + job_name + '.inp', 'cpus=4',
'mp_mode=threads', 'interactive'], shell=True)
    except:
    pass

# shell=True
# wait for data to be written (seemed to not be finding the file so trying
this)
    time.sleep(5)
    try:
        subprocess.run(['abaqus', 'python', 'extract_data.py'], shell=True)
    except:
        pass
    print('waiting')
    time.sleep(10)

    data = np.genfromtxt('./results/' + job_name + '.csv', delimiter=',')

    return data

def calc_g(exp, data):
    top = np.sum((exp - data) **2)
    average = np.mean(exp)
    bottom = np.sum((data - average)**2)

    if bottom > 1E-6:
        g =1-((top)/(bottom))**(0.5)
    else:
        g = 2
    return g

def calc_combined_g(material_variables, loads):

epsilon = material_variables[0]
sigmaMS = material_variables[1]
sigmaMF = material_variables[2]
sigmaAS = material_variables[3]
sigmaAF = material_variables[4]

g_values = np.ones_like(loads)
#loads=parameters['loads']

for i,load in enumerate(loads):
modelled_disp = simulate_plasticity(epsilon, sigmaMS, sigmaMF, sigmaAS,
sigmaAF, load)[:,1][0:200]
np.savetxt('./results/Cutdata' + job_name + '.csv', modelled_disp,
delimiter=',')
experimental_filename = str(int(load)) + '.csv'
expCsv = np.genfromtxt(experimental_filename, delimiter=",")
exp_disp = expCsv[:,1][0:200]
current_g = calc_g(exp_disp, modelled_disp)

g_values[i] = current_g
g = np.amax(g_values)
```

```
print(len(modelled_disp))
hist_file = open('./results/history.txt', 'at')
    # save g, yield stress, K, n
hist_file.write('{},{},{},{},{},{},\n'.format(g, *material_variables))
hist_file.close()
return g


def calc_scaled_sum_of_squares(exp, data):
    '''Calculate the sum of squares of the residuals between some
       experimental data and some data that has been generated to fit
it.'''
    residuals_squared = ((exp - data) / np.max(exp)) ** 2
    scaled_sum_of_squares = residuals_squared.sum()
    return scaled_sum_of_squares


def calc_combined_sum_of_squares(material_variables, loads):

epsilon = material_variables[0]
sigmaMS = material_variables[1]
sigmaMF = material_variables[2]
sigmaAS = material_variables[3]
sigmaAF = material_variables[4]

sum_of_squares = 0
g_values = np.zeros_like(loads)
    #loads=parameters['loads']

for i, load in enumerate(loads):

modelled_disp = simulate_plasticity(epsilon, sigmaMS, sigmaMF, sigmaAS,
sigmaAF, load)[:,1][0:200]
experimental_filename = str(int(load)) + '.csv'
expCsv = np.genfromtxt(experimental_filename, delimiter=",")
exp_disp = expCsv[:,1][0:200]

if len(modelled_disp) != len(exp_disp):
modelled_disp = np.zeros_like(exp_disp)

        ## I've made the assumption that there are the sma e number of data
points
        # at every load. If not a correction needs to be made here.

sum_of_squares += calc_scaled_sum_of_squares(exp_disp, modelled_disp)
g_values[i] = calc_g(exp_disp, modelled_disp)

ghist_file = open('./results/g-history.txt', 'at')
    # save g  average, epsilon, sigmaMS, sigmaMF, sigmaAS, sigmaAF
ghist_file.write('{},{},{},{},{},{},\n'.format(np.mean(g_values),
*material_variables))
ghist_file.close()

hist_file = open('./results/history.txt', 'at')
    # save sum of squares, epsilon, sigmaMS, sigmaMF, sigmaAS, sigmaAF
hist_file.write('{},{},{},{},{},{},\n'.format(sum_of_squares,
*material_variables))
hist_file.close()

return sum_of_squares
```

```
try:
    os.mkdir('./results/')
except:
    pass
try:
    os.mkdir('./temp/')
except:
    pass

# Initial guess at creep parameters
epsilon = 0.02
sigmaMS = 300
sigmaMF = 400
sigmaAS = 300
sigmaAF = 200

material_variables = np.array([epsilon, sigmaMS, sigmaMF, sigmaAS,
sigmaAF])


hist_file = open('./results/history.txt', 'wt')
hist_file.write('g value, epsilon, sigmaMS, sigmaMF, sigmaAS, sigmaAF\n')
hist_file.close()

# extract fixed parameters from data files with names of the form
"load.csv" where load is in Newtons
names = [os.path.basename(x) for x in glob.glob("*.csv")]
loads = [float(name.split('.')[0]) for name in names]
optimisation_result = optimize.fmin(calc_combined_sum_of_squares,
material_variables, args=(loads,), xtol=0.0001)
optimised_material_properties = optimisation_result.x
best_g = optimisation_result.fun

np.savetxt('./results/optimised_material_properties.csv',
np.array([optimised_material_properties]), delimiter=',')
```

Code for extracting data from ".ODB" files (must be in the same folder as in the previous file): "extract_data.py"

```
import odbAccess
import numpy as np
import job_params

def extract_odb(path_to_odb):
    stepName = 'Loading Step'
    historyRegionName = 'Node Load Application Part-1.1'
    historyOutputName = 'U2'

    # open odb file
    ODBFile = odbAccess.openOdb(path = path_to_odb)

    #
    # assign step object
    # print ODBFile.steps.keys()
    step = ODBFile.steps[stepName]
    #
    # assign historyRegion object
    # print step.historyRegions.keys()
    historyRegion = step.historyRegions[historyRegionName]
    #
    # assign historyOutput object
    # print historyRegion.historyOutputs.keys()
    data = np.array(historyRegion.historyOutputs[historyOutputName].data)

    data[:,1] = (data[0,1] - data[:,1]) * 1000

    return data

data = extract_odb('./'+job_params.job_name+'.odb')
   np.savetxt('./results/'    +    job_params.job_name    +    '.csv',    data,
delimiter=',')
```

12.3. Stress-Strain Curves

The data presented in Figure 12.2 is a comparison between stress-strain curves obtained from two different strain-measurement techniques: strain gauges and eddy current sensor (transducer).

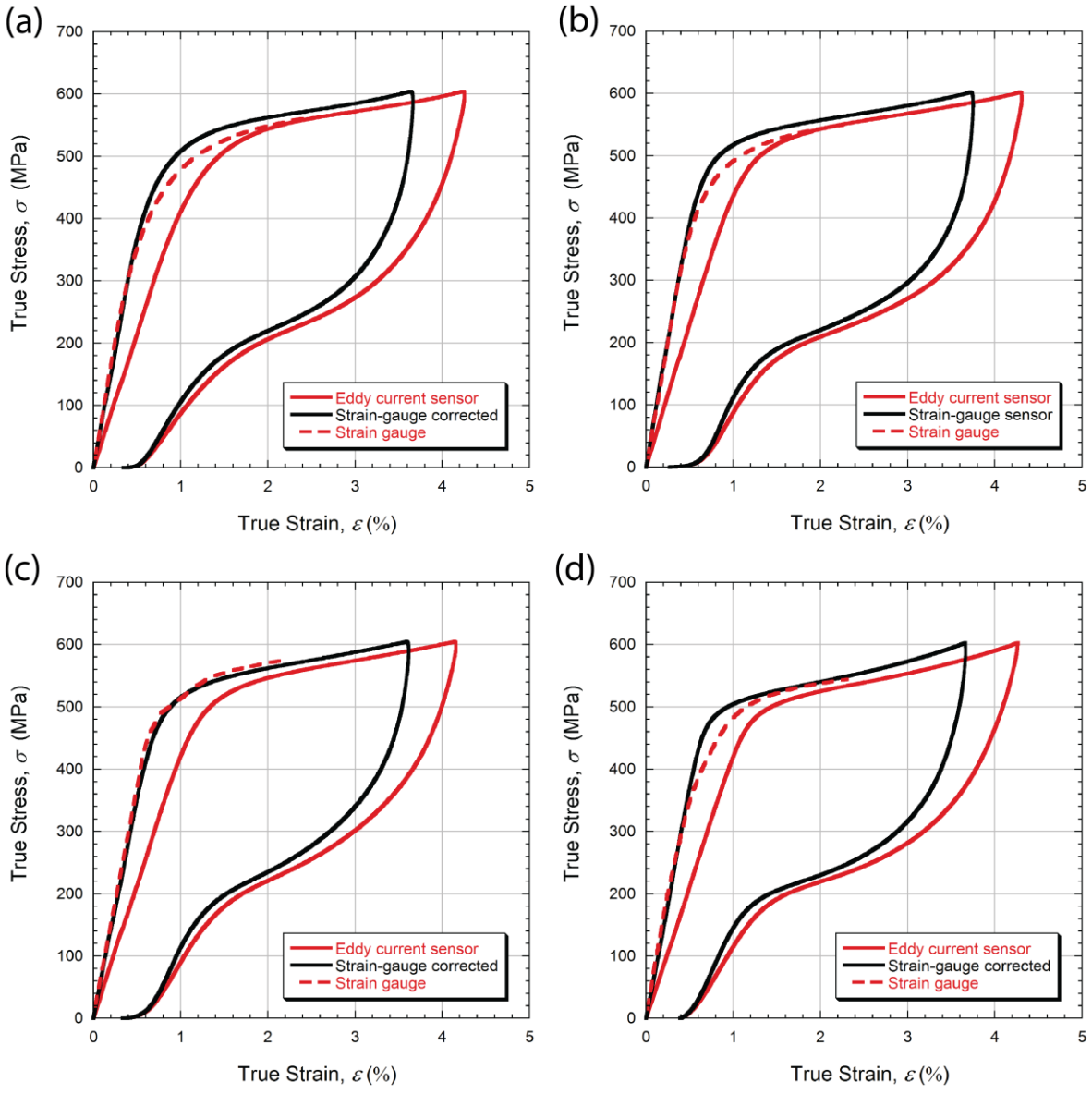

Figure 12.2. Comparison between a corrected stress-strain curve the ones obtained simultaneously via strain gauge and eddy current sensor: (a) and (c) specimens tested in the axial direction; (b) and (d) specimens tested in the radial direction.

12.4. Loading Rate Analysis

Load-displacement plots obtained at different loading rates are presented in Figure 12.3. Five indents were made at each rate.

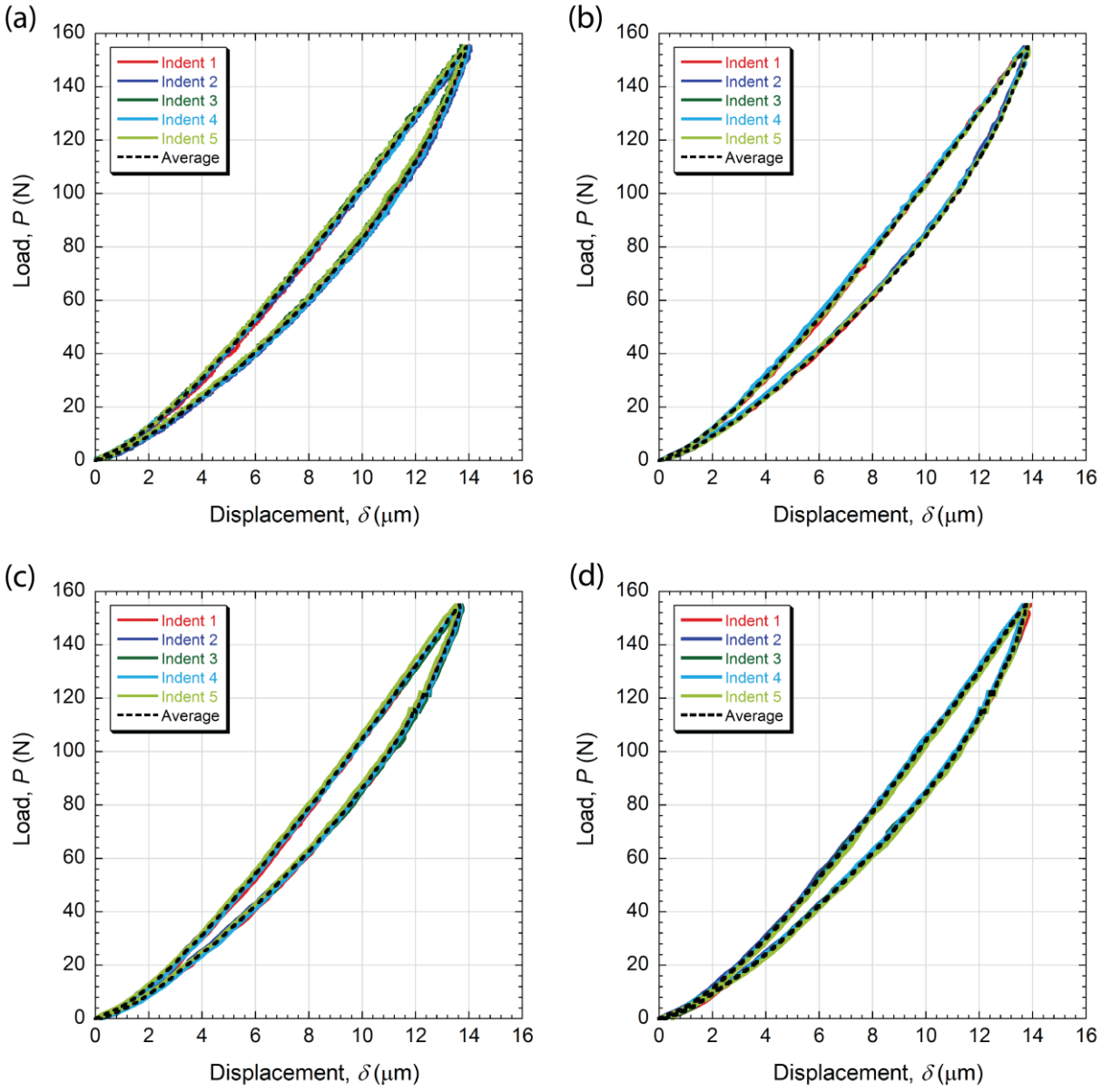

Figure 12.3. Load-displacement plots obtained at different loading rates at a maximum load of 155 N: (a) 0.25 μm/s, (b) 0.50 μm/s, (c) 1.00 μm/s and (d) 2.00 μm/s.

13. REFERENCES

1. Saburi, T., *Ti-Ni shape memory alloys*, in *Shape memory materials*, K. Otsuka and C.M. Wayman, Editors. 1998, CUP: Cambridge. p. 49-96.
2. Van Humbeeck, J. and R. Stalmans, *Shape memory alloys, types and functionalities*, in *Encyclopaedia of SMART MATERIALS*, M. Schwartz, Editor. 2002, John Wiley and Sons, Inc. p. 951-964.
3. Van Humbeeck, J., *The martensitic transformation*, in *Mechanical Spectroscopy*, R. Shaller, G. Fantozzi, and G. Gremaud, Editors. 2001, Trans Tech Publications. p. 382-415.
4. Otsuka, K. and X. Ren, *Physical metallurgy of Ti–Ni-based shape memory alloys.* Progress in Materials Science, 2005. **50**(5): p. 511-678.
5. Šittner, P., et al., *Young's Modulus of Austenite and Martensite Phases in Superelastic NiTi Wires.* Journal of Materials Engineering and Performance, 2014. **23**(7): p. 2303-2314.
6. Guelorget, B., et al., *Extracting the Plastic Properties of Metal Materials from Microindentation tests: Experimental Comparison of Recently Published Methods.* J. Mater. Res., 2007. **22**: p. 1512-1519.
7. Dean, J., J.M. Wheeler, and T.W. Clyne, *Use of Quasi-Static Nanoindentation Data to Obtain Stress-Strain Characteristics for Metallic Materials.* Acta Materialia, 2010. **58**: p. 3613-3623.
8. Patel, D.K. and S.R. Kalidindi, *Correlation of spherical nanoindentation stress-strain curves to simple compression stress-strain curves for elastic-plastic isotropic materials using finite element models.* Acta Materialia, 2016. **112**: p. 295-302.
9. Dean, J. and T.W. Clyne, *Extraction of Plasticity Parameters from a Single Test using a Spherical Indenter and FEM Modelling.* Mechanics of Materials, 2017. **105**: p. 112-122.
10. Campbell, J.E., et al., *Mechanical properties of sprayed overlayers on superalloy substrates, obtained via indentation testing.* Acta Materialia, 2018. **154**: p. 237-245.
11. Campbell, J.E., et al., *Experimental and Computational Issues for Automated Extraction of Plasticity Parameters from Spherical Indentation.* Mechanics of Materials, 2018. **124**: p. 118-131.
12. Goodall, R. and T.W. Clyne, *A Critical Appraisal of the Extraction of Creep Parameters from Nanoindentation Data obtained at Room Temperature.* Acta Materialia, 2006. **54**(20): p. 5489-5499.
13. Dean, J., et al., *A Critical Assessment of the "Stable Indenter Velocity" Method for Obtaining the Creep Stress Exponent from Indentation Data.* Acta Materialia, 2014. **80**: p. 56-66.
14. Entemeyer, D., et al., *Strain Rate Sensitivity in Superelasticity.* International Journal of Plasticity, 2006. **16**: p. 1269-1288.
15. Muir Wood, A.J. and T.W. Clyne, *Measurement and Modelling of the Nanoindentation Response of Shape Memory Alloys.* Acta Materialia, 2006. **54**(20): p. 5607-5615.
16. Yan, W., et al., *Analysis of spherical indentation of superelastic shape memory alloys.* International Journal of Solids and Structures, 2007. **44**(1): p. 1-17.

17. Muir Wood, A.J., et al., *Nanoindentation of Binary and Ternary Ni–Ti-based Shape Memory Alloy Thin Film.* Surface & Coatings Technology, 2008. **202**: p. 3115-3120.
18. Farhat, Z., G. Jarjoura, and M. Shahirnia, *Dent Resistance and Effect of Indentation Loading Rate on Superelastic TiNi Alloy.* Metallurgical and Materials Transactions a-Physical Metallurgy and Materials Science, 2013. **44A**(8): p. 3544-3551.
19. Neupane, R. and Z. Farhat, *Prediction of Indentation Behavior of Superelastic TiNi.* Metallurgical and Materials Transactions a-Physical Metallurgy and Materials Science, 2014. **45A**(10): p. 4350-4360.
20. Sgambitterra, E., C. Maletta, and F. Furgiuele, *Temperature dependent local phase transformation in shape memory alloys by nanoindentation.* Scripta Materialia, 2015. **101**: p. 64-67.
21. Sun, Y., G. Zhao, and F. Yang, *Effect of electric current on nanoindentation of superelastic NiTi alloy.* Experimental Mechanics, 2015. **55**(8): p. 1503-1509.
22. Li, P., H.E. Karaca, and Y.-T. Cheng, *Spherical indentation of NiTi-based shape memory alloys.* Journal of Alloys and Compounds, 2015. **651**: p. 724-730.
23. Wang, L.Q., et al., *Superelasticity of NiTi-Nb metallurgical bonding via nanoindentation observation.* Materials Letters, 2015. **161**: p. 255-258.
24. Frost, M., et al., *Characterization of Superelastic NiTi Alloys by Nanoindentation: Experiments and Simulations.* Acta Physica Polonica A, 2015. **128**(4): p. 664-669.
25. Perlovich, Y., et al., *Accessing mechanical properties of superelastic materials from microindentation data by computer modelling*. 2016: Proceedings of 2016 6th International Workshop on Computer Science and Engineering.
26. Kabla, M. and D. Shilo, *Characterization of NiTi superelastic properties by nano-dynamic modulus analysis and nanoindentation.* Functional Materials Letters, 2017. **10**(2).
27. Auricchio, F. and R.L. Taylor, *Shape-memory alloys: modelling and numerical simulations of the finite-strain superelastic behavior.* Computer Methods in Applied Mechanics and Engineering, 1997. **143**: p. 175-194.
28. Zhang, Y., Y.-T. Cheng, and D.S. Grummon, *Finite element modeling of indentation-induced superelastic effect using a three-dimensional constitutive model for shape memory materials with plasticity.* Journal of Applied Physics, 2007. **101**(5): p. 053507.
29. Hosford, W.F., *Mechanical Behavior of Materials*. 2005: Cambridge University Press.
30. Tsuchiya, K., *1 - Mechanisms and properties of shape memory effect and superelasticity in alloys and other materials: a practical guide*, in *Shape Memory and Superelastic Alloys*. 2011, Woodhead Publishing. p. 3-14.
31. Christian, J.W. *Martensitic Transformations: A Current Assessment*. in *The Mechanism of Phase Transformation in Crystalline Solids*. 1968. Manchester: I.O.M.
32. Christian, J., G. Olson, and M. Cohen, *Classification of Displacive Transformations : What is a Martensitic Transformation ?* Journal de Physique IV Colloque, 1995. **05**(C8): p. C8-3-C8-10.
33. Otsuka, K. and X. Ren, *Recent developments in the research of shape memory alloys.* Intermetallics, 1999. **7**(5): p. 511-528.
34. Otsuka, K. and C.M. Wayman, *Shape Memory Materials*. 1998: Cambridge University Press. 284.

35. Otsuka, K. and C.M. Wayman, *Mechanism of shape memory effect and superelasticity*, in *Shape Memory Materials*, K. Otsuka and C.M. Wayman, Editors. 1998, CUP: Cambridge. p. 27-48.
36. Van Humbeeck, J. and R. Stalmans, *Characteristics of shape memory alloys*, in *Shape Memory Materials*, K. Otsuka and C.M. Wayman, Editors. 1998, CUP: Cambridge. p. 149-183.
37. Miyazaki, S. and H.Y. Kim, *2 - Basic characteristics of titanium–nickel (Ti–Ni)-based and titanium–niobium (Ti–Nb)-based alloys*, in *Shape Memory and Superelastic Alloys*. 2011, Woodhead Publishing. p. 15-42.
38. Antonucci, V. and A. Martone, *Chapter 2 - Phenomenology of Shape Memory Alloys*, in *Shape Memory Alloy Engineering*, L.L. Concilio, Editor. 2015, Butterworth-Heinemann: Boston. p. 33-56.
39. Pelton, A.R., S.M. Russell, and J. DiCello, *The Physical Metallurgy of Nitinol for Medical Applications.* Journal of Materials, 2003. **55**: p. 33-37.
40. Van Humbeeck, J., *Shape Memory Alloys: A Material and a Technology.* Advanced Engineering Materials, 2001. **3**: p. 837-850.
41. Hartl, D.J., et al., *Use of a Ni60Ti shape memory alloy for active jet engine chevron application: I. Thermomechanical characterization.* Smart Materials and Structures, 2010. **19**(1): p. 015020.
42. Fu, Y., et al., *TiNi-based Thin Films in MEMS Applications: a Review.* Sensors & Actuators A: Physical, 2004. **112**: p. 395-408.
43. Kelly, A. and K.M. Knowles, *Crystallography and Crystal Defects, 2nd Edition*. Crystallography and Crystal Defects, 2nd Edition. 2012, Oxford: Blackwell Science Publ. 1-521.
44. Hu, L., et al., *Transformation twinning and deformation twinning of NiTi shape memory alloy.* Materials Science and Engineering: A, 2016. **660**: p. 1-10.
45. Jani, J.M., et al., *A review of shape memory alloy research, applications and opportunities.* Materials & Design, 2014. **56**: p. 1078-1113.
46. Van Humbeeck, J., R. Stalmans, and P.A. Besselink, *Shape memory alloys*, in *Metals as Biomaterials*, J.A. Helsen and H.J. Breme, Editors. 1998, John Wiley & Sons. p. 73-100.
47. Duerig, T.W., A.R. Pelton, and D. Stöckel, *An overview of nitinol medical applications.* Materials Science and Engineering, 1999. **A273-275**: p. 149-160.
48. Zhang, X. and H. Sehitoglu, *Crystallography of the B2 → R → B19' phase transformations in NiTi.* Materials Science and Engineering: A, 2004. **374**(1): p. 292-302.
49. Sittner, P., et al., *On the R-phase transformation related phenomena in NiTi polycrsytals subjected to thermomechanical loads.* Journal de Physique IV France, 2004. **115**: p. 269-278.
50. Uchil, J., K. Ganesh Kumara, and K.K. Mahesh, *Effect of thermal cycling on R-phase stability in a NiTi shape memory alloy.* Materials Science and Engineering: A: Structural Materials: Properties, Microstructure and Processing, 2002. **332**: p. 25-28.
51. Knowles, K.M. and D.A. Smith, *The crystallography of the martensitic transformation in equiatomic nickel-titanium.* Acta Metallurgica, 1981. **29**: p. 101-110.
52. Di Cocco, V., F. Iacoviello, and S. Natali, *Fatigue microstructural evolution in pseudo elastic NiTi alloy.* Procedia Structural Integrity, 2016. **2**: p. 1457-1464.
53. Lagoudas, D.C., *Shape Memory Alloys: Modeling and Engineering Applications*. 2008: Springer US.

54. Saigal, A. and M. Fonte, *Solid, shape recovered "bulk" Nitinol: Part I—Tension–compression asymmetry.* Materials Science and Engineering: A, 2011. **528**(16): p. 5536-5550.
55. Saigal, A. and M. Fonte, *Solid, shape recovered "Bulk" nitinol: Part II—Mechanical properties.* Materials Science and Engineering: A, 2011. **528**(16): p. 5551-5559.
56. Zurbitu, J., Kustov, S, Zabaleta, A, Cesari, E and Aurrekoetxea, J *Thermo-Mechanical Behaviour of NiTi at Impact*, in *Shape Memory Alloys*, C. Cismasiu, Editor. 2010, InTech.
57. Van Humbeeck, J., M. Chandrasekaran, and L. Delaey, *Shape memory alloys: materials in action.* Endeavour, 1991. **15**: p. 148-154.
58. Hassan, M.R., M. Mehrpouya, and S. Dawood, *Review of the Machining Difficulties of Nickel-Titanium Based Shape Memory Alloys*, in *Advances in Mechanical and Manufacturing Engineering*, Z.A. Zulkefli, et al., Editors. 2014, Trans Tech Publications Ltd: Stafa-Zurich. p. 533-537.
59. Auricchio, F. and E. Sacco, *A one-dimensional model for superelastic shape-memory alloys with different elastic properties between austenite and martensite.* International Journal of Non-Linear Mechanics, 1997. **32**(6): p. 1101-1114.
60. Auricchio, F., R.L. Taylor, and J. Lubliner, *Shape-memory alloys: macromodelling and numerical simulations of the superelastic behavior.* Computer Methods in Applied Mechanics and Engineering, 1997. **146**: p. 281-312.
61. Paiva, A., et al., *A constitutive model for shape memory alloys considering tensile-compressive asymmetry and plasticity.* Int. J. Solids and Structures, 2005. **42**: p. 3439-3457.
62. Brinson, L.C., *One-Dimensional Constitutive Behavior of Shape Memory Alloys: Thermomechanical Derivation with Non-Constant Material Functions and Redefined Martensite Internal Variable.* Journal of Intelligent Material Systems and Structures, 1993. **4**(2): p. 229-242.
63. Auricchio, F., *A robust integration-algorithm for a finite-strain shape-memory-alloy superelastic model.* International Journal of Plasticity, 2001. **17**(7): p. 971-990.
64. Boyd, J.G. and D.C. Lagoudas, *A thermodynamical constitutive model for shape memory materials. Part II. The SMA composite material.* International Journal of Plasticity, 1996. **12**: p. 843-873.
65. Boyd, J.G. and D.C. Lagoudas, *A thermodynamical constitutive model for shape memory materials. Part I. The monolithic shape memory alloy.* International Journal of Plasticity, 1996. **12**: p. 805-842.
66. ABAQUS, *ABAQUS User Manuals, Version 6.9*, 2009.
67. Gong, X.Y., et al., *Finite element analysis and experimental evaluation of superelastic Nitinol stent*. SMST-2003: Proceedings of the International Conference on Shape Memory and Superelastic Technologies, ed. A.R. Pelton and T. Duerig. 2004. 453-462.
68. Gong, X.-Y. and A.R. Pelton. *ABAQUS analysis on nitinol medical applications*. in *ABAQUS*. 2002.
69. Auricchio, F., E. Boatti, and M. Conti, *Chapter 12 - SMA Cardiovascular Applications and Computer-Based Design*, in *Shape Memory Alloy Engineering*, L.L. Concilio, Editor. 2015, Butterworth-Heinemann: Boston. p. 343-367.
70. Auricchio, F. and E. Sacco, *A Superelastic Shape-Memory-Alloy Beam Model.* Journal of Intelligent Material Systems and Structures, 1997. **8**(6): p. 489-501.

71. Lagoudas, D.C., Z. Bo, and M.A. Qidwai, *A unified thermodynamic constitutive model for SMA and finite element analysis of active metal matrix composites.* Mechanics of Composite Materials and Structures, 1996. **3**: p. 153-179.
72. Tanaka, K., *A Thermomechanical Sketch of Shape Memory Effect - One-dimensional Tensile Behavior.* Res Mechanica, 1986. **18**(3): p. 251-263.
73. Liang, C. and C.A. Rogers, *A multi-dimensional constitutive model for shape memory alloys.* Journal of Engineering Mathematics, 1992. **26**(3): p. 429-443.
74. Qidwai, M.A. and D.C. Lagoudas, *Numerical implementation of a shape memory alloy thermomechanical constitutive model using return mapping algorithms.* International Journal for Numerical Methods in Engineering, 2000. **47**: p. 1123-1168.
75. Frost, M., B. Benešová, and P. Sedlák, *A microscopically motivated constitutive model for shape memory alloys: Formulation, analysis and computations.* Mathematics and Mechanics of Solids, 2016. **21**(3): p. 358-382.
76. Frost, M., et al., *Modeling of mechanical response of NiTi shape memory alloy subjected to combined thermal and non-proportional mechanical loading: a case study on helical spring actuator.* Journal of Intelligent Material Systems and Structures, 2016. **27**(14): p. 1927-1938.
77. Sedlák, P. and M. Frost, *Two-Dimensional Thermomechanical Model for Combined Loading of NiTi Wire Structures.* 2009(48968): p. 101-109.
78. Thomasová, M., et al., *Evolution of macroscopic elastic moduli of martensitic polycrystalline NiTi and NiTiCu shape memory alloys with pseudoplastic straining.* Acta Materialia, 2017. **123**: p. 146-156.
79. Brocca, M., L.C. Brinson, and Z.P. Bažant, *Three-dimensional constitutive model for shape memory alloys based on microplane model.* Journal of the Mechanics and Physics of Solids, 2002. **50**(5): p. 1051-1077.
80. Lagoudas, D.C. and P.B. Entchev, *Modeling of transformation-induced plasticity and its effect on the behavior of porous shape memory alloys. Part I: constitutive model for fully dense SMAs.* Mechanics of Materials, 2004. **36**(9): p. 865-892.
81. Oliver, W.C. and G.M. Pharr, *An Improved Technique for Determining Hardness and Elastic Modulus Using Load and Displacement Sensing Indentation Experiments.* Journal of Materials Research, 1992. **7**(6): p. 1564-1583.
82. Oliver, W.C. and G.M. Pharr, *Measurement of hardness and elastic modulus by instrumented indentation: Advances in understanding and refinements to methodology.* Journal of Materials Research, 2004. **19**: p. 3-20.
83. Gong, J., et al., *Micro- and Nanopatterning of Inorganic and Polymeric Substrates by Indentation Lithography.* Nano Letters, 2010. **10**(7): p. 2702-2708.
84. Van Vliet, K.J., L. Prchlik, and J.F. Smith, *Direct measurement of indentation frame compliance.* Journal of Materials Research, 2011. **19**(1): p. 325-331.
85. Ullner, C., et al., *Effect and measurement of the machine compliance in the macro range of instrumented indentation test.* Measurement, 2010. **43**(2): p. 216-222.
86. Harsono, E., S. Swaddiwudhipong, and Z.S. Liu, *The effect of friction on indentation test results.* Modelling and Simulation in Materials Science and Engineering, 2008. **16**(6): p. 065001.
87. Mata, M. and J. Alcala, *The Role of Friction on Sharp Indentation.* Journal of the Mechanics and Physics of Solids, 2004. **52**: p. 145-165.
88. Menčík, J., *Uncertainties and Errors in Nanoindentation*, in *Nanoindentation in Materials Science*, J. Nemecek, Editor. 2012, InTech: Rijeka. p. Ch. 03.

89. Feng, G. and A.H.W. Ngan, *Effects of creep and thermal drift on modulus measurement using depth-sensing indentation.* Journal of Materials Research, 2002. **17**(3): p. 660-668.
90. Kim, J.-Y., et al., *Influence of surface-roughness on indentation size effect.* Acta Materialia, 2007. **55**(10): p. 3555-3562.
91. Atkinson, M., *Further Analysis of the Size Effect in Indentation Hardness Tests of Some Metals.* Journal of Materials Research, 1995. **10**(11): p. 2908-2915.
92. Bull, S.J., T.F. Page, and E.H. Yoffe, *An Explanation of the Indentation Size Effect in Ceramics.* Philosophical Magazine Letters, 1989. **59**(6): p. 281-288.
93. Kim, J.-Y., et al., *Influence of tip bluntness on the size-dependent nanoindentation hardness.* Scripta Materialia, 2005. **52**: p. 353-358.
94. Liu, Y., et al., *Orientation Effects in Nanoindentation of Single Crystal Copper.* International Journal of Plasticity, 2008. **24**: p. 1990-2015.
95. Stelmashenko, N.A., et al., *Microindentations on W and Mo oriented single crystals: An STM study.* Acta Metallurgica et Materialia, 1993. **41**(10): p. 2855-2865.
96. Casals, O., J. Ocenasek, and J. Alcala, *Crystal Plasticity Finite Element Simulations of Pyramidal Indentation in Copper Single Crystals.* Acta Mater., 2007. **55**: p. 55-68.
97. Zhao, M.H., et al., *Determination of uniaxial residual stress and mechanical properties by instrumented indentation.* Acta Materialia, 2006. **54**(10): p. 2823-2832.
98. Bressan, J.D., A. Tramontin, and C. Rosa, *Modeling of Nanoindentation of Bulk and Thin Film by Finite Element Method.* Wear, 2005. **258**: p. 115-122.
99. Alaboodi, A.S. and Z. Hussain, *Finite element modeling of nano-indentation technique to characterize thin film coatings.* Journal of King Saud University - Engineering Sciences, 2017.
100. Gan, L. and B. BenNissan, *The effects of mechanical properties of thin films on nano-indentation data: Finite element analysis.* Computational Materials Science, 1997. **8**(3): p. 273-281.
101. Saha, R. and W.D. Nix, *Effects of the substrate on the determination of thin film mechanical properties by nanoindentation.* Acta Materialia, 2002. **50**(1): p. 23-38.
102. Michler, J. and E. Blank, *Analysis of coating fracture and substrate plasticity induced by spherical indentors: diamond and diamond-like carbon layers on steel substrates.* Thin Solid Films, 2001. **381**(1): p. 119-134.
103. He, J.L. and S. Veprek, *Finite element modeling of indentation into superhard coatings.* Surface & Coatings Technology, 2003. **163**: p. 374-379.
104. Park, Y.J. and G.M. Pharr, *Nanoindentation with spherical indenters: finite element studies of deformation in the elastic-plastic transition regime.* Thin Solid Films Proceedings of the 30th International Conference on Metallurgical Coatings and Thin Films, 2004. **447-448**: p. 246-250.
105. Zhao, X., Z. Xie, and P. Munroe, *Nanoindentation of hard multilayer coatings: Finite element modelling.* Materials Science and Engineering: A, 2011. **528**(3): p. 1111-1116.
106. Fivel, M., M. Verdier, and G. Canova, *3D Simulation of a Nanoindentation Test at a Mesoscopic Scale.* Mat. Sci. & Eng. A, 1997. **234**: p. 923-926.
107. Bouzakis, K., et al., *Continuous FEM Simulation of the Nanoindentation.* Zeit. Metallk., 2002. **93**: p. 862-869.
108. Elmustafa, A. and D. Stone, *Strain Rate Sensitivity in Nanoindentation Creep of Hard Materials.* J. Mater. Res., 2007. **22**: p. 2912-2916.

109. Bouvier, S. and A. Needleman, *Effect of the Number and Orientation of Active Slip Systems on Plane Strain Single Crystal Indentation.* Modelling Simul. Mat. Sci. Eng., 2006. **14**: p. 1105-1125.
110. Chen, F. and R. Chang, *Study of the Effect of Imperfect Tips on Nanoindentation by FEM.* J. Mech. Sci. Techn., 2007. **21**: p. 1471-1476.
111. Bouzakis, K. and N. Michailidis, *Coating Elastic-plastic Properties determined by means of Nanoindentations and FEM-supported Evaluation Algorithms.* Thin Solid Films, 2004. **469**: p. 227-232.
112. Bouzakis, K. and N. Michailidis, *An Accurate and Fast Approach for Determining Materials Stress-strain Curves by Nanoindentation and its FEM-based Simulation.* Materials Characterisation, 2006. **56**: p. 147-157.
113. Bouzakis, K.D., G. Skordaris, and E. Bouzakis, *Methods for Determining Coating's Strength Properties Changes After Inducing Plastic or Elastic Residual Stresses.* Procedia Engineering, 2011. **19**: p. 34-39.
114. Chen, X., et al., *A combined inverse finite element – elastoplastic modelling method to simulate the size-effect in nanoindentation and characterise materials from the nano to micro-scale.* International Journal of Solids and Structures, 2017. **104**: p. 25-34.
115. Gomez, J. and C. Basaran, *Nanoindentation of Pb/Sn solder alloys; experimental and finite element simulation results.* International Journal of Solids and Structures, 2006. **43**(6): p. 1505-1527.
116. Liu, M., et al., *A combined experimental-numerical approach for determining mechanical properties of aluminum subjects to nanoindentation.* Scientific Reports, 2015. **5**: p. 15072.
117. Guha, S., S. Sangal, and S. Basu, *Finite Element studies on indentation size effect using a higher order strain gradient theory.* International Journal of Solids and Structures, 2013. **50**(6): p. 863-875.
118. Salehi, S.H. and M. Salehi, *Numerical investigation of nanoindentation size effect using micropolar theory.* Acta Mechanica, 2014. **225**(12): p. 3365-3376.
119. Dao, M., et al., *Computational modeling of the forward and reverse problems in instrumented sharp indentation.* Acta Materialia, 2001. **49**: p. 3899-3918.
120. Gao, F.C. and L.X. Han, *Implementing the Nelder-Mead simplex algorithm with adaptive parameters.* Computational Optimization and Applications, 2012. **51**(1): p. 259-277.
121. Nelder, J.A. and R. Mead, *A Simplex Method for Function Minimization.* The Computer Journal, 1965. **7**(4): p. 308-313.
122. Kan, Q., et al., *Oliver–Pharr indentation method in determining elastic moduli of shape memory alloys—A phase transformable material.* Journal of the Mechanics and Physics of Solids, 2013. **61**(10): p. 2015-2033.
123. Nolan, J.M., et al. *3D finite element analysis of indentation recovery due to the shape memory effect*. 2010.
124. Yu, A.P., et al., *Thermo-mechanical finite element modeling of shape memory materials' microindentation.* IOP Conference Series: Materials Science and Engineering, 2016. **130**(1): p. 012054.
125. Yan, W.Y., et al., *Determination of transformation stresses of shape memory alloy thin films: A method based on spherical indentation.* Applied Physics Letters, 2006. **88**(24).
126. *Standard Test Method for Transformation Temperature of Nickel-Titanium Alloys by Thermal Analysis*, 2016, ASTM International.

127. Yoon, S.H. and D.J. Yeo, *Phase transformations of nitinol shape memory alloy by varying with annealing heat treatment conditions*, in *Smart Materials III*, A.R. Wilson, Editor. 2005, Spie-Int Soc Optical Engineering: Bellingham. p. 208-215.
128. Kato, H. and K. Sasaki, *Avoiding error of determining the martensite finish temperature due to thermal inertia in differential scanning calorimetry: model and experiment of Ni–Ti and Cu–Al–Ni shape memory alloys.* Journal of Materials Science, 2012. **47**(3): p. 1399-1410.
129. Bragg, W.H. and W.L. Bragg, *The Reflection of X-rays by Crystals.* Proceedings of the Royal Society of London. Series A, 1913. **88**(605): p. 428-438.
130. Dwight, A.E., Trans. Met. Soc. AIME, 1959. **215**: p. 283-285.
131. Mlocek, B., et al., *Phase Analysis of NiTi Shape Memory Wires and Computer Simulations of the Superelastic Effect.* Acta Physica Polonica A, 2016. **130**(4): p. 1063-1065.
132. Polatidis, E., N. Zotov, and E.J. Mittemeijer, *Stress-induced phase transformations in thermally cycled superelastic NiTi alloys: in situ X-ray diffraction studies.* Powder Diffraction, 2015. **30**(S1): p. S76-S82.
133. *Standard Test Method for Dynamic Young's Modulus, Shear Modulus, and Poisson's Ratio by Impulse Excitation of Vibration*.
134. Burley, M., et al., *Johnson-Cook parameter evaluation from ballistic impact data via iterative FEM modelling.* International Journal of Impact Engineering, 2018. **112**: p. 180-192.
135. Lagarias, J.C., et al., *Convergence properties of the Nelder-Mead simplex method in low dimensions.* Siam Journal on Optimization, 1998. **9**(1): p. 112-147.
136. Kear, M., et al., *Computational aerodynamic optimisation of vertical axis wind turbine blades.* Applied Mathematical Modelling, 2016. **40**(2): p. 1038-1051.
137. Liu, Y. *Detwinning process and its anisotropy in shape memory alloys*. in *Smart Materials and MEMS*. 2001. SPIE.
138. Rao, A., A. Ruimi, and A.R. Srinivasa, *Internal loops in superelastic shape memory alloy wires under torsion – Experiments and simulations/predictions.* International Journal of Solids and Structures, 2014. **51**(25): p. 4554-4571.
139. Bo, Z. and D.C. Lagoudas, *Thermomechanical modeling of polycrystalline SMAs under cyclic loading, Part IV: modeling of minor hysteresis loops.* International Journal of Engineering Science, 1999. **37**(9): p. 1205-1249.
140. Cisse, C., W. Zaki, and T. Ben Zineb, *A review of constitutive models and modeling techniques for shape memory alloys.* International Journal of Plasticity, 2016. **76**: p. 244-284.
141. Machado, L.G. and D.C. Lagoudas, *Thermomechanical Constitutive Modeling of SMAs*, in *Shape Memory Alloys: Modeling and Engineering Applications*. 2008, Springer US: Boston, MA. p. 121-187.
142. Pharr, G.M., W.C. Oliver, and F.R. Brotzen, *On the Generality of the Relationship Among Contact Stiffness, Contact Area, and Elastic Modulus During Indentation.* J. Mater. Res., 1992. **7**(3): p. 613-617.
143. Fischer-Cripps, A.C., *Study of analysis methods of depth-sensing indentation test data for spherical indenters.* Journal of Materials Research, 2001. **16**(6): p. 1579-84.
144. Fischer-Cripps, A.C., *Simulation of sub-micron indentation tests with spherical and Berkovich indenters.* Journal of Materials Research, 2001. **16**(7): p. 2149-2157.
145. Fischer-Cripps, A.C., *A review of analysis methods for sub-micron indentation testing.* Vacuum, 2000. **58**: p. 569-585.

146. Fischer-Cripps, A.C., *Nanoindentation*. Mechanical Engineering Series, ed. F.F. Ling. 2004, New York: Springer-Verlag.
147. Fischer-Cripps, A.C., et al., *Methods of correction for analysis of depth-sensing indentation test data for spherical indenters.* Journal of Materials Research, 2001. **16**(8): p. 2244-2250.